

March 2021

## Optimization of Cathode/Anode Electrode Materials for High Performance Lithium-ion Batteries

MINGWEI SHANG

*University of Wisconsin-Milwaukee*

Follow this and additional works at: <https://dc.uwm.edu/etd>



Part of the [Engineering Commons](#)

---

### Recommended Citation

SHANG, MINGWEI, "Optimization of Cathode/Anode Electrode Materials for High Performance Lithium-ion Batteries" (2021). *Theses and Dissertations*. 2731.

<https://dc.uwm.edu/etd/2731>

This Dissertation is brought to you for free and open access by UWM Digital Commons. It has been accepted for inclusion in Theses and Dissertations by an authorized administrator of UWM Digital Commons. For more information, please contact [scholarlycommunicationteam-group@uwm.edu](mailto:scholarlycommunicationteam-group@uwm.edu).

OPTIMIZATION OF CATHODE/ANODE ELECTRODE  
MATERIALS FOR HIGH PERFORMANCE LITHIUM-ION  
BATTERIES

by  
Mingwei Shang

A Dissertation Submitted in  
Partial Fulfillment of the  
Requirement for the Degree of

Doctor of Philosophy  
in Engineering

at  
The University of Wisconsin-Milwaukee  
May 2021

# ABSTRACT

## OPTIMIZATION OF CATHODE/ANODE ELECTRODE MATERIALS FOR HIGH PERFORMANCE LITHIUM-ION BATTERIES

by

Mingwei Shang

The University of Wisconsin-Milwaukee, 2021  
Under the Supervision of Professor Junjie Niu

Lithium-ion batteries (LIBs) have been widely used in various devices such as portable devices, communication systems, and electric vehicles (EVs). In this dissertation, towards building LIBs with enhanced energy density and improved performance, Ni-rich cathode and Si-based anode are selected as the electrodes. The performance of LIBs is improved through optimization on both cathode and anode material.

Ni-rich layered transition metal oxide with dual gradient on both primary and secondary particles was successfully designed and synthesized through introducing Ni-based metal-organic framework (Ni-MOF) to the coprecipitation of the precursor. During the calcination process, the presence of organic components of Ni-MOFs promotes the formation of reduced Ni oxidation state, leading to the formation of self-induced cation mixing layer with stable rock salt phase on the surface of primary particles. It can successfully increase the structural stability through inhibiting the generation of internal cracks caused by the internal strain and phase transition within primary particles during cycling process. The metallic components from Ni-MOFs in the core lead to the formation of Ni concentration gradient within secondary particles. As results, a

greatly improved electro-chemo-mechanical stability was achieved, which contributed to the enhanced battery capacity retention upon long cycling.

At the same time, to overcome the disadvantages of Si-based anode material, including huge volume change, poor cycling stability, and low conductivity, micro-sized AlSi alloy was used to form the Si skeleton with an ultra-thin (<5 nm) mesoporous polypyrrole (PPy) skin ( $\mu$ -Si cage) through a facile wet-chemical method. Under this configuration, the hollow skeleton provides sufficient space to accommodate the large volume change upon lithiation/delithiation process. The conductive PPy layer serves as a protective layer and fast channel for  $\text{Li}^+/\text{e}^-$  transport. In addition, the application of micro-sized Si ensures high active mass loading and areal capacity. The battery with the obtained  $\mu$ -Si cage as anode displayed excellent capacity retention upon long cycling at high charge/discharge rates and high active mass loadings.

Additionally, the development of other Si-based materials was also explored in this dissertation. SiGe@MXene composite was obtained through a low-temperature reduction from the corresponding oxide. Through alloying with Ge, SiGe alloy showed improved rate performance and cycling stability compared with pure Si anode. Herein, the combination of SiGe alloy and MXene can further increase the performance of SiGe-based anode material. The autoadjustable layer space of MXene can provide sufficient space to accommodate the volume expansion/shrinkage upon  $\text{Li}^+$  insertion/extraction process. At the same time, it can provide superior conductivity, which can promote fast transportation of  $\text{Li}^+/\text{e}^-$ . With the incorporation of MXene, the SiGe@MXene composite exhibited improved cycling stability and rate capability, which shows great potential as anode material for high-performance LIBs.

© Copyright by Mingwei Shang, 2021  
All Rights Reserved

To  
my parents,  
my wife,  
and especially my daughters

# TABLE OF CONTENTS

<b>LIST OF FIGURES .....</b>	<b>ix</b>
<b>LIST OF TABLES .....</b>	<b>xvii</b>
<b>LIST OF ABBREVIATIONS .....</b>	<b>xviii</b>
<b>ACKNOWLEDGEMENTS .....</b>	<b>xxii</b>
<b>CHAPTER 1 INTRODUCTION .....</b>	<b>1</b>
1.1 Development of Lithium-ion batteries.....	1
1.1.1 Cathode .....	2
1.1.2 Anode.....	3
1.1.3 Components and working principle of modern LIBs. ....	4
1.2 Development of Cathode .....	7
1.2.1 Current state of art in Ni-rich cathode material .....	7
1.2.3 Rationale of Ni-rich cathode material modification .....	16
1.3 Development of Anode materials .....	18
1.3.1 Silicon anode.....	18
1.3.2 Si nanostructure. ....	20
1.3.3 Micrometer-sized Si.....	22
1.3.4 Development of advanced binder .....	26
1.4 Design of battery with improved performance by engineering electrode materials.....	29
Optimization of cathode:.....	29
Development of anode: .....	29
<b>CHAPTER 2 Ni-Rich Layered Transition Metal Oxide Cathode with Dual Gradient on Both Primary and Secondary Particles for High Energy-Density Lithium-Ion Batteries... 31</b>	
2.1 Introduction.....	31
2.2 Design strategies and preparation of D-NMC811 .....	34
2.2.1 Synthesis of D-NMC811.....	34
2.2.2 Working mechanism of Ni-MOFs .....	35
2.3 Characterization of D-NMC811 .....	38

2.3.1 Characterization of Ni-MOFs .....	38
2.3.2 Morphology and crystal structure .....	41
2.3.2 Confirmation of the gradient on both primary and secondary particles. ....	46
2.3.3 Confirmation of the oxidation state change .....	49
2.3.4 X-ray photoelectron spectroscopy characterization .....	51
2.4 Electrochemical performance .....	53
2.4.1 CV .....	53
2.4.2 Battery performance.....	54
2.4.3 EIS characterization .....	57
2.4.4 dQ/dV characterization .....	58
2.4.5 DSC measurement .....	59
2.5 Full cell performance .....	61
2.6 Characterization after cycling .....	65
2.6.1 Morphology and structure.....	65
2.6.2 XPS characterization.....	68
2.6.3 <i>Ex situ</i> XRD .....	70
2.7 Conclusion .....	72
2.8 Experimental .....	73
2.4.1 Synthesis of Ni-MOF.....	73
2.4.2 Synthesis of NMC811 and D-NMC811.....	73
2.4.3 Electrochemical measurement .....	74
2.4.4 Sample characterization.....	76
<b>CHAPTER 3 Development of Si-Based Anode for Li-Ion Battery with Largely Improved</b>	
<b>Performance .....</b>	<b>78</b>
3.1 Introduction.....	78
3.2 Design strategies and preparation of $\mu$ -Si cage .....	81
3.3 Characterization .....	83
3.3.1 Morphology of the $\mu$ -Si cage .....	83
3.3.2 XRD characterization.....	86
3.3.3 TGA .....	87
3.3.4 BET analysis .....	88
3.3.5 Etching process analysis .....	89
3.3 Electrochemical performance .....	93

3.4 Characterization after cycling .....	98
3.5 Conclusions.....	101
3.6 Methods/Experimental.....	102
3.6.1 Material synthesis .....	102
3.6.2 Electrochemical measurements.....	103
3.6.3 Sample characterizations .....	104
<b>CHAPTER 4 Other Si-based Anode Materials.....</b>	<b>106</b>
4.1 Introduction.....	106
4.2 Design strategies and preparation .....	109
4.3 Characterization .....	110
4.3.1 Morphology characterization.....	110
4.3.2 XRD characterization.....	111
4.4 Electrochemical performance .....	112
4.5 Conclusion .....	114
4.4 Experimental details.....	115
<b>CHAPTER 5 Summary and outlooks .....</b>	<b>117</b>
<b>REFERENCES.....</b>	<b>120</b>
<b>CURRICULUM VITAE.....</b>	<b>144</b>

# LIST OF FIGURES

<b>Figure 1.1</b> Schematic illustration of the LMO <sub>2</sub> with layered structure (Copyright 2007 Elsevier). <sup>4</sup> .....	2
<b>Figure 1.2</b> Schematics of a typical Li-ion cell. (Copyright 2012, Wiley-VCH GmbH, Weinheim) <sup>2</sup> .....	4
<b>Figure 1.3</b> Li-ion battery cell configurations (Copyright 2018, Elsevier). <sup>1</sup> .....	6
<b>Figure 1.4</b> Radar plots comparing various classes of high-voltage positive electrode materials with one example composition in terms of energy density (volumetric), power, cyclability (with commercial carbon-based negative electrodes), cost and thermal stability. The electrochemical performance of LiVPO <sub>4</sub> F is based on solely the V <sup>3+/4+</sup> redox couple. Dashed lines exhibit the cyclability of the two samples (Li <sub>1.2</sub> Ni <sub>0.2</sub> Mn <sub>0.6</sub> O <sub>2</sub> and LiNi <sub>0.5</sub> Mn <sub>1.5</sub> O <sub>4</sub> ) obtained in Li-metal half cells (Copyright 2017, The Royal Society of Chemistry). <sup>10</sup> .....	8
<b>Figure 1.5</b> The partial O replacement doped by S in the lattice of Li <sub>1.2</sub> Ni <sub>0.13</sub> Co <sub>0.13</sub> Mn <sub>0.54</sub> O <sub>2</sub> (Copyright 2019, Elsevier) <sup>47</sup> .....	9
<b>Figure 1.6</b> Schematic illustration of the stability improvement through coating on both secondary/primary particle via oCVD (Copyright 2019, Nature Publishing Group). <sup>64</sup> .....	11
<b>Figure 1.7</b> Schematic illustration of the Ni-rich LiNi <sub>0.8</sub> Co <sub>0.1</sub> Mn <sub>0.1</sub> O <sub>2</sub> with Ni concentration gradient (Copyright 2017, American Chemistry Society). <sup>65</sup> .....	12
<b>Figure 1.8</b> a) Schematic of the synthesis process of porous LiNi <sub>0.6</sub> Co <sub>0.2</sub> Mn <sub>0.2</sub> O <sub>2</sub> by coprecipitation method with polystyrene beads (PSBs) and corresponding cross-sectioned SEM images of (b) precursor and (c) lithiated PSB-NMC. d) A HAADF-STEM image showing the high magnified cross-sectioned PSB-NCM (Copyright 2017, Wiley-VCH GmbH, Weinheim). <sup>64</sup> .....	13

<b>Figure 1.9</b> Schematic illustration of the structure and characterization of (a) commercial NMC and (b) Ni-rich $\text{LiNi}_{0.8}\text{Co}_{0.1}\text{Mn}_{0.1}\text{O}_2$ cathode material with radially aligned single-crystal primary particles (Copyright 2019, Wiley-VCH GmbH, Weinheim). <sup>69</sup> .....	15
<b>Figure 1.10</b> Schematic illustration of the lithiation process of a) solid nanowires, with repetitive SEI formation on the surface after cycling, b) Si nanotubes, with a similar outcome that SEI continues to grow upon the shrinking and expansion of the nanotubes, and c) Si nanotubes with a mechanical constraining layer on the surface, where a thin and stable SEI layer is built. Reproduced with permission (Copyright 2012, Nature Publishing Group). <sup>97</sup> .....	20
<b>Figure 1.11</b> Schematic illustration of the Li-ion pathway in Si nanotube (Copyright 2009, American Chemistry Society). <sup>107</sup> .....	21
<b>Figure 1.12</b> SEM images of 3D porous Si-C particles at different magnification (Copyright 2008, Wiley-VCH GmbH, Weinheim). <sup>113</sup> .....	23
<b>Figure 1.13</b> The preparation process from SiO precursor to the Si-C composite (Copyright 2013, Wiley-VCH GmbH, Weinheim). <sup>114</sup> .....	24
<b>Figure 1.14</b> Schematic illustration and packing status with different size distribution of the watermelon-inspired Si/C microspheres (Copyright 2017, Wiley-VCH GmbH, Weinheim). <sup>115</sup> .	25
<b>Figure 1.15</b> Schematics of the technical approaches to address volume change issue in battery materials. (Copyright 2011, Wiley-VCH GmbH, Weinheim). <sup>116</sup> .....	27
<b>Figure 2.1</b> Design of MOF modulated double-Ni-gradient NMC811. Synthesis process of the D-NMC811. ....	34
<b>Figure 2.2</b> Schematic illustration of how cationic disordering is suppressed through surface reconstruction by the presence of Ni-MOF in D-NMC811 during calcination. ....	36
<b>Figure 2.3</b> SEM morphologies of the Ni-MOF precursor under different magnification.....	38

<b>Figure 2.4</b> Surface and TGA analysis of the Ni-MOF. Nitrogen sorption-desorption isotherms (a) and the pore size distribution (b). (c) TGA data at a rate of 5 °C/min under an air flow of 50 ml/min. (d) XRD patterns of Ni-MOF before and after TGA. ....	39
<b>Figure 2.5</b> XRD pattern of the NMC811 obtained directly from the NiCoMn-MOF. ....	40
<b>Figure 2.6</b> Cycling performance of the NMC811 obtained directly from the NiCoMn-MOF. ....	41
<b>Figure 2.7</b> SEM morphologies of (a-b) the D-NMC811, and (c-d) the conventional NMC811. ....	42
<b>Figure 2.8</b> Surface analysis of the D-NMC811 and conventional NMC811. Nitrogen sorption-desorption isotherms and pore size distribution of the conventional NMC811 (a, b) and the D-NMC811 (c, d). ....	43
<b>Figure 2.9</b> XRD patterns and refinement results of the D-NMC811 and the conventional NMC811. ....	44
<b>Figure 2.10</b> Phase structure and chemical composition diagnosis of primary and secondary particles. High-resolution TEM along with the corresponding FFT analysis of the primary particle with (a) conventional NMC811 and (b) D-NMC811, respectively. The A region corresponds to the surface area while B is located at the core area. ....	46
<b>Figure 2.11</b> Cross-section view (a) and the corresponding Ni, Mn, Co concentration evolution from the surface to core (b) of a secondary particle of D-NMC811. TEM morphology (c) and concentration evolution from the surface to core (d) of a primary particle of D-NMC811. ....	47
<b>Figure 2.12</b> STEM image (a) of a primary particle of D-NMC811 with corresponding EELS spectra of Mn (b), Co (c), and Ni (d) L-edges. ....	49
<b>Figure 2.13</b> XPS spectra analysis of the D-NMC811 and conventional NMC811. Depth profiles of Ni 2p (a-b), O 1s (c-d), and XPS spectra of C 1s (e-f), respectively. The ratio evolution of Ni to	

Ni<sup>2+</sup>/Ni<sup>3+</sup> (g) and lattice oxygen (TM-O) (h) with increasing etching time obtained from the depth profiles. .... 51

**Figure 2.14** Cyclic voltammetry of D-NMC811 and NMC811 at a scanning rate of 0.1 mV/s.. 53

**Figure 2.15** (a) Charge/discharge voltage profile of the first cycle at 0.1 C (2.8-4.3 V, 1 C=180 mAh/g). (b) Specific charge/discharge capacity evolution of D-NMC811 and NMC811 at different rates from 0.1 C to 5.0 C (before test, the batteries were charged/discharged at 0.1 C between 2.8 to 4.3 V for 4 cycles for activation). Battery cycling performance (c,d) of D-NMC811 and NMC811 at 1/3 C at the temperature of 25 °C and 55 °C, respectively. The loading was controlled to be 5-6 mg/cm<sup>2</sup>. The interrupted data were originated from the temperature perturbation upon operation. .... 54

**Figure 2.16** Cycling performance of half-cell batteries with the D-NMC811 and conventional NMC811 as cathode electrode materials at 1.0 C and 25°C, respectively. Before cycling at 1.0 C, the batteries were charged/discharged three times at 0.1 C for activation. The mass loading of D-NMC811 and NMC811 is 5-6 mg/cm<sup>2</sup>. .... 56

**Figure 2.17** Nyquist plots of the cells with D-NMC811 (red) and conventional NMC811 (black) before and after 100 cycles at 1 C, respectively (the coin cells were charged to 4.3 V and kept for 2 h before test). .... 57

**Figure 2.18** dQ/dV vs potential plots of D-NMC811 (a) and conventional NMC811 (b) at 10th, 50th and 100th cycles..... 58

**Figure 2.19** DSC profiles of D-NMC811 and NMC811 at a scan rate of 10 °C/min in N<sub>2</sub> (The coin cells were charged to 4.3 V and kept for 2 h before disassembling in glovebox. The obtained electrode material and electrolyte with total mass of 10 mg were collected and sealed in aluminum pan in glovebox for test. ). .... 59

**Figure 2.20** (a) Full-cell battery cycling performance with D-NMC811 and NMC811 at 1/3 C. The cathode mass loading of the active material is ~8.2 mg/cm<sup>2</sup>. The N/P ratio is 1.16. The battery was activated at 0.1 C for 4 cycles before cycling. (b) 300 mAh pouch-cell battery cycling performance with D-NMC811 and NMC811 at 1.0 C. .... 62

**Figure 2.21** Specific capacity (a) and the estimated energy density (b) evolution upon cycling of the full-cell pouch cells with D-NMC811 and conventional NMC811 as cathode electrode materials at 1.0 C, respectively. The pouch cell electrode was made with double-side coated cathode materials with a single side mass loading of ~12.2 mg/cm<sup>2</sup> and a N/P ratio of 1.16. .... 63

**Figure 2.22** Active material morphology evolution after 300 cycles at 1.0 C. SEM morphologies of the conventional NMC811 (a,b) and the D-NMC811 (c,d)..... 65

**Figure 2.23** TEM morphologies of the D-NMC811 (a,b) and conventional NMC811 (c, d) after 300 cycles at 1.0 C. .... 66

**Figure 2.24** The corresponding XPS spectra of F1s, O1s, and C1s of D-NMC811 (a, c, e) and the conventional NMC811 (b, d, e). .... 68

**Figure 2.25** *EX situ* XRD patterns for NMC811, D-NMC811 at 4.3 V and 4.5 V, respectively. 70

**Figure 2.26** The lattice parameter of *V* calculated by Rietveld refinement of the XRD patterns for NMC811 and D-NMC811 at original state, 4.3 V, and 4.5 V, respectively..... 71

**Figure 2.27** Formation and activation process of the obtained pouch cells with D-NMC811 and conventional NMC811 as cathode electrode materials, respectively. .... 75

**Figure 3.1** Scalable synthesis of  $\mu$ -Si cage using AlSi micro-spheres as precursor by chemical method..... 81

**Figure 3.2** TEM morphology (inset) of  $\mu$ -Si cage. Line elemental mapping (a) and area elemental mapping (b) of a  $\mu$ -Si cage. High-resolution TEM image of the edge of a  $\mu$ -Si cage (c)..... 83

**Figure 3.3** Morphology and chemical composition of the sample with different etching processes. SEM images of pure AlSi alloy before (a) and after (b) direct acid etching. SEM images of  $\mu$ -Si cage before (c) and after (d) acid etching. .... 84

**Figure 3.4** SEM images and corresponding size distribution of the AlSi alloy (a, b) and  $\mu$ -Si cage (c, d). .... 85

**Figure 3.5** XRD patterns of the  $\mu$ -Si cage (red), AlSi alloy (black) and commercial Si (green). 86

**Figure 3.6** TGA analysis of the  $\mu$ -Si cage (red) and pure PPy (black) under  $N_2$ . .... 87

**Figure 3.7** Nitrogen sorption-desorption isotherm (a) and the pore size distribution curve (b) of  $\mu$ -Si cage. The inset of (a) is the comparison of surface area and pore volume between AlSi alloy and  $\mu$ -Si cage. .... 88

**Figure 3.8** XPS analysis (a) of pure AlSi alloy (black), AlSi alloy after direct etching (red) and  $\mu$ -Si cage (blue). (b) XPS depth profiling of the  $\mu$ -Si cage before etching ..... 89

**Figure 3.9** FTIR curves of pure AlSi alloy (black) and the  $\mu$ -Si cage (red). .... 90

**Figure 3.10** Morphology and chemical composition of  $\mu$ -Si cage before etching. Elemental mapping of the  $\mu$ -Si cage before etching. .... 91

**Figure 3.11** Galvanostatic charge/discharge profile of  $\mu$ -Si cage with a loading of 3 mg/cm<sup>2</sup> at 1.0 C (a) (the first cycle is activation at 0.2 C with a coulombic efficiency of 78.17%). Cyclic voltammetry of the battery with  $\mu$ -Si cage as anode at 2nd cycle with a scan rate of 0.05 mV/s (b). Nyquist plots of  $\mu$ -Si cage (red) and commercial Si (black) at 5th cycle at 0.2 C obtained from EIS measurements (c). .... 93

**Figure 3.12** Cycling performance of the battery with  $\mu$ -Si cage as anode with loadings of 3 mg/cm<sup>2</sup> (a) and 4.4 mg/cm<sup>2</sup> (b) at various rates of 0.2, 0.5 and 1.0 C, respectively. The specific capacity was calculated based on the pure silicon inside  $\mu$ -Si cage. The black curve in (a) is the battery

performance with commercial silicon as anode. The Coulombic efficiency was calculated at 0.2 C. .....	94
<b>Figure 3.13</b> Areal capacity vs cycle number of the battery with the active material loading of 3 mg/cm <sup>2</sup> (a) and 4.4 mg/cm <sup>2</sup> (b), respectively. ....	95
<b>Figure 3.14</b> Cycling performance of $\mu$ -Si cage in a NMC 622/ $\mu$ -Si cage full cell at 0.2 C (the loading of $\mu$ -Si cage and NMC 622 are 0.6 mg/cm <sup>2</sup> and 11 mg/cm <sup>2</sup> , respectively). ....	96
<b>Figure 3.15</b> Cycling performance of the battery with the $\mu$ -Si cage as anode with a loading of 3 mg/cm <sup>2</sup> at 2.0 C. The specific capacity was calculated based on the pure silicon inside $\mu$ -Si cage. .....	96
<b>Figure 3.16</b> Low-mag (a) and high-mag (b) TEM images of the $\mu$ -Si cage. ....	98
<b>Figure 3.17</b> Elemental mapping of the $\mu$ -Si cage after 20 cycle at 0.5 C. Cycling performance of the battery using $\mu$ -Si cage as anode with different loadings. ....	99
<b>Figure 3.18</b> Cross-section SEM image of $\mu$ -Si cage coating (the loading is 4.7 mg/cm <sup>2</sup> with an as-received density of 950.2 mg/cm <sup>3</sup> ). ....	99
<b>Figure 3.19</b> (a) Volume comparison with 0.3g sample. (b) Produced pellet under the pressure of 155 Mpa displays a density of 1.32 g/cm <sup>3</sup> . ....	100
<b>Figure 4.1</b> Schematic illustration of the GeO <sub>x</sub> @MXene. ....	106
<b>Figure 4.2</b> Cycling performance of the battery with GeO <sub>x</sub> @MXene as anode under (a) 0.5 C and a loading of GeO <sub>x</sub> of 1.0 mg/cm <sup>2</sup> , (b) 0.5 C and GeO <sub>x</sub> loadings of 2.0, 3.4 mg/cm <sup>2</sup> , and (c) 1.0 C, 5.0 C, 10.0 C and 20.0 C (1.0 mg/cm <sup>2</sup> ), respectively. ....	107
<b>Figure 4.3</b> Schematic illustration of the synthesis process of SiGe@MXene. ....	109
<b>Figure 4.4</b> SEM image of SiGe@MXene with corresponding EDS element mapping of Ge, Si, and Ti. ....	110

**Figure 4.5** XRD patterns of the SiGe@MXene and Si@MXene. .... 111

**Figure 4.6** Specific discharge capacity evolution of Si@MXene and SiGe@MXene at different rates from 0.1 to 2.0 C. The batteries were cycled three times at 0.05 C for activation. .... 112

**Figure 4.7** Cycling performance of Si@MXene and SiGe@MXene at 0.5 C. .... 113

## LIST OF TABLES

<b>Table 2-1</b> Lattice parameters, ratio of $I(003)/I(104)$ and $\text{Li}^+/\text{Ni}^{2+}$ mixing derived from the Rietveld refinement of the D-NMC811 and conventional NMC811 .....	45
<b>Table 2-2</b> Calculated change in enthalpy for charged NMC811 and D-NMC811 cathode materials obtained from DSC curves as shown in Figure 2.19. ....	60
<b>Table 2-3</b> Pouch cell detailed parameters .....	64
<b>Table 2-4</b> Lattice parameters from the Rietveld refinement of the D-NMC811 and conventional NMC811. ....	71
<b>Table 3-1</b> Tapped density comparison of $\mu\text{-Si}$ and Si nanoparticles. ....	100

## LIST OF ABBREVIATIONS

BET	Brunauer-Emmett-Teller
CTAB	Cetyl-trimethylammonium bromide
CV	Cyclic voltammetry
oCVD	Oxidative chemical vapor deposition
DEC	Diethyl carbonate
DI	Deionized
DME	Dimethoxy ethane
DMF	Dimethylformamide
DSC	Differential scanning calorimetry
EC	Ethylene carbonate
EDS	Energy dispersive X-ray spectroscopy
EELS	Electron energy-loss spectroscopy
EIS	Electrochemical impedance spectroscopy
EMC	Ethyl methyl carbonate
EV	Electric vehicles
FEC	Fluorinated ethylene propylene

FESEM	Field emission scanning electron microscopy
FFT	Fast Fourier transform
FTIR	Fourier-transform infrared spectroscopy
HAADF-STEM	High-angle annular dark-field scanning transmission electron microscopy
HEV	Hybrid electric vehicles
HF	Hydrofluoric acid
HRTEM	High resolution transmission electron microscopy
ICP-MS	Inductively coupled plasma mass spectrometer
LCO	Lithium cobalt oxide
LFP	Lithium iron phosphate
LIB	Lithium-ion battery
LMO	Lithium manganese oxide
LTO	Lithium titanate
MCMB	Mesocarbon microbeads
MOF	Metal-organic framework
NMP	N-methyl-2-pyrrolidone
NCA	Lithium nickel cobalt aluminum oxide

NMC	Lithium nickel manganese cobalt oxide
NMC111	$\text{LiNi}_{1/3}\text{Mn}_{1/3}\text{Co}_{1/3}\text{O}_2$
NMC532	$\text{LiNi}_{0.5}\text{Mn}_{0.3}\text{Co}_{0.2}\text{O}_2$
NMC622	$\text{LiNi}_{0.6}\text{Mn}_{0.2}\text{Co}_{0.2}\text{O}_2$
NMC811	$\text{LiNi}_{0.8}\text{Mn}_{0.1}\text{Co}_{0.1}\text{O}_2$
PEDOT	Poly(3,4-ethylenedioxythiophene)
Ppy	Polypyrrole
PSB	Polystyrene beads
PVDF	Polyvinyl difluoride
PVP	Polyvinylpyrrolidone
RGO	Reduced graphene oxide
SBR	Styrene-butadiene rubber
SEI	Solid electrolyte interface
SEM	Scanning electron microscopy
STEM	Scanning transmission electron microscopy
TEM	Transmission electron microscopy
TEOS	Tetraethoxysilane

TGA	Thermogravimetric analysis
TM	Transition metal
UHV	Ultrahigh vacuum
VC	Vinylene carbonate
WO <sub>2</sub>	Vinylene carbonate
XPS	X-ray photoelectron spectroscopy
XRD	X-ray diffraction

## ACKNOWLEDGEMENTS

First, I would like to express my sincere thanks to my advisor Professor Junjie Niu. His patient advisory makes me learn a lot during my PhD study at UW-Milwaukee, which will also allow me to obtain further benefit during my following career. His attitude on research and study is always a good example for me to learn and follow. The time spend at UW-Milwaukee will be one of the most valuable experience and memory during my life.

Also, I would like to give my deeply appreciation to all the committee members, Professor Pradeep Rohatgi, Professor Benjamin Church, Professor Deyang Qu, and Professor Yi Hu, for serving as my thesis defense committee members. Their thoughtful suggestions and ideas helped me to accomplish the dissertation in a better way.

I would like to thank all our formal and current group members, including Dr. Yingying Lv, Dr. Shuai Kang, Dr. Fan Xia, Dr. Yongsuk Kim, Dr. Xi Chen, Dr. Boyang Liu, Dr. Bangxing Li, Dr. Cheng Feng, Dr. Melvin Samuel, Dr. Yuemei Ye, and all other group members, for their support, cooperation, and help. It is a great experience to work with them.

I also would like to acknowledge my deep gratitude to Dr. Steven Hardcastle at UWM AAF, Dr. Heather Owen at UWM biology department EM lab, Dr. Xinqi Chen at Northwestern University NUANCE, and all other stuffs who offered help during my PhD study.

Thanks to Dr. Lifeng Dong at Hamline University, Dr. Jin Liu at General Motors, and all my friends!

Finally, I would like to express my best thanks to my parents, my wife, and my daughters for your love and support. Your love is always my driving force!

# CHAPTER 1 INTRODUCTION

## 1.1 Development of Lithium-ion batteries

The development of energy techniques is becoming more and more important with the development of human society. Energy storage technique plays an important role in the application of energy. With the wide applications of numerous electric vehicles (EVs), portable devices, and other electric devices, the demand for high-performance rechargeable batteries has become more urgent in recent years. The strong desire for advanced energy storage techniques motivated the development of high-performance lithium-ion batteries (LIBs).

The history of the development of LIBs can be traced back to the rechargeable Li metal battery, which was published by Lewis and Keyes in 1913. In early 1970s, the original lithium-metal anode primary batteries with nonaqueous electrolytes, such as propylene carbonate-lithium perchlorate, and lithium negative electrodes were developed and introduced to the world, which opens the new pathway for the development of LIBs. Several different commercialized primary cells based on lithium-carbon monofluoride and lithium-manganese dioxide were also introduced by Matsushita and Sanyo, respectively, during 1973 to 1975. However, these types of primary Li metal cells were limited to be used only for small devices, such as LED fishing floats, cameras, and memory backup applications, due to the low energy density.<sup>3</sup>

To make LIBs with improved energy and power density, a lot of research efforts were spent on the development and optimization of the LIBs, including the search for a cathode and anode materials, optimization of the cell structure, development of electrolytes, *et al.*

### 1.1.1 Cathode

After comparison with other cathode materials, near metallic metal dichalcogenides, like  $\text{TiS}_2$  and  $\text{TaS}_2$  with layered structure were first introduced as cathode material to store Li-ions. The layered structure promotes enhanced cycling stability. However, the relative low voltage ( $\sim 2 \text{ V vs Li/Li}^+$ ), need of prelithiation, and safety issue limited the application for large packs.<sup>4</sup> To overcome these disadvantages, lithium cobalt oxide (LCO) was first introduced by Godshall *et al.* in 1980, which is regarded as the first appearance of modern layered metal oxide. After further optimization, the LCO cathode material can work at room temperature with organic electrolytes.<sup>4</sup> LCO had similar layered structure with  $\text{TiS}_2$ , which is favorable for the Li-ions insertion and extraction. Compared with  $\text{TiS}_2$  cathode, LCO showed high stability at ambient conditions, which largely increased the safety. At the same time, it performed higher voltage of 3.5-4 V vs  $\text{Li/Li}^+$ . Another advantage of LCO was the prestored lithium during the preparation process, which can match with anode material not limited to Li metal and provide more freedom for the choice of anode materials.

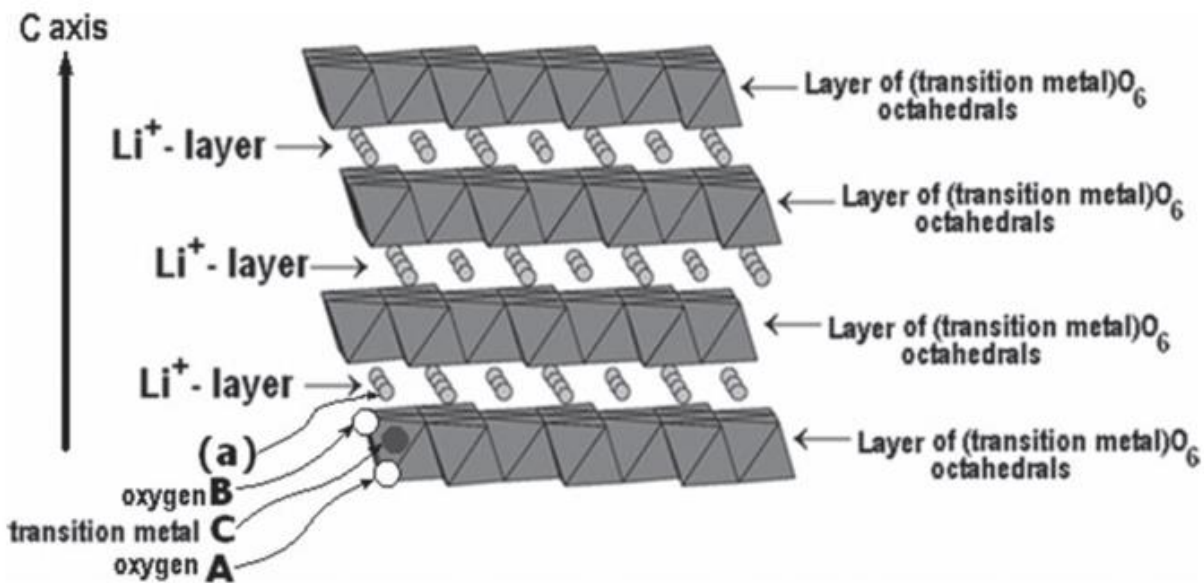


**Figure 1.1** Schematic illustration of the  $\text{LMO}_2$  with layered structure (Copyright 2007 Elsevier).<sup>5</sup>

The introduction of LCO with layered structure provides more ideas about the design of cathode material. Later, different kind of transition metal oxide with layered structure were developed,<sup>5</sup> such  $\text{LiNiO}_2$ ,  $\text{LiNi}_{1-x-y}\text{Co}_x\text{Mn}_y\text{O}_2$  (NMC), et al (**Figure 1.1**). Among various cathode materials, the Ni-rich cathode materials, such as  $\text{LiNi}_{0.8}\text{Co}_{0.15}\text{Al}_{0.05}\text{O}_2$  (NCA) and  $\text{LiNi}_{1-x-y}\text{Mn}_x\text{Co}_y\text{O}_2$  ( $x+y < 0.4$ ) have been widely investigated and regarded as one of the most promising cathode materials for next generation LIBs.

### 1.1.2 Anode

At the same time when researchers were looking for cathode materials, the search for safer and more stable anode materials to replace the pure Li metal was also under progress in parallel. Various kinds of material were explored as anode, including various alloy anode materials (including Si-Li, Sn-Li, and Li-Al) and  $\text{WO}_2$ .<sup>6</sup> However, most of them were discouraged by the large volume change upon lithiation, or some other problems. Among various candidates, carbon-based materials were thought to be the most promising, due to the high specific capacity of 372 mAh/g, high reversibility, and low lithiation potential.<sup>6</sup>

A lot of cell design based on carbon-based anode were reported. For example, high temperature molten salt cell coupling  $\text{LiC}_6$  graphite anode with metal sulfide cathode, ambient temperature cell using  $\text{LiC}_6$  anode and  $\text{NbSe}_3$  cathode in 1,3-dioxolane solvent with  $\text{LiAsF}_6$  salt electrolyte, graphite anode cell with a solid electrolyte. However, considering the practical application, none of them can be commercialized. Also, at that time, the organic decomposition layer separating the solid electrode from the liquid electrolyte on the surface of graphite was named as the solid electrolyte interphase (SEI). Following research also focused on the factors affecting the capacity and cyclability of graphite. It was found that the capacity of graphite anode is proportional to the graphitization, and the cyclability was related to the graphitization.

In 1987, Yoshino et al. built the new cell using soft carbon with reversible capacity of ~200 mAh/g as anode, coupling with the LCO discovered by Goodenough as cathode and carbonate-based electrolyte.<sup>6</sup> This has been widely accepted as the first LIB. After confirming the enhanced safety issue, the door to the commercialization of LIBs was opened. Sony Co. and A&T Battery Co. started the production of commercialized LIBs in 1991 and 1992, respectively.

### 1.1.3 Components and working principle of modern LIBs.

Currently, the modern LIB usually contains four main components: the cathode, anode, electrolyte and separator. During charge process, the lithium ions move from the cathode, through the electrolyte, to the anode, and move back during discharge process.

Currently, the most commonly used commercial cathode is the lithium-ion donor in the cathode, which is the main determinant of cell properties. There are several types of lithium metal oxides

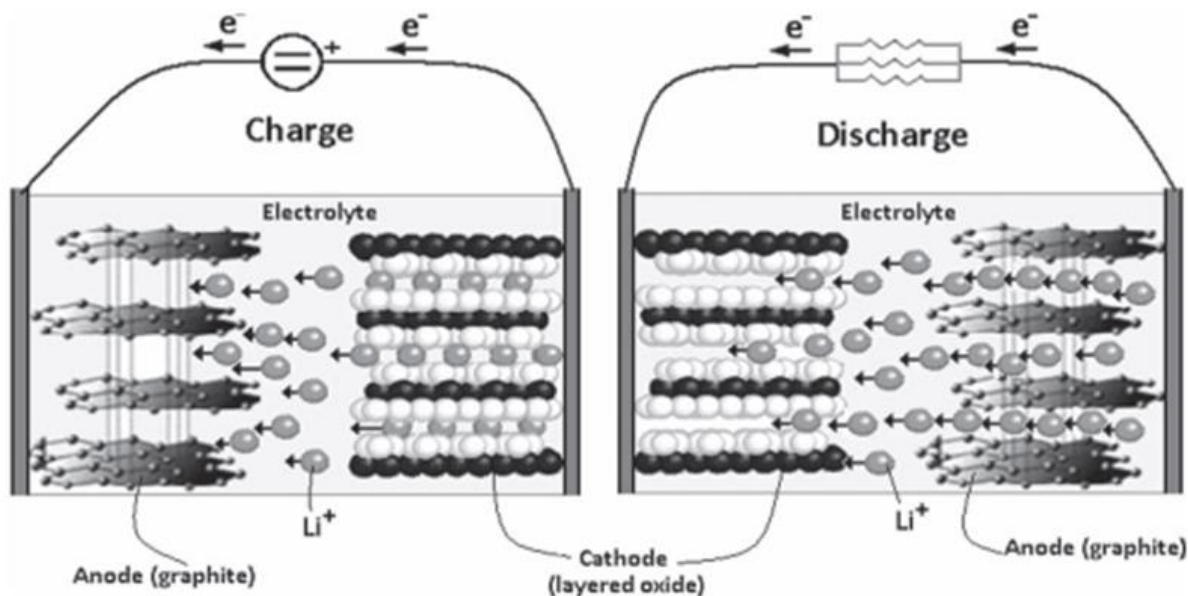


**Figure 1.2** Schematics of a typical Li-ion cell (Copyright © 2012 WILEY-VCH Verlag GmbH & Co. KGaA, Weinheim ).<sup>2</sup>

are used for this purpose: lithium cobalt oxide (LCO), lithium nickel manganese cobalt oxide (NMC), lithium nickel cobalt aluminum oxide (NCA), lithium manganese oxide (LMO), and lithium iron phosphate (LFP).<sup>7</sup> Graphite is the current dominant anode material for LIBs, due to its high stability and high capacity. Lithium titanate (LTO,  $\text{Li}_4\text{Ti}_5\text{O}_{12}$ ) is also used for some special LIBs, which can provide ultrahigh stability.<sup>3</sup>

Copper foil and aluminum foil are used as the current collector for anode and cathode, respectively. The active material with binder and conductive additives are coated on the current collector. The slurry was prepared through uniformly mixing active material, conductive additives, and binder (e.g., PVDF) in solvent (e.g., N-methyl-2-pyrrolidone). And the PVDF binder and N-methyl-2-pyrrolidone solvent (NMP) are usually replaced with carboxymethyl cellulose, styrene-butadiene rubber (SBR) binder, and water for the preparation of anode slurry considering about the cost.

The electrolyte is a mixture of lithium salt and organic solvents. Common lithium salts include lithium-hexafluorophosphate ( $\text{LiPF}_6$ ), lithium-perchlorate ( $\text{LiClO}_4$ ) and lithium-hexafluoroarsenate ( $\text{LiAsF}_6$ ). Common organic solvents include ethyl-methyl-carbonate, dimethyl-carbonate, diethylcarbonate, propylene-carbonate and ethylene-carbonate, which are vital for increasing the mobility of lithium ions. The quality of electrolyte will directly affect the performance of LIBs. Some additives can be used to improve the performance of LIBs, such as fluorinated ethylene propylene (FEC) and vinylene carbonate (VC).<sup>1</sup>

The separator is a safety component between the cathode and the anode, preventing direct contact, i.e. short-circuiting, while being permeable to lithium ions. The most common separator materials are polyethylene and polypropylene.

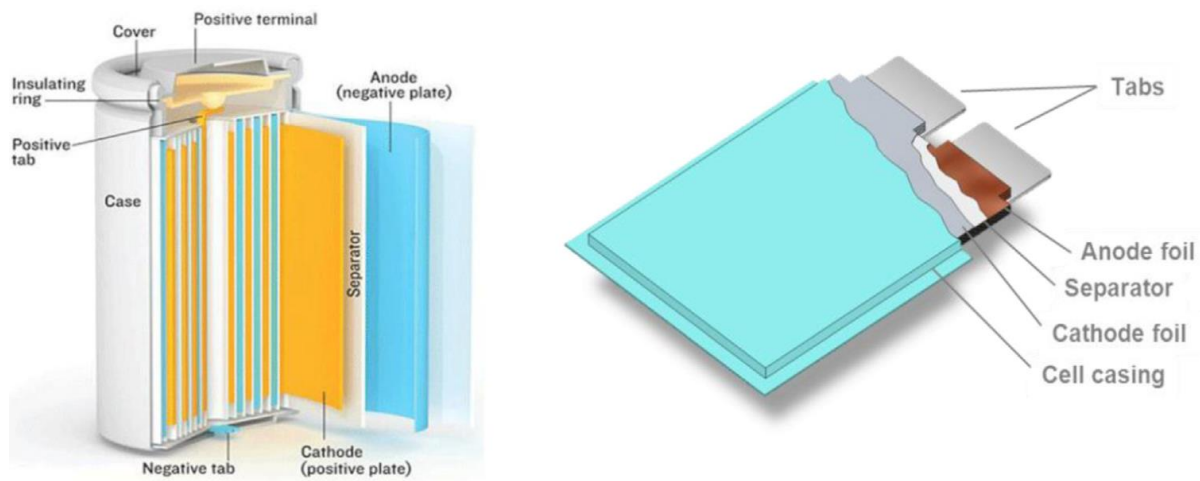


**Figure 1.3** Li-ion battery cell configurations (Copyright 2018, Elsevier).<sup>1</sup>

Li-ion battery cells are usually manufactured as cylindrical or stack cells. In the stack configuration, the cathode, anode and separator are enclosed in laminate film (**Figure 1.3**). In the cylindrical configuration, the layers are rolled and sealed in a metal can. Both configurations are used to produce different standard cell sizes, such as 18650. When applied for different area, the LIBs can be made into different shapes. For example, they can be manufactured into flexible for wearable electronics or devices with polymer case.

## 1.2 Development of Cathode

### 1.2.1 Current state of art in Ni-rich cathode material

As one of the most promising energy storage devices, lithium-ion batteries (LIBs) have been widely used as the power source for various portable electric devices and EVs and hybrid electric vehicles (HEVs).<sup>8-10</sup> The electrochemical performance, especially the energy density of LIBs poses an important effect on the development of EVs and HEVs, which mainly affect the driving range and charge frequency.<sup>11, 12</sup>

As an important component in LIBs, cathode material is regarded as the major limiting factor for the energy density of LIBs.<sup>7, 13, 14</sup> Currently, the majority of cathodes used in LIBs is  $\text{LiFePO}_4$  (LFP) and  $\text{LiNi}_{1-x-y}\text{Mn}_x\text{Co}_y\text{O}_2$  ( $x+y<0.5$ ) (NMC) family, such as  $\text{LiNi}_{1/3}\text{Mn}_{1/3}\text{Co}_{1/3}\text{O}_2$  (NMC111) and  $\text{LiNi}_{0.5}\text{Mn}_{0.3}\text{Co}_{0.2}\text{O}_2$  (NMC532).<sup>15-17</sup> Among these cathode materials,  $\text{LiNi}_{0.5}\text{Mn}_{1.5}\text{O}_5$  can only provide a moderate energy density. But it is regarded as one of the most promising cathode materials for high power density, due to the high operating voltage of 4.7 V vs  $\text{Li}/\text{Li}^+$  when cooperated with appropriate electrolyte. Lithium-rich manganese based  $\text{Li}_{1+x}\text{M}_{1-x}\text{O}_2$  is showing great potential with high specific capacity of  $\sim 250$  mAh/g. However, the voltage fading and capacity decay caused by the intrinsic layered to spinel phase transition still limit its practical application. The polyanion-based compounds provide high voltage but low power and energy

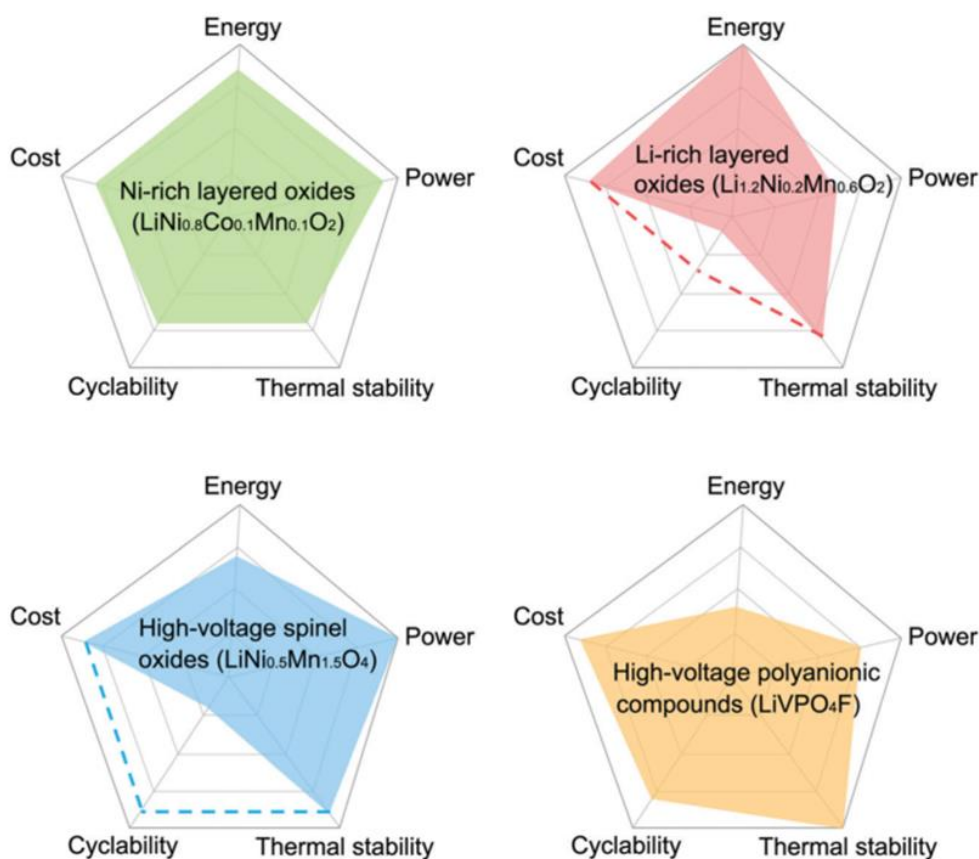


**Figure 1.4** Radar plots comparing various classes of high-voltage positive electrode materials with one example composition in terms of energy density (volumetric), power, cyclability (with commercial carbon-based negative electrodes), cost and thermal stability. The electrochemical performance of  $\text{LiVPO}_4\text{F}$  is based on solely the  $\text{V}^{3+}/4+$  redox couple. Dashed lines exhibit the cyclability of the two samples ( $\text{Li}_{1.2}\text{Ni}_{0.2}\text{Mn}_{0.6}\text{O}_2$  and  $\text{LiNi}_{0.5}\text{Mn}_{1.5}\text{O}_4$ ) obtained in Li-metal half cells (Copyright 2017, The Royal Society of Chemistry).<sup>7</sup>

density due to heavier formula weight, inadequate intrinsic electronic/ionic transport, and lower powder packing density (**Figure 1.4**).<sup>7</sup>

To meet the requirement of high energy density of LIBs from the development of EVs, it is important to improve the upper cutoff voltages, the capacity and active material loading. Currently, the Ni-rich cathode materials including  $\text{LiNi}_{0.8}\text{Co}_{0.15}\text{Al}_{0.05}\text{O}_2$  (NCA) and  $\text{LiNi}_{1-x-y}\text{Mn}_x\text{Co}_y\text{O}_2$  ( $x+y < 0.4$ ) have been widely and deeply investigated and studied. It has been regarded as a class

of promising cathode material and attracting considerable attention due to high capacity of above 200 mAh/g and the average high discharge potential of 3.8 V (vs Li<sup>+</sup>/Li).<sup>16, 18, 19</sup> However, some challenges related to the poor cycling stability and rate capability of Ni-rich oxide cathode materials still need to be addressed before they can compete in practical implementation.<sup>16, 20</sup> The reasons resulting in performance fading are originated from the Li<sup>+</sup>/Ni<sup>2+</sup> cation mixing,<sup>21, 22</sup> Li residues on the surface,<sup>15, 23</sup> overcharging,<sup>24, 25</sup> exposing to high temperature,<sup>26, 27</sup> crystal orientation of the secondary particles,<sup>28, 29</sup> et. al. Cycling lifetime and safety issue have become the biggest problems and research focus for Ni-rich cathode material like NMC and NCA.<sup>30-32</sup>

Several strategies have been applied to mitigate the structural/interfacial degradation of Ni-rich cathodes to improve the electrochemical especially the cycling capability.

**(i) Element doping**

Element doping has been proved to be an effective strategy to decrease Li/Ni disordering in the Ni-rich cathode materials through increasing the structural stability and impeding the intergranular

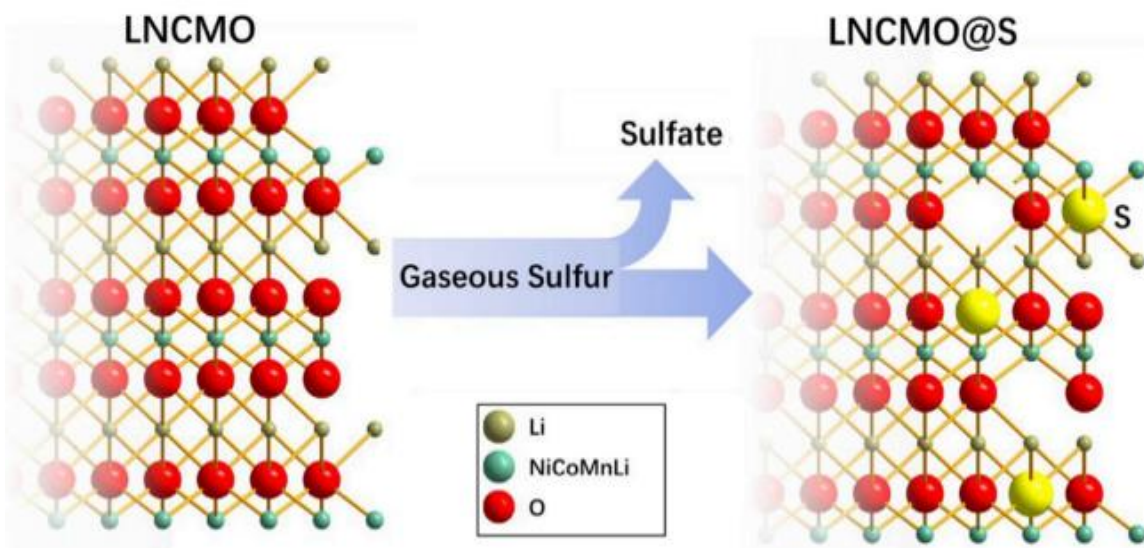


**Figure 1.5** The partial O replacement doped by S in the lattice of Li<sub>1.2</sub>Ni<sub>0.13</sub>Co<sub>0.13</sub>Mn<sub>0.54</sub>O<sub>2</sub> (Copyright 2019, Elsevier).<sup>50</sup>

cracks in secondary particles.<sup>33-35</sup> Tina et al.<sup>36</sup> analyzed the effect of doping  $\text{LiNi}_{0.8}\text{Co}_{0.1}\text{Mn}_{0.1}\text{O}_2$  with various cations, including  $\text{Mg}^{2+}$ ,  $\text{Al}^{3+}$ ,  $\text{Si}^{4+}$ ,  $\text{Ti}^{4+}$ ,  $\text{Zr}^{4+}$ , and  $\text{Ta}^{5+}$  through a fast screening methodology. Through substitution of mobile ions, such as  $\text{Ni}^{2+}$  and  $\text{Li}^+$ , with structurally and (1) electrochemically monovalent, static ions,<sup>37,38</sup> (2) hindrance of  $\text{Ni}^{2+}$  ion migration to the Li layers,<sup>39,40</sup> (3) decrease of oxygen release during electrochemical cycling by increasing oxygen and transition metal (TM) ion bond strength,<sup>41,42</sup> and (4) increase in strength of the transition metal–oxide bond, which limits the contraction of the material at the end of charge when the  $\text{Ni}^{\text{IV}}\text{–O}$  bond becomes highly covalent, reducing  $\text{O}^{2-}$  repulsion.<sup>43,44</sup> As the cation doping sites are difficult to control due to the coexistence of several transition metals with different oxidation states in the transition metal layer, the dopant concentration needs fine optimization.<sup>37,45</sup> The effects of Al and Mg doping on oxygen evolution and structural stability in NMC811 were analyzed using first-principle calculations. The most energetically stable site with Al doping is Ni-site, followed by Co-, Li-, and Mn- sites. While Mg doping usually occupies the Li-site. Al doping can significantly prevent the oxygen evolution under a broad range of delithiation stages and various defects. Mg doping is effective on avoiding the formation of cation-disordered structures on the fully lithiated structure. Except cation doping, anion doping was also proved to be effective and relatively easy to improve the electrochemical performance of Ni-rich and Li-rich cathode materials. Doping of F<sup>-</sup> anions can stabilize the crystal structure by forming F-M (Ni, Co and Mn) bonds.<sup>45,46</sup> Due to the relative weaker Li-S bonds, S<sup>2-</sup> displays great potential in enhancing the ionic conductivity of Li- and Ni-rich cathode materials.<sup>47-49</sup> Zhang et al performed S doping on Li-rich ( $\text{Li}_{1.2}\text{Ni}_{0.13}\text{Co}_{0.13}\text{Mn}_{0.54}\text{O}_2$ ) and Ni-rich (NMC811) cathode materials (**Figure 1.5**).<sup>50</sup> During the preparation process, part of sulfur atoms were reduced and occupied the oxygen sites, inducing the increment of unit cell parameters. The rest reacted with the oxygen and lithium atoms extracted

from cathode material, forming sulfate species in situ accompanied by the appearance of oxygen vacancies at the surface region. The migration energy barriers of Li ions in S doped  $\text{Li}_{1.2}\text{Ni}_{0.13}\text{Co}_{0.13}\text{Mn}_{0.54}\text{O}_2$  (0.53 eV) is much lower than that of undoped (0.71 eV). The doped cathode material displayed improved cycling and rate capability.

## (ii) Surface coating

To reduce the reaction between the electrode surface and the electrolyte, surface coating is regarded as an effective approach to separate the bulk materials from the electrolyte solution.<sup>51-</sup>  
<sup>54</sup> At the same time, the coating layer can provide structural support to the cathode material and also prevent the surface phase transformations from a layered to disordered spinel and rock-salt structures, which are produced from the parasitic reactions between the highly oxidized  $\text{Ni}^{4+}$  and

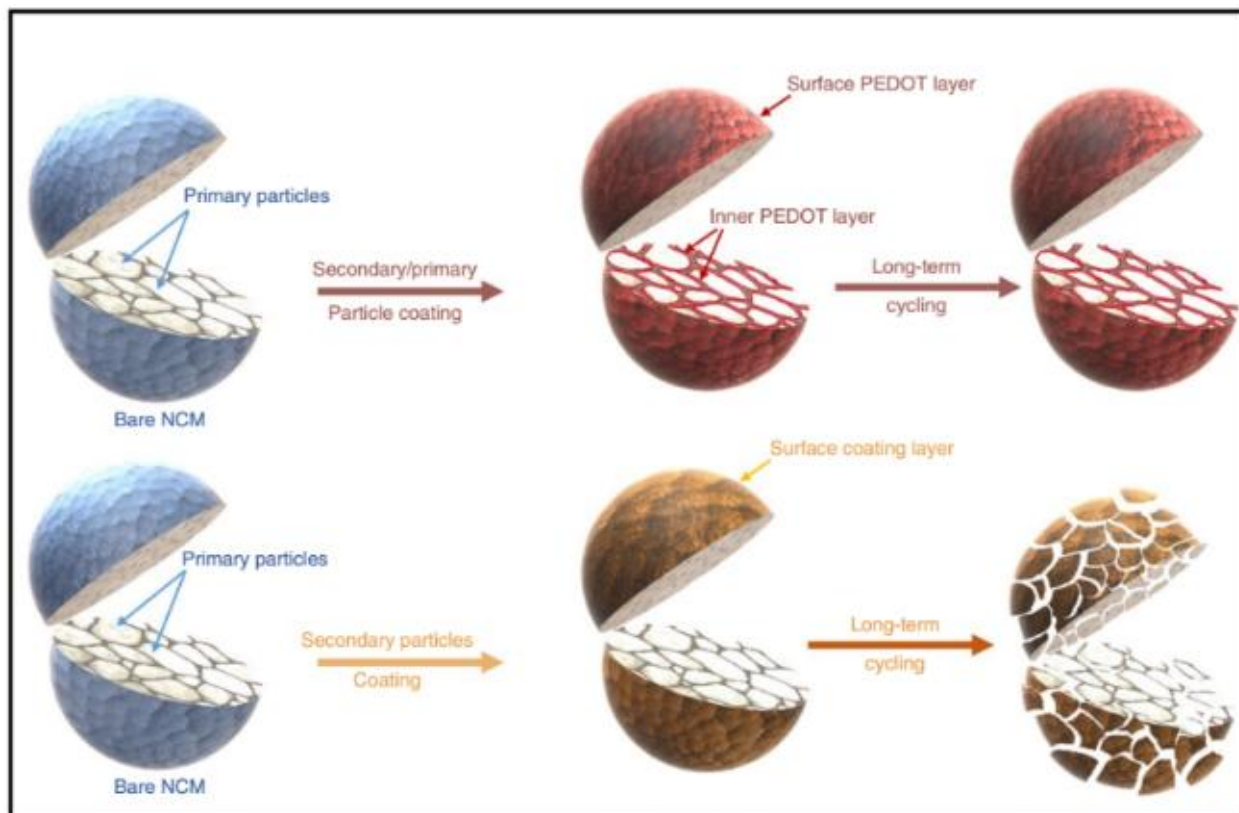


**Figure 1.6** Schematic illustration of the stability improvement through coating on both secondary/primary particle via oCVD (Copyright 2019, Nature Publishing Group).<sup>67</sup>

the electrolyte, as well as the oxygen removal, especially in the highly delithiated state, enhancing the cycle lifetime of cathodes. Currently, materials commonly used as the protective coating layer include lithium salt like  $\text{Li}_3\text{PO}_4$ ,<sup>55, 56</sup>  $\text{LiFePO}_4$ ,<sup>57, 58</sup> conductive polymers like polypyrrole,<sup>59, 60</sup> and metal oxides, including  $\text{SiO}_2$ ,<sup>61, 62</sup>  $\text{ZrO}_2$ ,<sup>63, 64</sup>  $\text{Al}_2\text{O}_3$ .<sup>65, 66</sup> It is an effective strategy to suppress the increase of interfacial resistance during cycling through separating electrode from the corrosion of the electrolyte.

However, coating only on secondary particles cannot absolutely prevent the penetration of electrolyte along the grain boundaries. It is believed to be more effective to apply protection to both the primary and secondary particles. Recently, a unique coating on both secondary and primary particles of layered NMC was reported by Xu et al.<sup>67</sup> In this approach, solid electrolyte

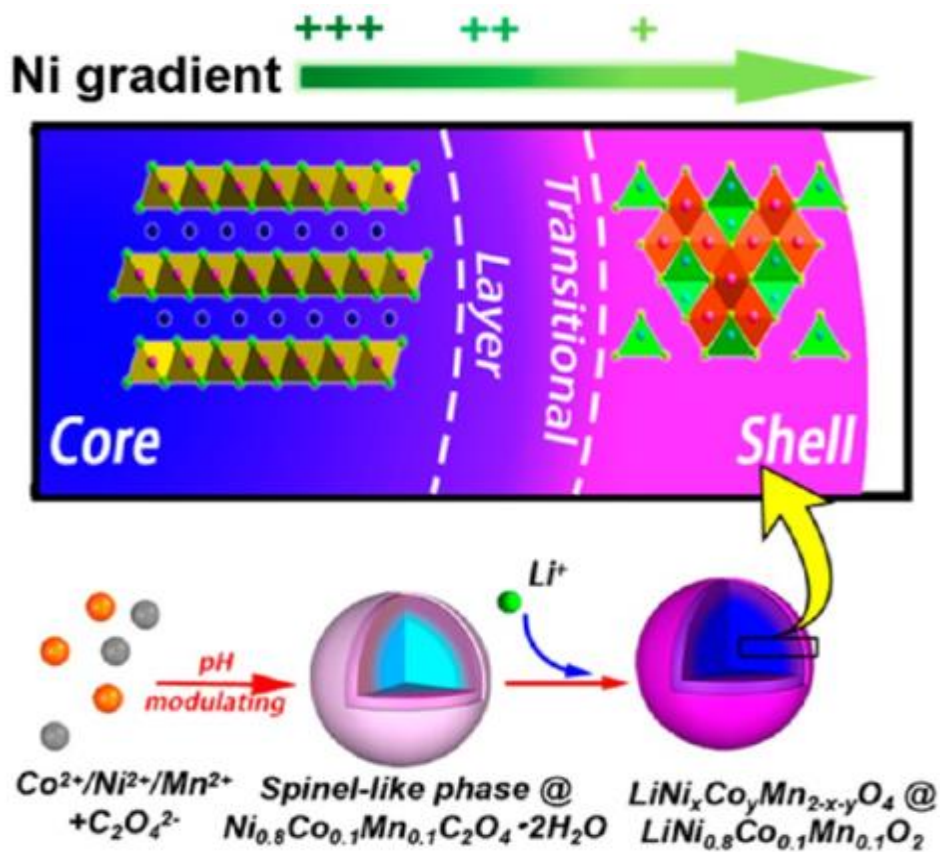


**Figure 1.7** Schematic illustration of the Ni-rich  $\text{LiNi}_{0.8}\text{Co}_{0.1}\text{Mn}_{0.1}\text{O}_2$  with Ni concentration gradient (Copyright 2017, American Chemistry Society).<sup>68</sup>

$\text{Li}_3\text{PO}_4$  was applied to cover both the primary and secondary particles using oxidative chemical vapor deposition (*oCVD*) technique (**Figure 1.6**). After a long-time cycling, the PEDOT (Poly(3,4-ethylenedioxythiophene)) protective layer can successfully enhance the structural stability, and also stabilize the interface between cathode material and electrolyte without affecting the lithium ions and electrons transportation.

### (iii) Other approaches

By controlling the gradual change of the pH value in the synthesis of precursor, Zhang et al<sup>68</sup> successfully constructed NMC811 with Ni gradient concentration and an atom-scale integrated hierarchical spinel coating layer on the surface (**Figure 1.7**). The  $\text{Li}^+/\text{Ni}^{2+}$  cation disordering decreased from 3.26% for the normal NMC811 to 1.94% for the NMC811 with Ni concentration

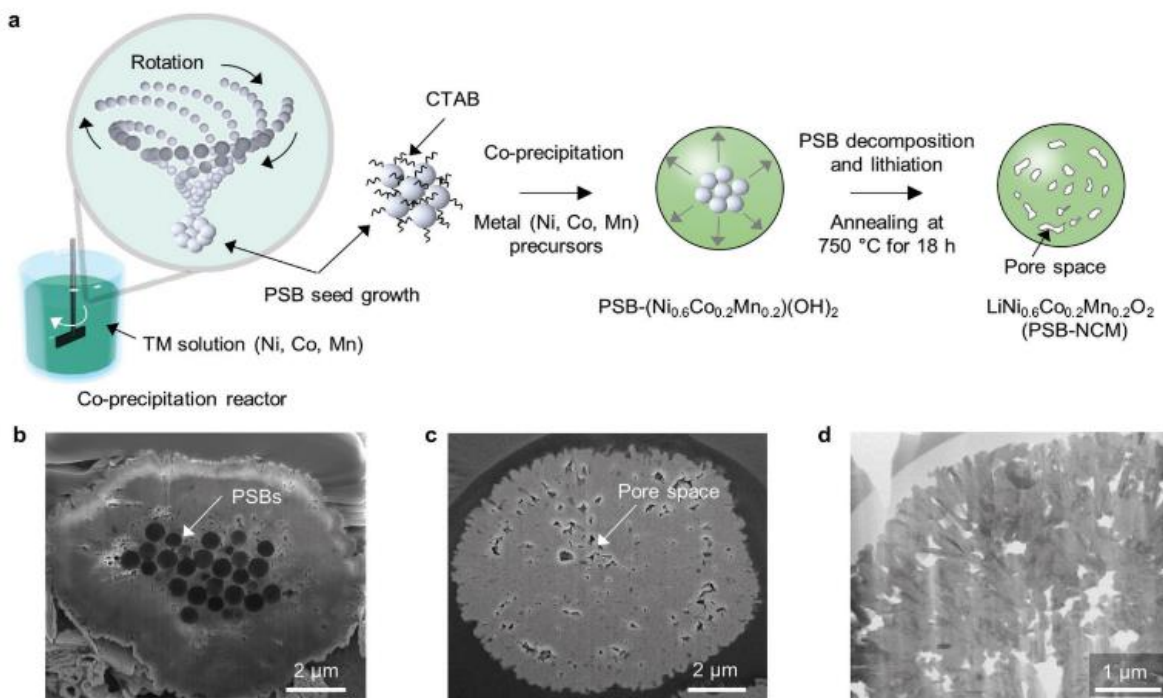


**Figure 1.8** a) Schematic of the synthesis process of porous  $\text{LiNi}_{0.6}\text{Co}_{0.2}\text{Mn}_{0.2}\text{O}_2$  by coprecipitation method with polystyrene beads (PSBs) and corresponding cross-sectioned SEM images of (b) precursor and (c) lithiated PSB-NMC. d) A HAADF-STEM image showing the high magnified cross-sectioned PSB-NCM (Copyright 2017, Wiley-VCH GmbH, Weinheim).<sup>69</sup>

gradient. As a result, the structure stability and long-term storage is substantially improved. The electrochemical performance on the cycling stability (92.7% vs 62.9%, 100 cycles), rate capability (111.7 vs 13.9 mA h/g, 10 C), and low-temperature performance (156.6 vs 92.8 mAh/g; 93.2% vs 43.2%, 100 cycles, -20 °C) compared with the typical NMC811.

The concentration gradient of Ni has been demonstrated to be effective on improving the structural stability and electrochemical performance. Sacrificial polymeric (polystyrene) beads were introduced in the coprecipitation of  $\text{Ni}_{0.6}\text{Co}_{0.2}\text{Mn}_{0.2}(\text{OH})_2$  (**Figure 1.8**).<sup>69</sup> The well dispersed polystyrene beads react as the reaction seed for the coprecipitation of the  $\text{Ni}_{0.6}\text{Co}_{0.2}\text{Mn}_{0.2}(\text{OH})_2$  and become the core of the core of the cathode materials. During the calcination, the carbonization and decomposition of polystyrene beads in the core that promote the decrease of Ni oxidation state and transition metals concentration gradient in the primary particles. At the same time, some inner pores produced during this process can effectively accommodate the volume change during the lithiation/delithation.

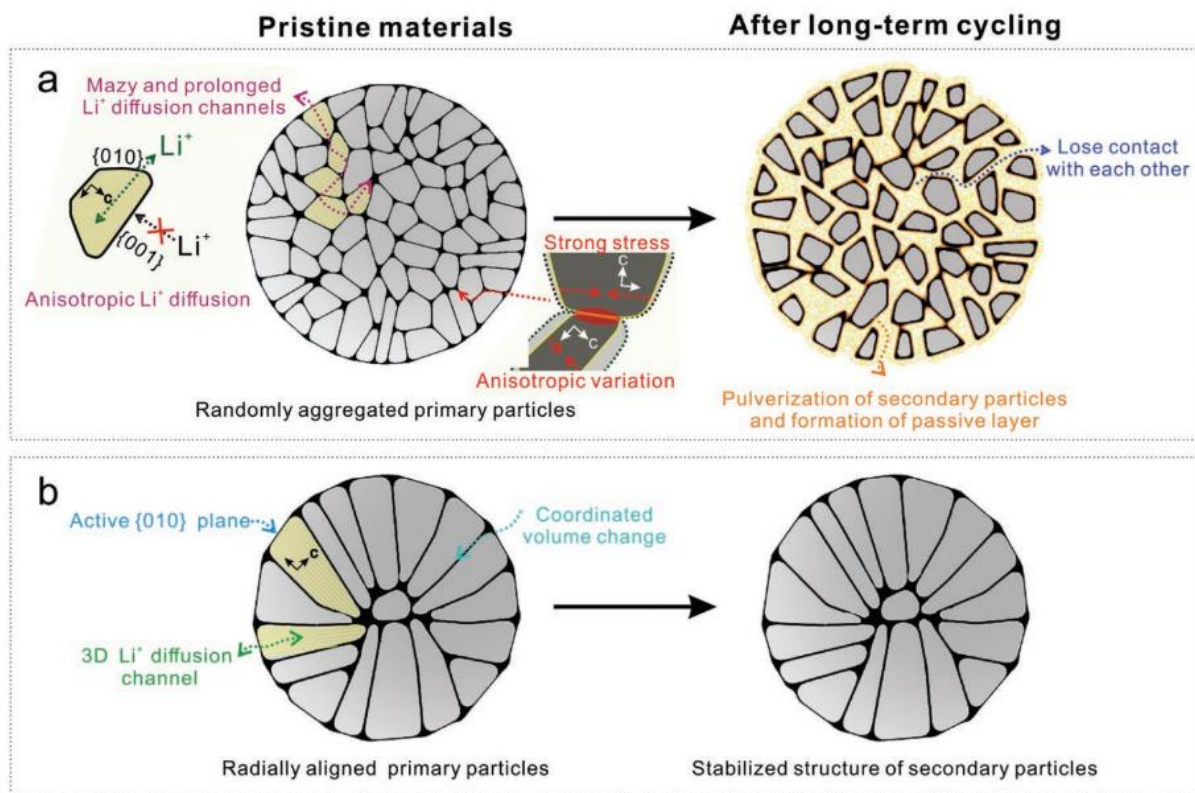


**Figure 1.9** Schematic illustration of the structure and characterization of (a) commercial NMC and (b) Ni-rich  $\text{LiNi}_{0.8}\text{Co}_{0.1}\text{Mn}_{0.1}\text{O}_2$  cathode material with radially aligned single-crystal primary particles (Copyright 2019, Wiley-VCH GmbH, Weinheim).<sup>72</sup>

**Crystal orientation of primary particles:** Most spherical NMC particles are aggregated densely by many randomly oriented primary nanoparticles (**Figure 1.9a**).<sup>20, 28, 29</sup> It is believed that the micrometer-sized secondary particles have a lot of drawbacks. First,  $\text{Li}^+$  can only diffuse along the 2D (010) plane among the hexagonal-layer structure.<sup>70</sup> The  $\text{Li}^+$  exchange at the electrode/electrolyte interface is hindered and  $\text{Li}^+$  diffusion pathway inside secondary particles is prevented by the randomly oriented primary nanoparticles. Second, microstrains at the boundaries of primary particles are generated as a result of the asynchronous volume change due to the substantial anisotropic lattice expansion/contraction during the repeating  $\text{Li}^+$  insertion/extraction

process, particularly with the increased Ni content.<sup>71, 72</sup> Optimization on the crystal orientation is proved to be effective to improve the performance of Ni-rich cathode material (**Figure 1.9**).<sup>72</sup>

### 1.2.3 Rationale of Ni-rich cathode material modification

Recently a novel concept of full transition metal concentration-gradient is attracting more and more attention.<sup>73-76</sup> Zhang et al synthesize Ni-rich  $\text{LiNi}_{0.8}\text{Co}_{0.1}\text{Mn}_{0.1}\text{O}_2$  through atom-scale interfacial integration of self-forming hierarchical spinel layer with Ni gradient concentration.<sup>68</sup> Full concentration-gradient of Mn-rich phase with long rod-shaped primary particles was also reported.<sup>76-78</sup> The reported cathode materials with transition metal gradient displayed enhanced electrochemical performance and structural stability. The specific capacity of cathode material is related to the Ni concentration.<sup>31</sup> However, when Ni-rich cathode materials are charged to high voltage, plenty of unstable  $\text{Ni}^{4+}$  ions will be reduced to form a stable and inactive NiO phase on the surface.<sup>79, 80</sup> As a result, the interfacial impedance will increase to have a poor cycling lifetime.<sup>81, 82</sup> In the same time, the reaction of  $\text{Ni}^{4+}$  with electrolyte can also lead to structural degradation and electrolyte decomposition.<sup>77</sup> The co-formed oxygen and thermal behavior will have safety issues with flammable electrolytes.<sup>83, 84</sup> Compared with  $\text{Ni}^{4+}$ ,  $\text{Mn}^{4+}$  is believed to be more stable and not involved in redox reaction. Through the construction of decreased Ni concentration from center towards outer layer of the secondary particle, two-electron reaction ( $\text{Ni}^{2+} \rightarrow \text{Ni}^{4+}$ ) on charging can be effectively suppressed by the Mn-rich layer.<sup>73, 85</sup>

The gradient structure can be synthesized using co-precipitation methods by continuously changing the precursor concentrations.<sup>76-78</sup> The surface modification and preparation of precursors can be combined in one step to create Ni gradient by pH modulating.<sup>68</sup> For most of the reported results, Ni-gradient of the secondary particles was created.<sup>86-88</sup> It was also found that transition metal concentration can be adjusted by introducing organic seeds.<sup>69</sup> During the high-temperature

calcination, the organic molecules are carbonized and decomposed by oxidization to react with transition metals of the primary particles. As a result, it forms the gradual decrease of Ni oxidation state and transition metal concentration in the primary particles are gradually decreased.

## 1.3 Development of Anode materials

Anode material also plays an important role in the development of high-performance LIBs. Graphite has been widely used as the anode material for LIBs due to its high reversibility and low cost since it was introduced to the LIBs. However, as the conventional commercialized anode material, graphite cannot satisfy the current requirement of high energy density and high power density for advanced LIBs, due to its relative low capacity, 372 mAh/g (LiC<sub>6</sub> state).<sup>89,90</sup> With the demand for LIBs with high energy and power density, the research on advanced anode material has also been attracting more and more attention during the past decades.

### 1.3.1 Silicon anode

Compared with carbon, other elements in group IV with higher theoretical capacities, including silicon, germanium and tin, are considered as promising anode candidates for next-generation LIBs. Among various anode materials, silicon is attracting tremendous attention due to several advantages. First, silicon presents a theoretical specific capacity of around 4200 mAh/g, which is almost 10 times higher than graphite. Second, the discharge potential plateau is around 0.4 V vs Li/Li<sup>+</sup>, which is beneficial for higher working potential when coupled with cathode material, leading to high energy density. Third, the price of Si is relatively low due to the abundant presence on earth. All these advantages make Si one of the most promising anodes for the next-generation LIBs.<sup>91,92</sup> Regarding to these specificities, recently efforts have been made in developing a series of new designs on nano-structured silicon.<sup>93-97</sup>

However, behind the advantages, there are also several disadvantages limiting the practical application of Si for LIBs:

(1) Large volume change during lithiation/delithiation, leading to high internal stress and pulverization of Si morphology. Experimental and simulation studies found a large volume expansion (>280%) of Si upon lithiation and revealed a sharp interface between the fully lithiated shell and the Si crystal core and crystal orientation dependent expansion.<sup>98</sup>

(2) The sever pulverization leads to electrical contact loss of active material from surrounding particles, conductive network, and the current collector. As a result, increased internal electrical resistance will be caused by this self-isolation of the active material.

(3) The large volume changes and pulverization would result in the repeating formation of unstable thick SEI. A thin passivating SEI layer can protect the electrolyte from direct contact with Si and avoid further decomposition. The continuous formation of SEI leads to block of the electron flow and excessive decomposition of electrolyte and consumption of Li ions. A stable SEI is crucial for the long cycling of Si electrodes.<sup>99</sup>

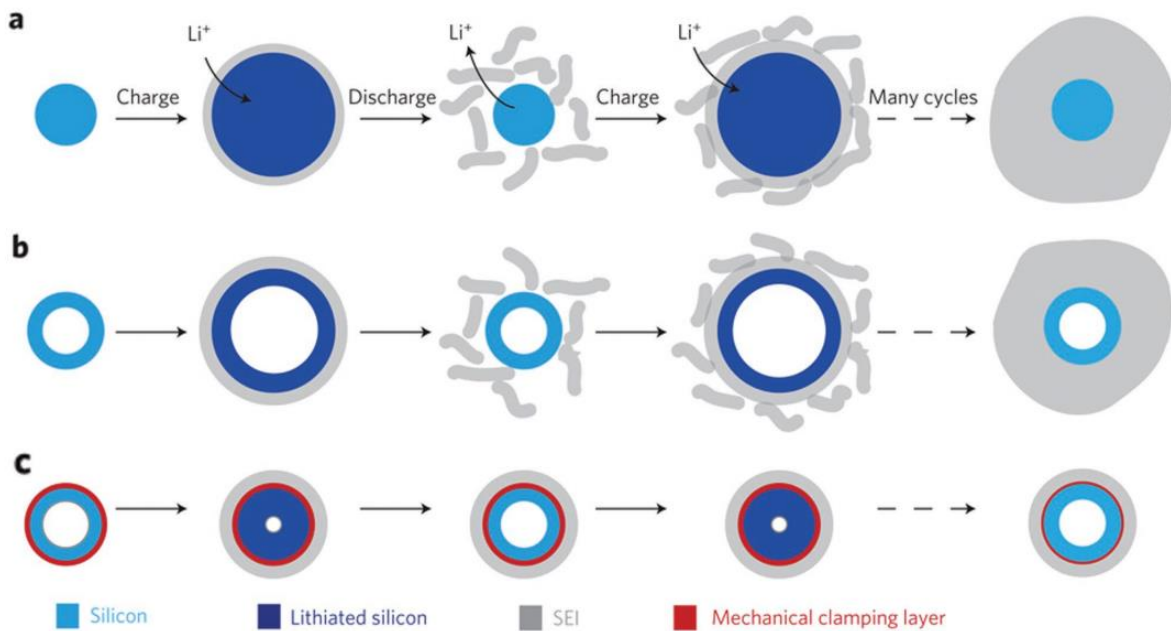


**Figure 1.10** Schematic illustration of the lithiation process of a) solid nanowires, with repetitive SEI formation on the surface after cycling, b) Si nanotubes, with a similar outcome that SEI continues to grow upon the shrinking and expansion of the nanotubes, and c) Si nanotubes with a mechanical constraining layer on the surface, where a thin and stable SEI layer is built. Reproduced with permission (Copyright 2012, Nature Publishing Group).<sup>101</sup>

Numerous works have been on applied on the effort to accommodate the huge volume change of Si during cycling to overcome the rapid capacity decay and poor cycling stability which is a limits the practical applications of Si anode (**Figure 1.10**).<sup>90, 100, 101</sup>

### 1.3.2 Si nanostructure.

Si nanoparticles or nanostructures have been regarded one of the most promising design to better capability in accommodating the volume change of Si during cycling due to larger specific surface area and higher average binding energy per atom at the surface.<sup>102</sup> The battery cycling capability

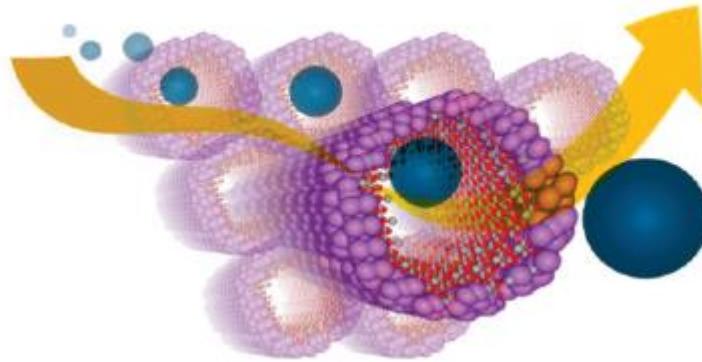


**Figure 1.11** Schematic illustration of the Li-ion pathway in Si nanotube (Copyright 2009, American Chemistry Society).<sup>110</sup>

has been largely improved through constructing various nano-structured silicon, for instance, nanowires,<sup>103</sup> nanospheres<sup>104</sup> and nanotubes.<sup>105</sup>

Commercial available Si nanoparticles were treated through boron doping and  $\text{AgNO}_3/\text{HF}$  etching to create the porous structure with improved specific surface area, which was measured to be more than  $60 \text{ m}^2/\text{g}$ .<sup>106</sup> When applied as anode for LIBs, both the cycling stability and rate performance were significantly improved. Si with hierarchical porous-hollow structure was synthesized through reduction of  $\text{SiO}_2$  with Mg. The specific capacity of  $1200 \text{ mAh/g}$  at  $0.5 \text{ C}$  and  $1850 \text{ mAh/g}$  at  $0.1 \text{ C}$ , and obviously improved cycling stability were achieved during electrochemical performance test in coin cells. In situ TEM was also applied to confirm the working mechanism, where the lithiation of Si starts from the surface and propagates inward, and the volume expansion of the inner Si happens toward the center of the sphere and shrinks the hollow core.<sup>107</sup> Porous network was also applied to Si to sponge to accommodate the volume expansion.<sup>108</sup> Si nanowires and nanotubes were also successfully applied as anode material for LIBs.<sup>109</sup> The unique benefit of 1D structure can significantly accommodate the volume change of Si. Especially, the nanotubes are

able to provide higher specific surface area, where the hollow space inside the tube allow the release of the produced volume expansion inward and outward (**Figure 1.11**).<sup>110</sup>

The researchers also reported a scaffold that is comprised of Si nanoparticles, S-doped graphene and polyacrylonitrile, to protect the Si while preserving the conductivity.<sup>111</sup> To improve the electrical conductivity, carbon was always used to serve as the coating layer on the surface of Si nanostructures.

However, there are still some limitations from nanostructured Si cannot be solved, which affect the commercialization of Si nanomaterial as anode material for LIBs. First is the relatively low active mass loading of nanomaterials, limiting the energy density of LIBs. Second, most of the Si nanomaterials under high mass loading would result in severe pulverization, solid-electrolyte-interface (SEI) growth and contact loss. As a result, the cyclability and rate performance are affected a lot. Also, the low packing density, the complex synthesis rote, and the unstable quality control of Si nanoparticles during scale-up production is still challenging, limiting the commercialization of Si nanomaterials.<sup>112</sup>

### **1.3.3 Micrometer-sized Si**

Compared with Si nanoparticles, micrometer-sized Si particles is believed more practical as anode for LIBs. Micrometer-sized Si can significantly improve the packing density and reach high mass loading when applied as anode. At the same time, the production is relatively simple compared with that of Si nanomaterials, which can reduce the production cost. Si with increased size, which is also able to maintain high cyclability and high active material loading is considered as a promising direction for mass production of LIBs with high volumetric and gravimetric energy densities, *e.g.*, over 500 Wh/kg.<sup>113-115</sup> How to improve the cycling stability of large Si particles,

while maintaining high mass loading became the focusing point of the application of micrometer-sized Si. One promising strategy is to artificially design the micrometer-sized structure with characteristics of nanosized Si, which cannot only preserve the unique advantages of nanosized Si, but also eliminate the associated drawbacks of the nanomaterial. Under the direction of this strategy, basically two methodologies were successfully performed. One is micrometer-sized 3D structure of Si with nanocharacteristics, including nanopores, nanograins. The other one is incorporating nanosized Si onto a micrometer-sized host, such as graphite, graphene, and various carbon frameworks.

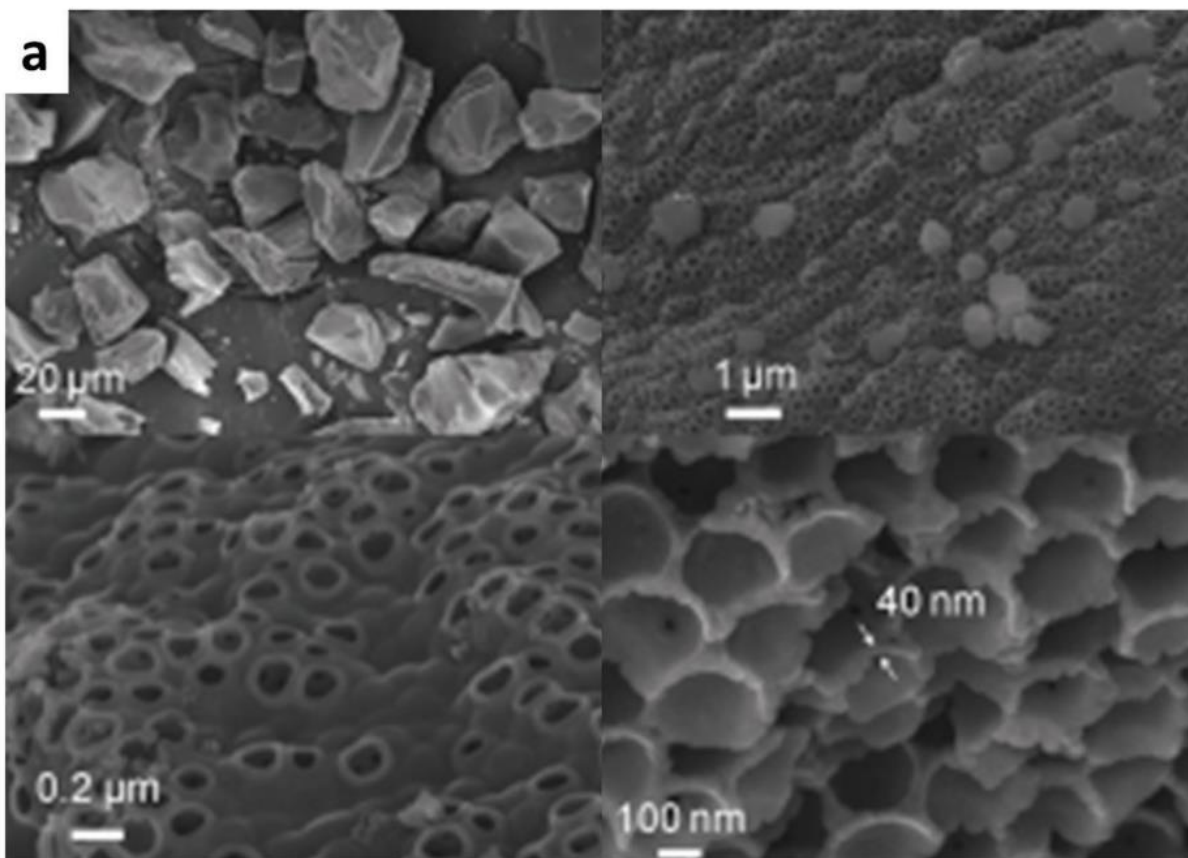


**Figure 1.12** SEM images of 3D porous Si-C particles at different magnification (Copyright 2008, Wiley-VCH GmbH, Weinheim).<sup>116</sup>

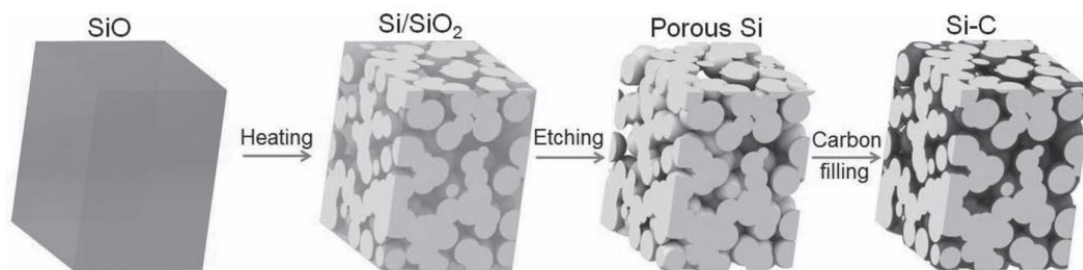


**Figure 1.13** The preparation process from SiO precursor to the Si-C composite (Copyright 2013, Wiley-VCH GmbH, Weinheim).<sup>117</sup>

Bulk Si with particle size ranged from several to 100  $\mu\text{m}$  was prepared (**Figure 1.12**). A huge number of “octopus-foot-like” voids were created on the bulk structure, with thickness of Si walls being around 40 nm, leading to high specific surface area of 158  $\text{m}^2/\text{g}$ . The benefits from both 3D Si nanowalls and large number of nanopores promotes superior capacity retention and good rate performance.<sup>116</sup> Another work demonstrates the typical synthesis process of the Si-C composite. Basically, porous Si was obtained through heating and etching process of SiO bulk material. Then carbon was filled in the pores of the obtained porous Si to improve the conductivity and serve as buffers to accommodate the volume change upon lithation/delithiation process (**Figure 1.13**).<sup>117</sup>

Another method is to incorporate the Si nano particles into conductive host. Among various host material, graphite, as the widely used anode material for LIBs, is considered as a good candidate as a host material to load Si nano particles due to its high cycling stability, low cost, and high conductivity. Si-nanolayer-embedded-graphite was prepared through deposition of Si on both the surface and internal pores of graphite via a CVD process.<sup>95</sup> With this unique design, the uniformly distributed Si nanoparticles can significantly improve the capacity of the composite. At the same time, the graphite with pores can improve the conductivity and provide sufficient space to

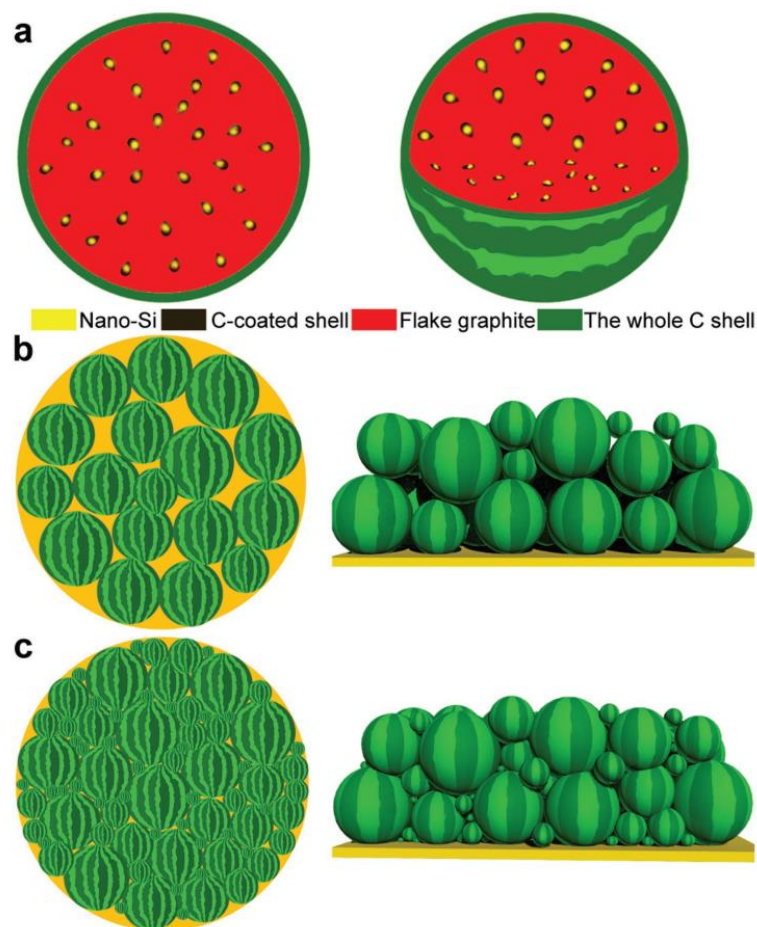


**Figure 1.14** Schematic illustration and packing status with different size distribution of the watermelon-inspired Si/C microspheres (Copyright 2017, Wiley-VCH GmbH, Weinheim).<sup>118</sup>

accommodate the volume change. A thin layer of carbon coated on the surface of Si can enhance both the ionic and electric conductivity. Based on the testing result, the total specific capacity of the composite can increase to 517 mAh/g with 6 wt% of Si addition, ensuring it as a promising candidate as anode for the LIB with high energy density.

Another interesting configuration is like watermelon (**Figure 1.14**), where the Si nanoparticles were uniformly distributed in the matrix of flake graphite, and another thin layer of conductive carbon was coated on the out surface to increase the conductivity and maintain the closely packing

of the microspheres.<sup>118</sup> Under this design, the tap density of the Si/C composite was measured to be 0.88 g/cm<sup>3</sup>, which is much higher than that of the Si nanoparticles, ensuring a high active mass loading of 4.1 mg/cm<sup>2</sup> and areal capacity of 2.54 mAh/cm<sup>2</sup>. The increased tap density is important for the practical application of the Si/C composite as anode for LIBs.

Except for the above structure designs, yolk-shell or core-shell structure is also attracting a lot of attention. Carbon-based or conductive polymers, which can provide good conductivity, are usually the first choice as the shell material to construct core-shell or yolk-shell structure. Core-shell structure can be introduced to improve the conductivity of the active material. At the same time, the thin conductive layer is effective to suppress the growth of thick SEI on the surface of Si. After the introduction of void space in the yolk-shell structure, it can provide sufficient space for the volume change of Si during lithiation/delithiation and provide enhanced cycling stability.

### **1.3.4 Development of advanced binder**

Various structural designs can solve the problems affecting the practical application of Si as anode for LIBs, including large volume change during cycling, poor electrical conductivity, low tap density, and some other problems. Compared with other modification methods, the development of conductive binder also provides another effective strategy to solve the problems of Si material.

The function of binder is to maintain the strong mechanical stability of all the components of the electrode. The binder is expected to be minimal swelling in the electrolyte, flexible, Li-conductive, and stable under different voltages. Currently, the widely used binder is PVDF. However, there are still some disadvantages of PVDF. The first one is the large swelling in electrolyte, which makes it lose some of its adhesion ability. Another one is the relatively weak adhesive force, due to the absence of polar functional groups, leading to only van der Waals force with other components.

Considering these two disadvantages of the PVDF, the search for a good candidate to be applied in the Si electrode becomes important. As the large volume change and poor conductivity are the two main disadvantages of Si, the advanced binders should be conductive and able to accommodate the large volume change during cycling to maintain the mechanical stability of the electrode.

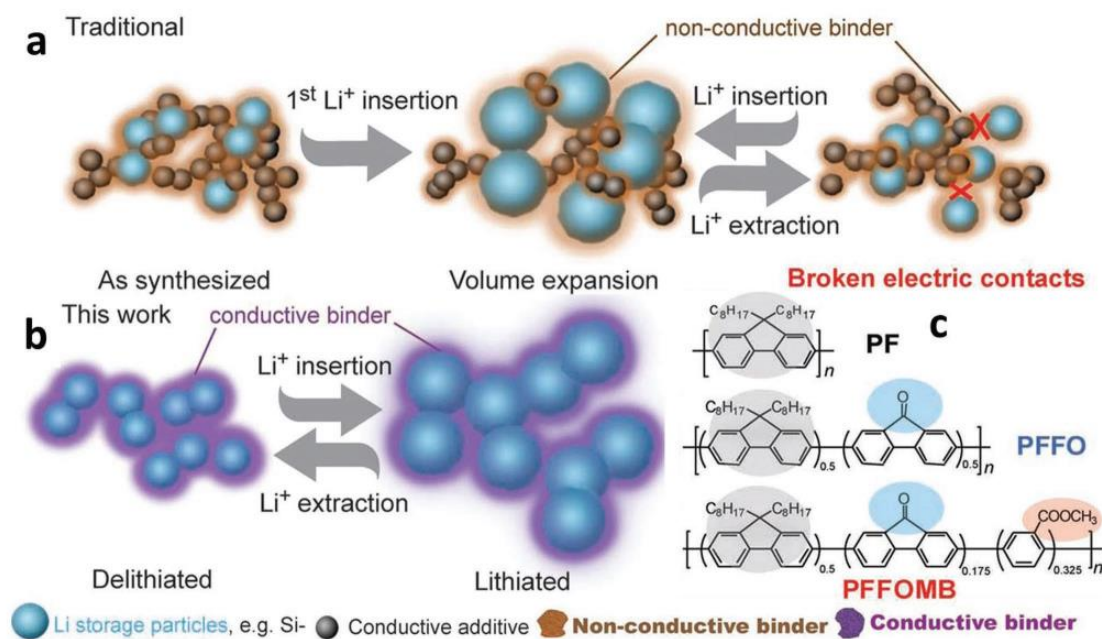


**Figure 1.15** Schematics of the technical approaches to address volume change issue in battery materials. (Copyright 2011, Wiley-VCH GmbH, Weinheim).<sup>119</sup>

Based on this designing strategy, some bifunctional polymers were developed to serve as the binder for Si based electrode (**Figure 1.15**). Except the basic function of binder, this kind of polymer is also conductive, which eliminate the using of conductive additives, benefiting the increase of energy density. Additionally, the presence of polar functional groups can form chemical bonding with the surface of Si particles to maintain the desired mechanical stability. Unlike the traditional binder, it can efficiently accommodate the large volume change during

cycling and maintain contact between the Si and the conductive binders, ensuring better cycling stability.<sup>119</sup>

Some self-healing polymers were also proved to be a promising candidate for serving as binder for Si anode material.<sup>114</sup>

## **1.4 Design of battery with improved performance by engineering electrode materials**

In this dissertation, to build LIBs with enhanced energy density, Ni-rich cathode and Si-based anode are selected as the electrodes. To overcome the above discussed challenges of Ni-rich cathode and Si-based anode, various modification strategies to cathode and anode are proposed, respectively.

### **Optimization of cathode:**

The cycling stability is the main challenges of the Ni-rich cathode material. Various factors can lead to the capacity decay of the Ni-rich cathode, including  $\text{Li}^+/\text{Ni}^{2+}$  disordering, Li residual, overcharging, poor thermal stability, *et al.* The problem can happen to both primary and secondary particles. Current, the commonly used modification methods are coating and doping, which can be applied on either primary or secondary particles. To improve the structural stability, here, we propose a novel modification strategy to simultaneously modify both the primary and secondary particles through an easy coprecipitation method.

### **Development of anode:**

For the Si-based anode, to increase the potential for practical application, micro-sized Si is selected as the main component of the Si-based composite. Through building the micro-sized Si with skeleton and protective thin skin, the Si-based composite anode material is expected to provide sufficient space to accommodate the volume change during cycling and enhanced conductivity. All these unique features contribute to the improvement of the electrochemical performance of Si-based anode material.

At the same time, a composite combined the advantages of both MXene matrix and SiGe alloy is also proposed. Under this configuration, MXene with autoadjustable layer space can provide sufficient space to accommodate the volume expansion/shrinkage upon  $\text{Li}^+$  insertion/extraction process. While SiGe alloy is also expected to show increased structural stability. With the incorporation of MXene with high conductivity and outstanding mechanical stability, the SiGe@MXene composite is proposed as anode material with improved cycling stability and rate capability.

# **CHAPTER 2 Ni-Rich Layered Transition Metal Oxide Cathode with Dual Gradient on Both Primary and Secondary Particles for High Energy-Density Lithium-Ion Batteries**

## **2.1 Introduction**

Lithium-ion batteries (LIBs) have been regarded as one of the most important energy storage devices and been attracting more and more interest during the past decades. LIBs have been widely used as the power source for portable electric devices, communication equipment, electric vehicles (EVs) and hybrid electric vehicles (HEVs).<sup>8</sup> Considering the development of technology and the current status of traditional energy resources, EVs has been thought to be the most promising transportation method for now and in future. The performance of EVs is closely related to the performance of LIBs. To meet the demand of driving range and charge frequency for EVs and HEVs, LIBs with high energy density, high rate capability, and thermal stability are required.<sup>11, 12</sup> Among the components of modern LIBs, cathode material has been regarded as one of the most important factors limiting the energy density of LIBs due to its relative low specific capacity.<sup>13, 14</sup> To reach high energy density, effort can be focus on two directions, the optimization and improvement of both the upper cutoff voltage and the specific capacity of the cathode material.<sup>7</sup> Various cathode materials have been widely and deeply investigated. Among them, Ni-rich cathode materials, including  $\text{LiNi}_{1-x-y}\text{Mn}_x\text{Co}_y\text{O}_2$  ( $x+y \leq 0.4$ ) (NMC) and  $\text{LiNi}_{0.8}\text{Co}_{0.15}\text{Al}_{0.05}\text{O}_2$  (NCA), are attracting high attention and have been widely regarded as one class of the most promising cathode material. The high capacity of above 200 mAh/g and the average high discharge

potential of 3.8 V (vs Li<sup>+</sup>/Li) provide Ni-rich cathode material high potential to largely improve the energy density and power density of LIBs.<sup>16-18</sup> However, there are still some challenges, including the poor cycling stability and rate capability, limiting the practical application of Ni-rich cathode materials need to be overcome in hurry.<sup>16, 20</sup> Based on the previous research, the main reasons resulting in the poor electrochemical performance can be summarized as the Li<sup>+</sup>/Ni<sup>2+</sup> cation mixing, Li residues on the surface, poor thermal stability, crystal structure and some other factors.<sup>30</sup>

Various methods or approaches have been applied on the modification of Ni-rich cathode material, as discussed in **Chapter 1**. Compared with other modification methods, the construction of transition metal concentration gradient provided a new idea for the designing of Ni-rich cathode materials to improve the structural stability and electrochemical performance.<sup>73</sup> The concentration gradient can be created through various methods, for example, controlling the gradual change of the pH value in the synthesis of precursor,<sup>68</sup> and gradually changing the transition metal ions ratio of the solution during coprecipitation.<sup>73</sup> All these methods have been proved to be effective to improve the structural stability of cathode material during cycling. Through introducing the sacrificial polymeric (polystyrene) beads the coprecipitation process to serve as the core of the Ni-rich NMC precursor, a cation mixing layer can be created on the surface of the secondary particles. The self-induced cation mixing layer with rock-salt structure on the surface of primary particles displayed significant influence on improving the structural stability during lithiation/delithiation by suppressing the phase transition from the original layered structure.<sup>69</sup>

As we know, to increase the tap density, most of the Ni-rich NMC cathode materials are composed of microsized secondary particles, which are formed by densely packed nanosized primary

particles.<sup>67</sup> The capacity decay of Ni-rich cathode during cycling can be caused by various factors. The accumulation of strain within primary particles would cause the pulverization of secondary particles. At the same time, the penetrating electrolyte through grain boundaries can build thick solid-electrolyte interphase layer on the surface of the primary particles, which can inhibit the transport of electrons and lithium ions. However, after literature review, it can be found that most of the reported approaches were applied only on primary or secondary particles. For example, coating is mainly applied on the surface of secondary particles, which is not effective to eliminate the volume change of primary particles and suppress the formation of strain of primary particles during cycling. Doping can modify the component of primary particles but protecting the secondary particles from the side reaction with electrolyte. All these can lead to the performance decay for Ni-rich NMC cathode materials during cycling. Applying effective protection on both primary and secondary particles provides a promising design strategy for Ni-rich NMC cathode materials with high performance.<sup>67</sup>

## 2.2 Design strategies and preparation of D-NMC811

### 2.2.1 Synthesis of D-NMC811

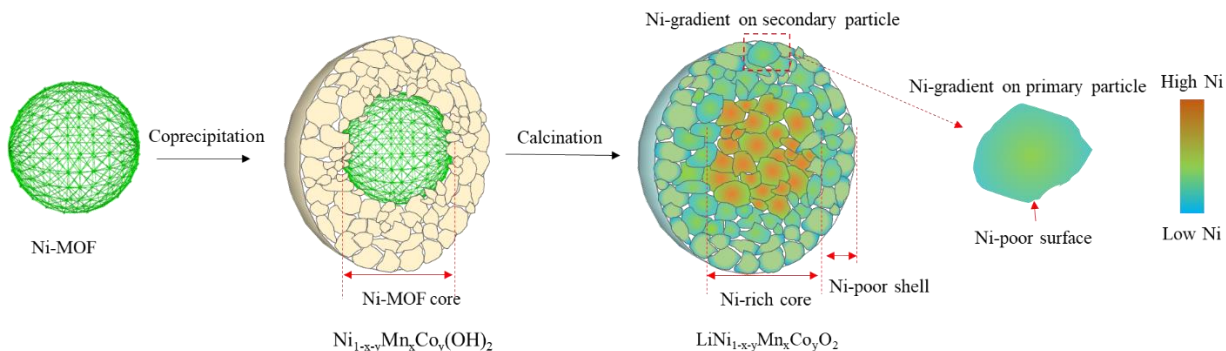


**Figure 2.1** Design of MOF modulated double-Ni-gradient NMC811. Synthesis process of the D-NMC811.

Herein, we propose a novel approach by simultaneously building dual Ni concentration gradient on both primary and secondary particles of Ni-rich NMC cathode material through introducing Ni-MOFs during the coprecipitation of the NMC precursor. The sample is denoted as D-NMC811. The synthesis route is shown in **Figure 2.1**. Basically, without changing the conventional coprecipitation method to obtain the precursor, Ni-MOFs are introduced into the synthesis of Ni-rich cathode material.

As we know, the highly ordered three-dimensional MOFs with ultrahigh surface area, controllable porous structure and periodic arrangement of metal atoms have been demonstrated as novel pyrolytic precursors in obtaining non-precious metal oxides with homogeneous distribution of particles.<sup>120</sup> MOF-derived metal oxides have been widely used for supercapacitor electrode materials. In the area of LIBs, Li *et al.* developed a thin protective layer of MOF-derived alumina on the surface of NMC622 through calcinating Al-based MOF (NH<sub>2</sub>-MIL-53) coated NMC

precursor.<sup>121</sup> And MOFs were also successfully used to modify the surface of Li-rich layered oxide cathode.<sup>122</sup> Here a different route is applied. Briefly, the precursor was synthesized through the coprecipitation method. Ni-MOFs were uniformly dispersed in the metal sulfate solution and pumped into the reactor. During the coprecipitation of the precursor, the well-dispersed Ni-MOFs act as reaction seeds for the growth of metal hydroxide particles. The huge specific surface area provides numerous active sites for the growth of metal hydroxide primary particles around the Ni-MOFs. The precursor,  $\text{Ni}_{1-x-y}\text{Mn}_x\text{Co}_y(\text{OH})_2$ , prepared through coprecipitation was incorporated with Ni-MOFs as core of the secondary particles (**Figure 2.1**). After uniformly mixing with lithium source (LiOH), the obtained precursors were subjected to calcination process under pure oxygen flow. During the high temperature calcination, the Ni-MOFs were carbonized and decomposed by oxidation and reacted with transition metals on the surface of the primary particles. Transition metal concentration gradient with reduced Ni oxidation state were formed in the primary particles due to the movement of transition metal ions motivated by the electric compensation of charge change.<sup>123</sup> At the same time, due to the presence of metallic components from Ni-MOFs in the core, Ni concentration gradient also formed in secondary particles.

### **2.2.2 Working mechanism of Ni-MOFs**

The prepared NMC811 through cooperation with D-NMC811 retains self-induced Ni concentration gradient on both primary and secondary particles. The concentration gradient and self-induced cation mixing layer on the surface of primary particles effectively improved the structural stability during cycling by inhibiting the generation of internal cracks through resisting the internal strain and suppressing phase transition within primary particles during cycling process. At the same time, the high Ni content of the bulk materials ensures high specific capacity, while

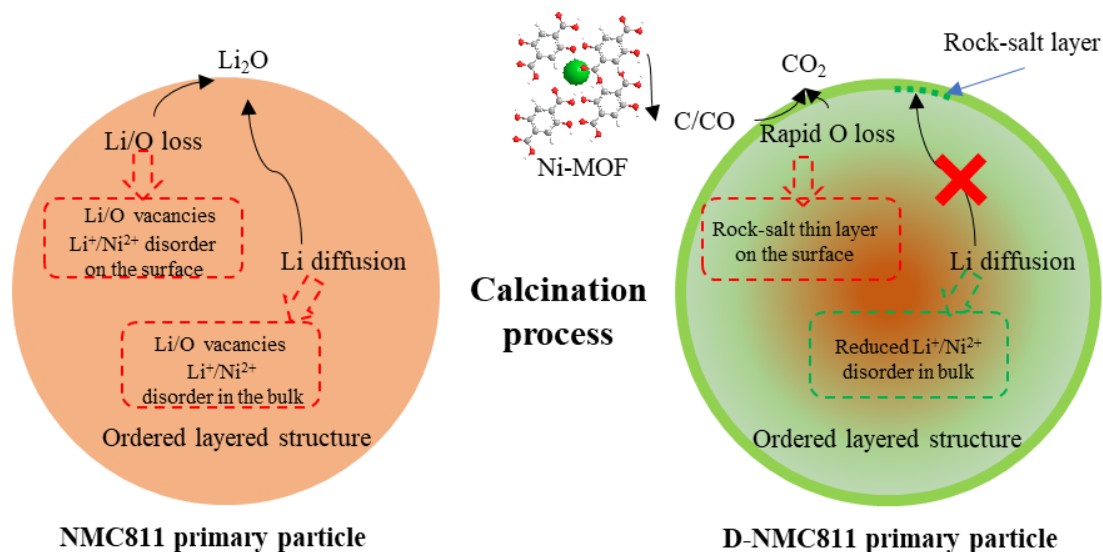


**Figure 2.2** Schematic illustration of how cationic disordering is suppressed through surface reconstruction by the presence of Ni-MOF in D-NMC811 during calcination.

low Ni content in the outer layer further improved the stability of the obtained cathode material. This approach leads to significantly improved cycling stability.

**Figure 2.2** illustrates how the cationic disordering ( $\text{Li}^+/\text{Ni}^{2+}$ ) is suppressed through surface reconstruction by the presence of Ni-MOF in the calcination process of D-NMC811. It is well known that MOFs have been widely used to produce metal/carbon composite through carbonization at relative high temperature in inert gas.<sup>124</sup> During the calcination process, as Ni-MOFs are presented as the core of the precursor, which are closely covered by the transition metal hydroxide, the Ni-MOFs core cannot get sufficient oxygen from the outside calcination atmosphere. When the temperature is high enough, the produced carbon or carbon oxide from the decomposition and carbonization of Ni-MOFs will extract oxygen from the surface of primary particles. The resulted rapid oxygen loss on the surface of the primary particles produces a large number of oxygen vacancies on the surface, leading to the phase transformation from layered phase

to disordered rock-salt phase. Compared with layered structure, rock-salt phase is oxygen-deficient and thermodynamically more stable, which is not easy to lose extra oxygen and is able to prevent further oxygen loss through blocking the outward diffusion pathway from the bulk to the surface. As a result, the  $\text{Li}^+/\text{Ni}^{2+}$  disordering can be effectively suppressed in the bulk.<sup>125</sup> For contrast, without the protection of the rock-salt passivation layer, continuous Li/O loss produce lithium vacancies on the surface, leading to the diffusion of lithium from the bulk to the surface and formation of  $\text{Li}^+/\text{Ni}^{2+}$  disordering in the bulk.

## 2.3 Characterization of D-NMC811

### 2.3.1 Characterization of Ni-MOFs

Before reaction, the Ni-MOFs were prepared through a hydrothermal method. Various characterizations were applied to analyze the property of the obtained Ni-MOFs. **Figure 2.3** shows the morphology of the obtained Ni-MOFs. It can be found that, after drying, Ni-MOF particles with diameter of  $\sim 1.3 \mu\text{m}$  were uniformly dispersed into the coprecipitation solution containing transition metals ions.

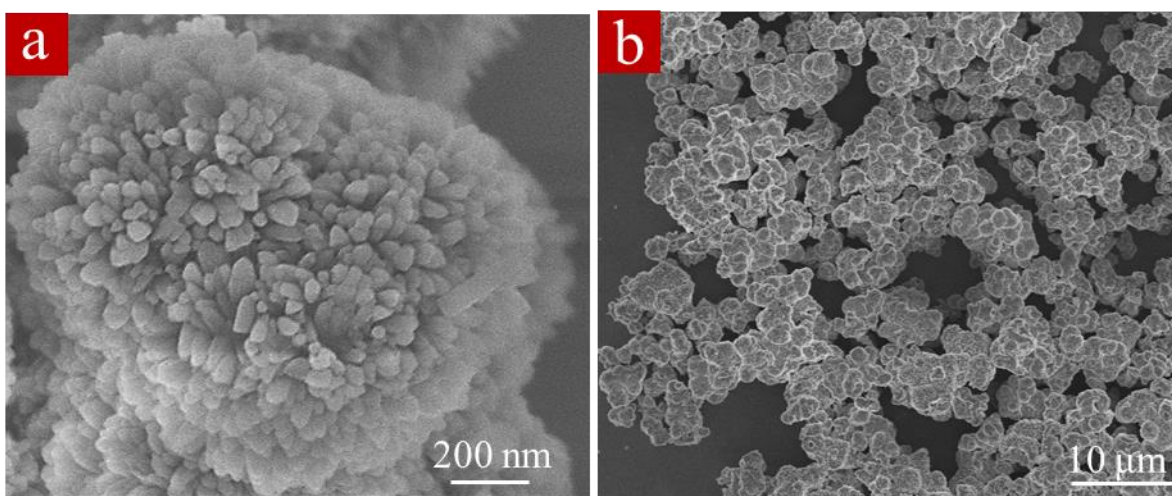


**Figure 2.3** SEM morphologies of the Ni-MOF precursor under different magnification.

The specific surface area was also measured through  $\text{N}_2$  sorption-desorption isotherms, as shown in **Figure 2.4 a, b**. The specific surface area of the obtain Ni-MOF was determined to be  $933.7 \text{ m}^2/\text{g}$  with pore volume of  $0.519 \text{ cm}^3/\text{g}$  and pore size of 10-60 nm through Brunauer-Emmett-Teller (BET) method. The high specific surface area provides numerous sites for the growth of the transition metal precursor.

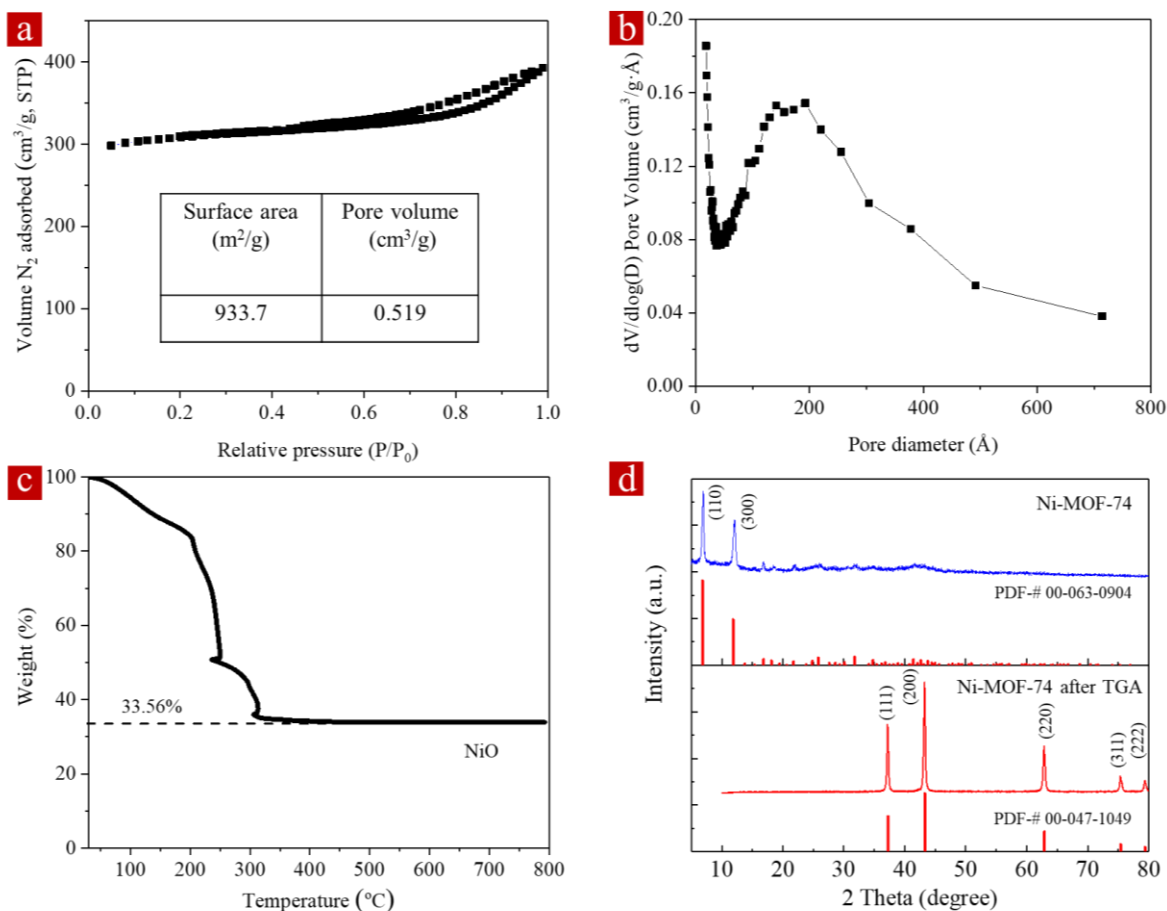


**Figure 2.4** Surface and TGA analysis of the Ni-MOF. Nitrogen sorption-desorption isotherms (a) and the pore size distribution (b). (c) TGA data at a rate of 5 °C/min under an air flow of 50 ml/min. (d) XRD patterns of Ni-MOF before and after TGA.

To accurately control the transition metal ions ratio, the Ni content in the obtained Ni-MOFs needs to be determined. Thermogravimetric analysis (TGA) was operated with a heating rate of 5 °C/min under an air flow of 50 ml/min. As shown in **Figure 2.4 c**, after heating to 800 °C, the weight of the residual is 33.56% of the original mass. X-ray diffraction (XRD) was then applied to determine the composition and structure of the residual. As shown in **Figure 2.4 d**, the residual is determined to be NiO (PDF # 00-047-1049). The crystal structure of the obtained Ni-MOF was

also confirmed to be Ni-MOF-74 (PDF # 00-063-0904). Combine with the TGA result, the Ni content was determined to be 26.4%. The content of Ni in Ni-MOF was calculated as: (mass ratio of the final produced NiO) \* (Mw of Ni / Mw of NiO) = 33.56% \* 58.693 / 74.693 = 26.4%. At the same time, the crystal structure of the obtained Ni-MOF was also confirmed to be Ni-MOF-74 (PDF # 00-063-0904).

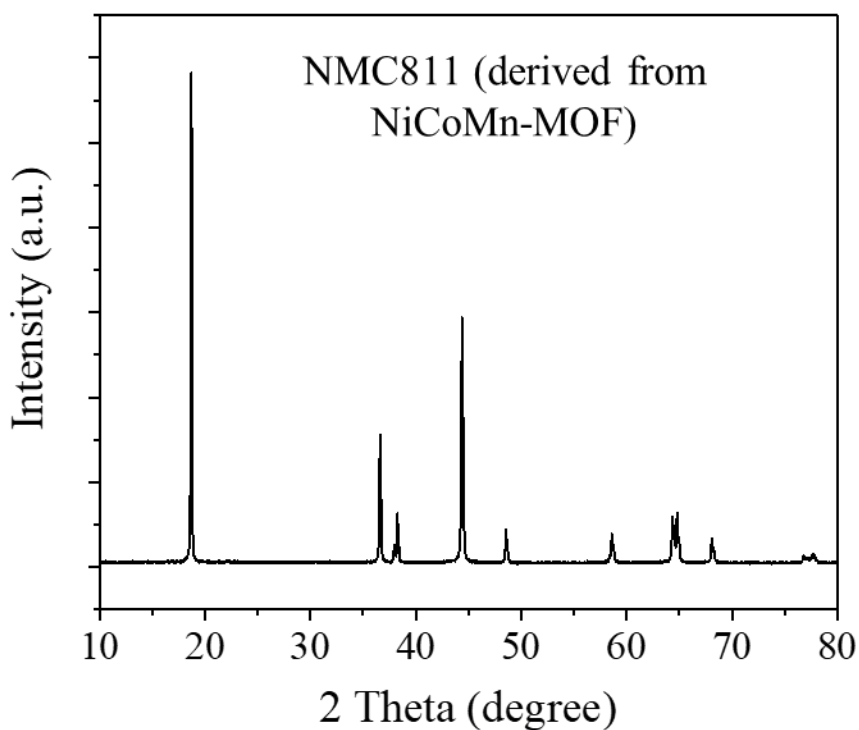


**Figure 2.5** XRD pattern of the NMC811 obtained directly from the NiCoMn-MOF.

As the Ni-MOFs are shown as the core of the transition metal precursor, it is necessary to confirm that Ni-MOFs can form layered structure during the same calcination as the transition metal precursor. MOFs containing Ni, Co, and Mn with corresponding ratio of 8:1:1 was prepared through same method as Ni-MOFs (denoted as NiCoMn-MOFs). Then, same calcination process

was applied to the obtained NiCoMn-MOFs to figure out the possibility to produce NMC811. As shown in **Figure 2.6**, the layered structure of the NMC811 directly derived from MOFs was confirmed by XRD. However, the electrochemical performance of the obtained NMC was not good, which may result from the inaccurate control of the transition metal ions ratio, particle structure and morphology (**Figure 2.7**).<sup>126</sup>

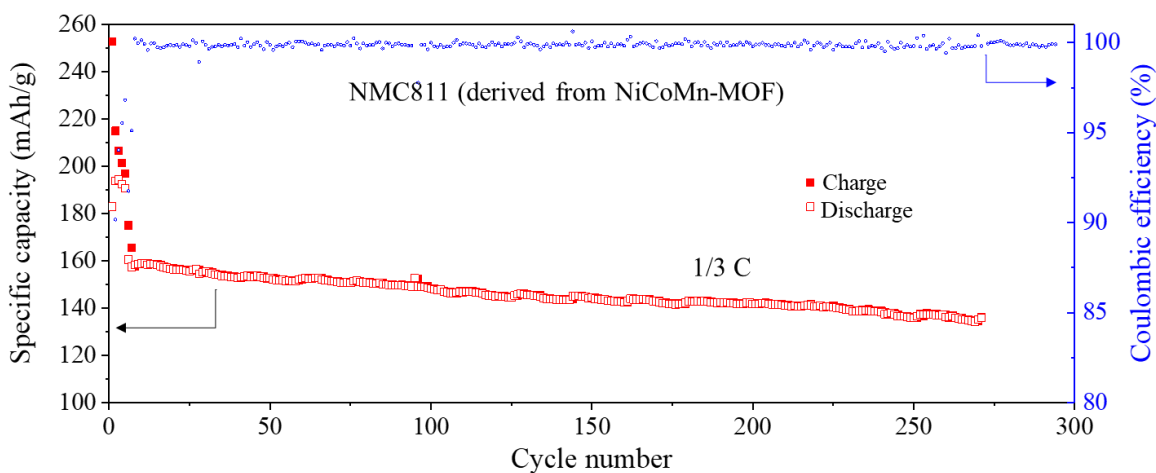


**Figure 2.6** Cycling performance of the NMC811 obtained directly from the NiCoMn-MOF.

## 2.3.2 Morphology and crystal structure

### 2.3.2.1 Morphology

The morphology of the obtained NMC particles is also important for practical application. To improve the tap density, the favorable packing status of NMC particles is secondary particle formed by closely packed primary particles. Scanning electron microscopy (SEM) was applied to check the morphology of the obtained D-NMC811 and regular NMC81, as shown **Figure 2.7**. From the SEM images, it is clear that the diameter of the secondary particles of the two samples are about 4.0  $\mu\text{m}$ , which are composed of closely packed primary particles with diameter of several

hundred nanometers. The formed packing status of the obtained NMC particles is beneficial to improve the tap density of NMC cathode materials, which is important for the practical application.

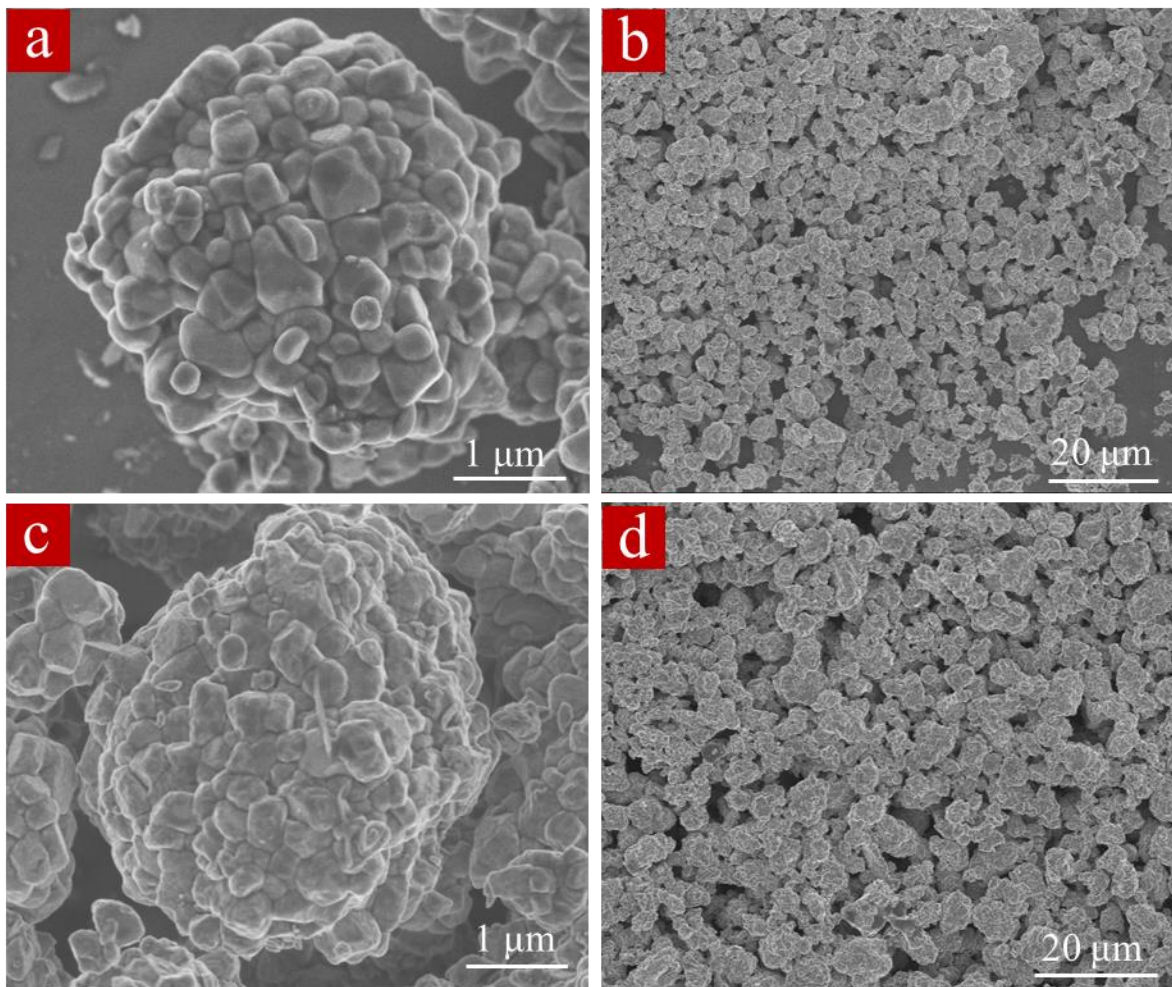


**Figure 2.7** SEM morphologies of (a-b) the D-NMC811, and (c-d) the conventional NMC811.

At the same time, BET was applied to measure the specific surface area and pore size of the obtained NMC samples, as shown in **Figure 2.8**. It can be found that the specific surface area of NMC811 and D-NMC811 are 0.4943 and 0.5206 m<sup>2</sup>/g, respectively. The slightly increased specific surface area may result from the possible pores after the decomposition of Ni-MOFs.

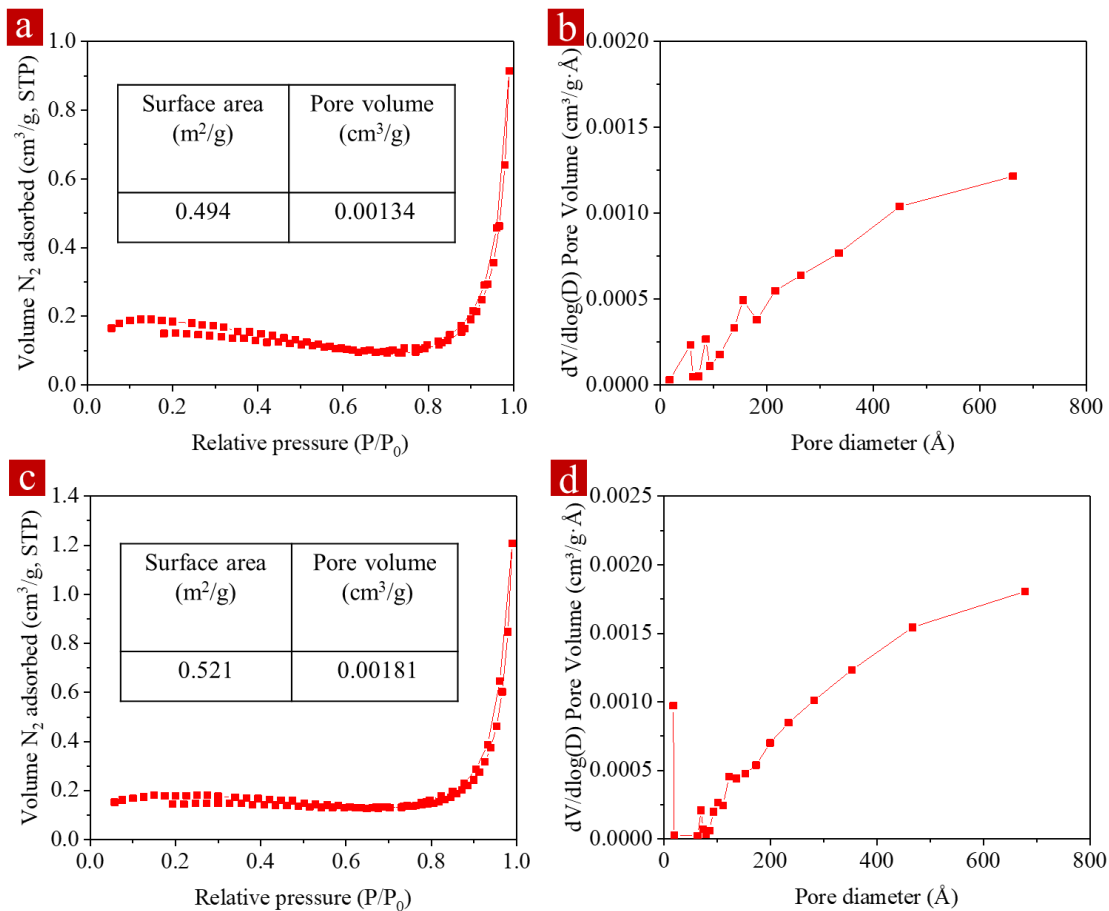


**Figure 2.8** Surface analysis of the D-NMC811 and conventional NMC811. Nitrogen sorption-desorption isotherms and pore size distribution of the conventional NMC811 (a, b) and the D-NMC811 (c, d).

### 2.3.2.2 Crystal structure

X-ray diffraction (XRD) was used to measure the crystal structure of the two obtained NMC samples, NMC811 and D-NMC811.<sup>127</sup> To reveal the structure details, Rietveld refinement was applied. The fitting results were shown in **Table 1**. The XRD patterns and corresponding fitting results from the refinement were plotted in **Figure 2.9**. First, clear splits between the (006)/(102) and (108)/(110) are found on the XRD patterns of the two samples (inserted), indicating well-

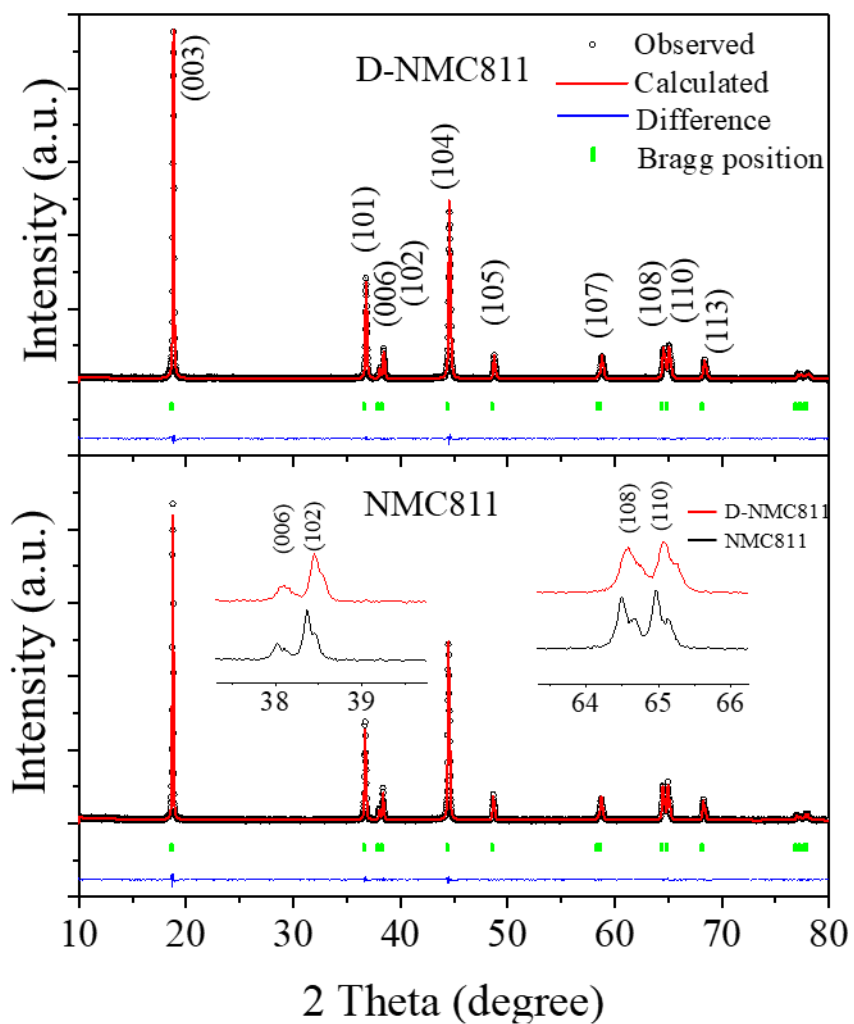


**Figure 2.9** XRD patterns and refinement results of the D-NMC811 and the conventional NMC811.

defined highly crystalline layer structure. The  $\text{Li}^+/\text{Ni}^{2+}$  disordering of the samples can be reflected by the ratio of  $I(003)/I(104)$  from the XRD refinement results. From the refinement results, it can be found that the intensity ratio of  $I(003)/I(104)$  of D-NMC811 increases from 1.082 to 1.244, which indicates that the degree of cation mixing was reduced from 3.4 to 1.70%. It is also proved by the increased ratio of parameters  $c/a$  of D-NMC811. The detailed suppressing mechanism has been explained in **section 2.2.2**. The  $\text{Li}^+/\text{Ni}^{2+}$  disordering has been proved to be a key factor affecting the initial capacity loss and cycling performance. The reduced  $\text{Li}^+/\text{Ni}^{2+}$  is usually favorable for Li ion diffusion and the rate capability.<sup>128</sup>

**Table 2-1** Lattice parameters, ratio of  $I(003)/I(104)$  and  $\text{Li}^+/\text{Ni}^{2+}$  mixing derived from the Rietveld refinement of the D-NMC811 and conventional NMC811

Samples	$a$ (Å)	$c$ (Å)	$V$ (Å <sup>3</sup> )	$z_{ox}$	$I(003)/I(104)$	$\text{Li}^+/\text{Ni}^{2+}$ mixing (%)
NMC811	2.87096	14.20333	101.385	0.24779	1.082	3.40
D-NMC811	2.86691	14.19543	101.043	0.24744	1.244	1.70

### 2.3.2 Confirmation of the gradient on both primary and secondary particles.

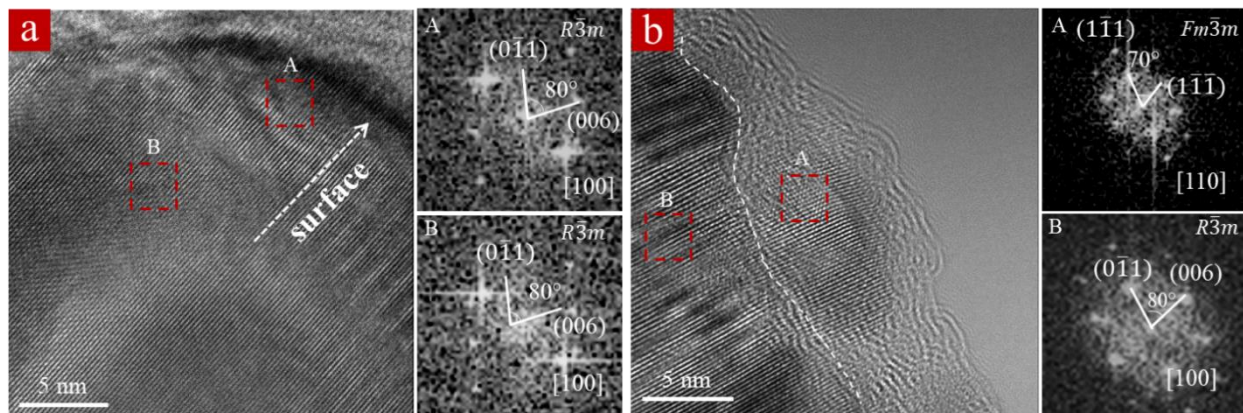


**Figure 2.10** Phase structure and chemical composition diagnosis of primary and secondary particles. High-resolution TEM along with the corresponding FFT analysis of the primary particle with (a) conventional NMC811 and (b) D-NMC811, respectively. The A region corresponds to the surface area while B is located at the core area.

As discussed in the designing strategy, a thin cation mixing layer with rock-salt structure is supposed to form on the surface of the primary particles of D-NMC811 during the calcination process, due to the presence of Ni-MOFs. To confirm the presence of the cation mixing layer, high resolution transition electron microscopy (HRTEM) with fast Fourier transform (FFT) patterns were applied on the edge of the primary particles, as shown in **Figure 2.10**. From the HRTEM images with FFT patterns of the primary particles of NMC811 and D-NMC811, it can be found that a thin cation mixing layer with thickness of 5-10 nm was shown on the surface of D-NMC811. While, different with that of D-NMC811, continuous layered phase is found from the core to the surface from the obtained FFT patterns (**Figure 2.10 a**).

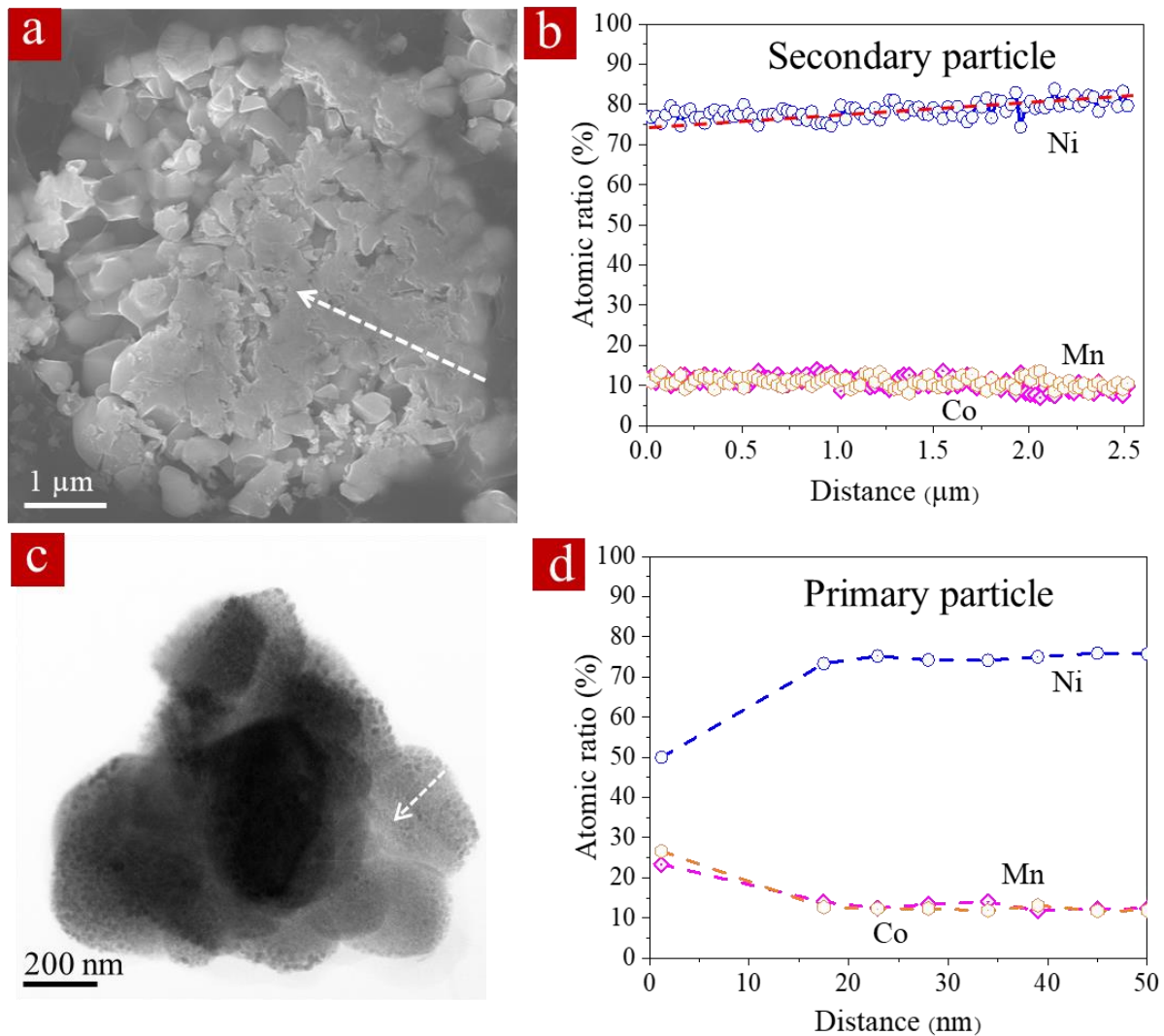


**Figure 2.11** Cross-section view (a) and the corresponding Ni, Mn, Co concentration evolution from the surface to core (b) of a secondary particle of D-NMC811. TEM morphology (c) and concentration evolution from the surface to core (d) of a primary particle of D-NMC811.

To further confirm the presence of concentration gradient on both primary and secondary particles, TEM and SEM with energy dispersive X-ray spectroscopy (EDS) were applied on the obtained D-NMC811 sample. The results are shown in **Figure 2.11**. First, as shown in **Figure 2.11 a**, the cross-sectional SEM image of the secondary particle of D-NMC811 is selected to measure the

concentration gradient following the arrow from surface to core. It can be found that the atomic ratio of Ni increases from ~76% to 82% in a length about 2.5  $\mu\text{m}$  (**Figure 2.11 b**). This can be attributed to the presence of metallic components from Ni-MOF in the core of precursor. During the calcination process, the metallic component, Ni, is left and involved in the formation of NMC. **Figure 2.11 c and d** show the TEM image of a primary particle with corresponding EDS line scan, which shows that reduced Ni concentration from the surface to the core. The atomic Ni ratio is determined to be ~50% on the surface of primary particles, instead of ~75% in the bulk.

### 2.3.3 Confirmation of the oxidation state change

Scanning transmission electron microscopy (STEM) and electron energy-loss spectroscopy (EELS) were applied at the surface of primary particles of D-NMC811 to analyze the chemical and electronic structures. The EELS depth profiles of Mn, Co, and Ni from the surface layer with a depth of  $\sim 35$  nm are shown in **Figure 2.12 a-d**. It can be found that the intensity ratio of  $L_3/L_2$  at

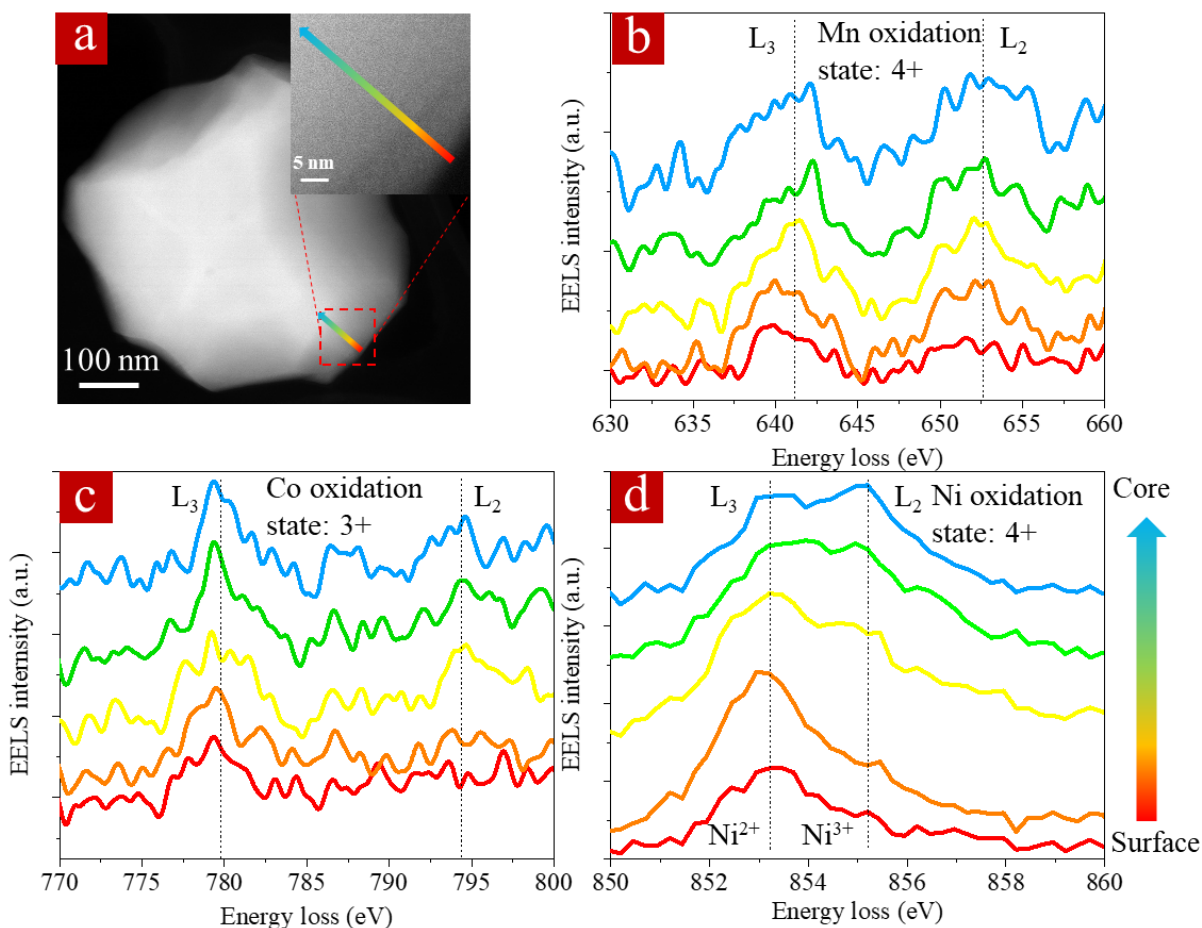


**Figure 2.12** STEM image (a) of a primary particle of D-NMC811 with corresponding EELS spectra of Mn (b), Co (c), and Ni (d) L-edges.

Mn-L edge and Co-L edge, which is correlated with the valence state of transition metals, is not changed (**Figure 2.12 b and c**), indicating constant valence state of manganese and cobalt from

the surface to the core.<sup>129</sup> Basically the oxidation state decreased as increasing of the integrated intensities ratio of  $L_3/L_2$ .<sup>130</sup> Obvious change of the  $L_3/L_2$  is found on the Ni-L edge, as shown in **Figure 2.12 d**. With the depth increase from the surface to the core, the peak of trivalent nickel is increased, and the intensity ratio of  $L_3/L_2$  is decreased, indicating the increased oxidation state from divalent nickel on the surface to trivalent nickel in the core. During the calcination process at high temperature, the organic component of Ni-MOFs is decomposed and carbonized by the oxidization and produce  $CO_2$ . The produced  $CO_2$  is able to diffuse out through the grain boundaries, which has been proved to be able to extract oxygen and create oxygen vacancies on the surface of primary particles.<sup>131</sup> At the same time, the most unstable trivalent  $Ni^{3+}$  ions are gradually reduced to divalent  $Ni^{2+}$  ions on the surface, resulting the gradual change of oxidation state of Ni from the surface to the core of the primary particles. The oxidation state change of Ni ions provides driving force for the movement of transition metal ions to balance the electron neutrality, resulting the concentration gradient. During calcination process, the produced  $Ni^{2+}$  on the surface can move from the transition metal site to the Li site and form a thin layer of cation mixing region due to similar ionic radius only on primary particles (**Figure 2.10 b**). The self-induced cation mixing layer could significantly inhibit the volume change of grains due to the pillar effect and promote high stability during cycling, which will be further evaluated in the following **section 2.6**.<sup>132</sup> Furthermore, the transition metal concentration gradient on secondary particles also bring benefit to the electrochemical performance. The high Ni content of the bulk material ensures the high capacity of D-NMC811 with further improved stability attributed to the presence of low Ni content in the outer layer.<sup>73, 133</sup>

### 2.3.4 X-ray photoelectron spectroscopy characterization

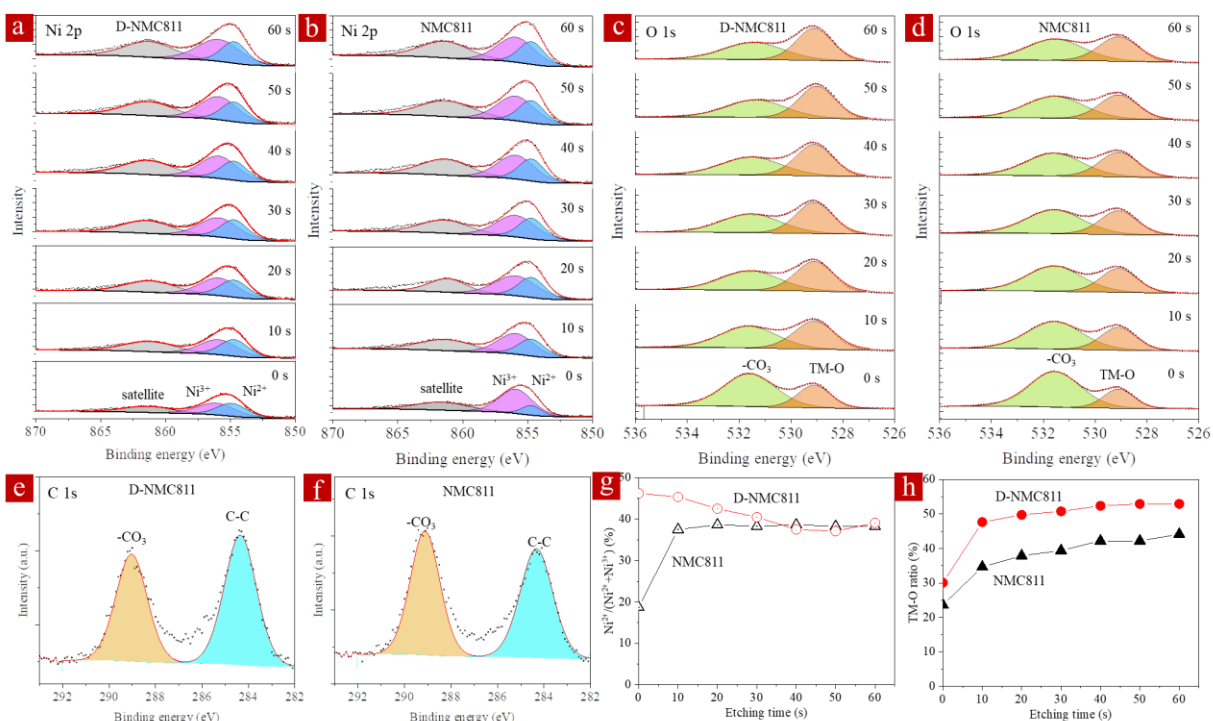


**Figure 2.13** XPS spectra analysis of the D-NMC811 and conventional NMC811. Depth profiles of Ni 2p (a-b), O 1s (c-d), and XPS spectra of C 1s (e-f), respectively. The ratio evolution of Ni to Ni<sup>2+</sup>/Ni<sup>3+</sup> (g) and lattice oxygen (TM-O) (h) with increasing etching time obtained from the depth profiles.

X-ray photoelectron spectroscopy (XPS) was used to further confirm the structure information and surface properties. As shown in **Figure 2.13**, XPS spectra depth profiles of Ni, O, and spectra of C on the surface were obtained for NMC811 and D-NMC811, respectively. **Figure 2.13 a-d** show the XPS spectra depth profiles and fitting results of Ni 2p and O1s of the obtained two samples, respectively. The Ni 2p<sub>3/2</sub> can split into two peaks at 855.8 eV and 853.9 eV, indicating the existence of Ni<sup>3+</sup> and Ni<sup>2+</sup>, respectively. The oxidation state of Ni ions can be determined by the value of Ni<sup>2+</sup>/(Ni<sup>2+</sup> + Ni<sup>3+</sup>), which was calculated based on the fitting results and shown in **Figure 2.13 g**. It can be found that divalent Ni<sup>2+</sup> ion ratio for NMC811 and D-NMC811 before etching are

18.70% and 46.24%, respectively. After etching, from 10 s to 60 s, the divalent  $\text{Ni}^{2+}$  ion ratio for NMC811 keeps constant at ~38.27%. But the  $\text{Ni}^{2+}$  ion ratio for D-NMC811 decreases from 46.24% to 37.11%, indicating the gradual change of oxidation state of Ni from the surface to the core. The increased  $\text{Ni}^{2+}$  ratio also matches well with the EELS results (as shown in **Figure 2.12 d**) and provides further confirmation of the presence of self-induced cation mixing layer on the surface of D-NMC811 as obtained from the TEM images and FFT patterns (**Figure 2.10 b**). The formation of Li residues, like LiOH and  $\text{Li}_2\text{CO}_3$ , can lead to the decomposition reaction with electrolytes and gas generation, resulting deterioration of the battery performance.<sup>134</sup> The XPS spectra of O1s and C1s (**Figure 2.13 c-f**) were also used to analyze the formation of carbonate on the surface. As shown in **Figure 2.13 h**, on the original surface (without etching), the relative intensity ratio of the peak at ~529 eV representing lattice oxygen covalency (TM-O) of D-NMC811 is ~30.1%, which is higher than that of regular NMC811 (23.7%). Also, the relative intensity ratio of TM-O significantly increased to 47.6% after etching of 10 s with corresponding etching depth of ~2.4 nm, indicating the formation of much thinner layer of  $\text{Li}_2\text{CO}_3$  on the surface of D-NMC811. However, the peak of NMC811 still shows relative low TM-O intensity ratio of 44.1% even after etching of 60 s, as an evidence of the presence of  $\text{Li}_2\text{CO}_3$  with large thickness. The amount difference of the formed  $\text{Li}_2\text{CO}_3$  on the surface is further confirmed by the different intensity ratio of  $-\text{CO}_3$  on the XPS spectra of C1s and O1s, as shown in **Figure 2.13 c-f**.

## 2.4 Electrochemical performance

### 2.4.1 CV

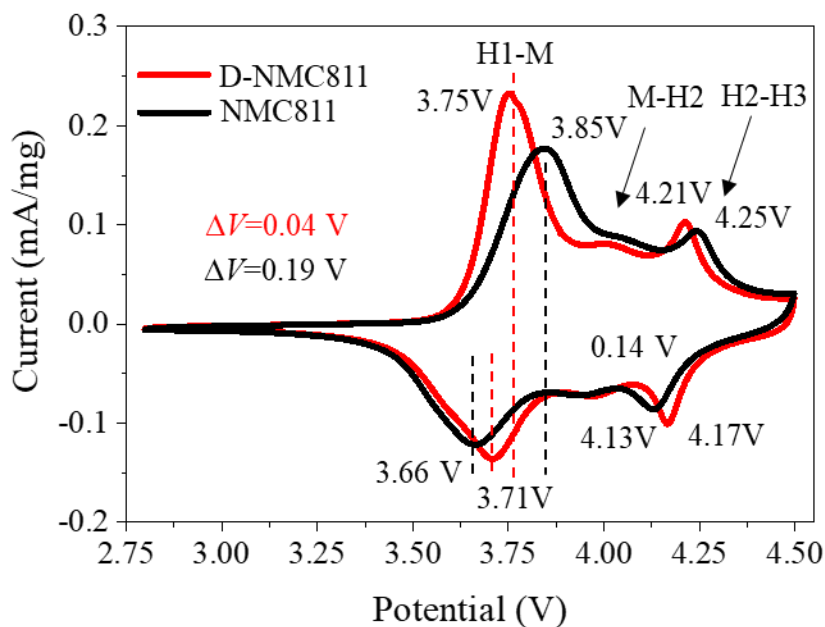


**Figure 2.14** Cyclic voltammetry of D-NMC811 and NMC811 at a scanning rate of 0.1 mV/s.

Cyclic voltammetry (CV) was measured at a scanning rate of 0.1 mV/s, which is believed to be able to reflect the electrochemical kinetic properties. As shown in **Figure 2.14**, the redox peaks are much sharper for D-NMC811 compared with NMC811, indicating enhanced  $\text{Li}^+$  diffusion behavior.<sup>68</sup> At the same time, the gap between all redox couples for NMC811 is wider than D-NMC811. The voltage difference between anodic and cathodic peaks are 0.04 V and 0.19 V for D-NMC811 and NMC811. The voltage between anodic and cathodic peaks is associated with the redox reactions involving  $\text{Ni}^{2+}$ ,  $\text{Ni}^{3+}$ , and  $\text{Ni}^{4+}$ , where smaller value reflects the superior reversibility of D-NMC811.<sup>68, 135</sup>

## 2.4.2 Battery performance

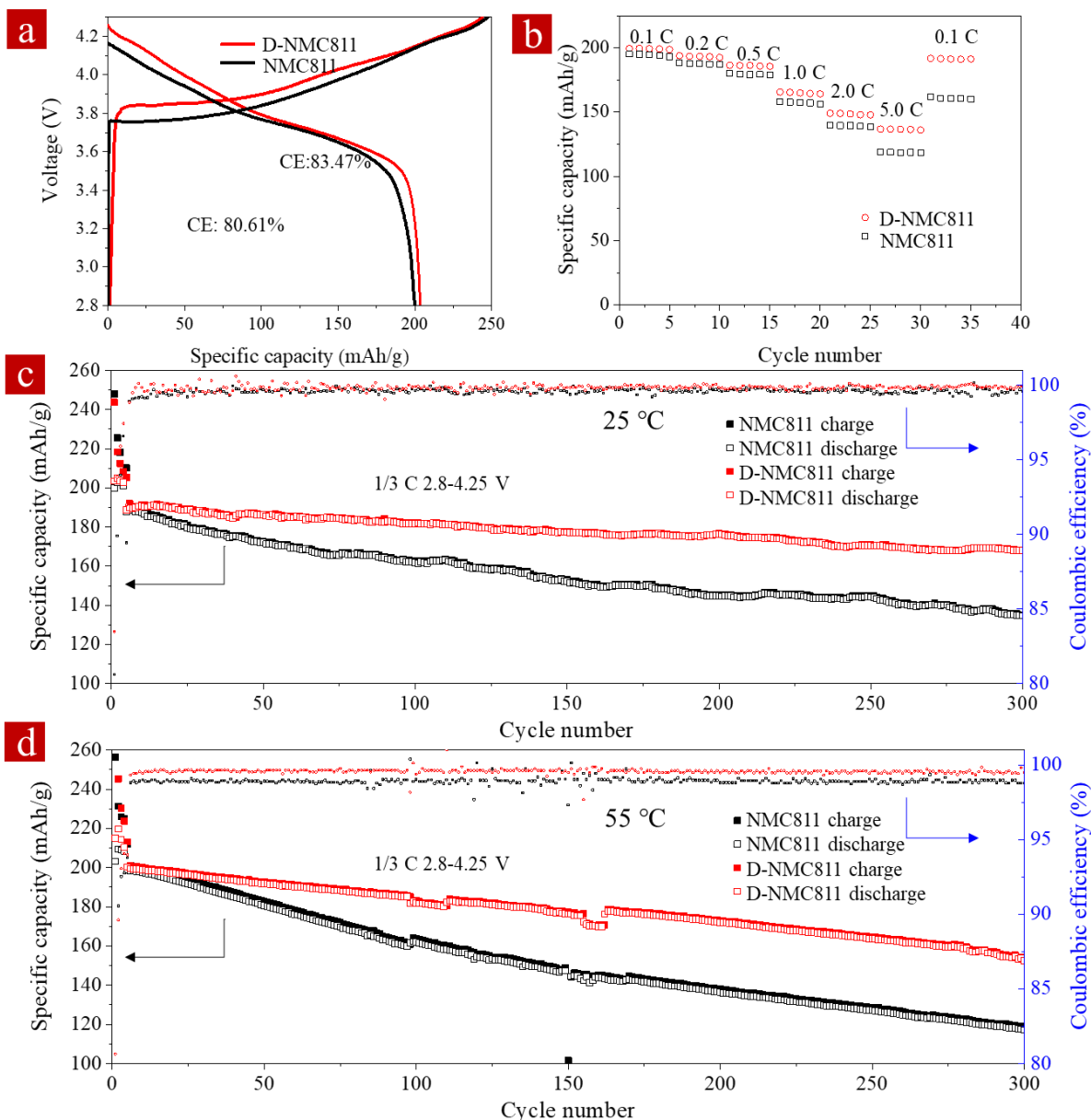


**Figure 2.15** (a) Charge/discharge voltage profile of the first cycle at 0.1 C (2.8-4.3 V, 1 C=180 mAh/g). (b) Specific charge/discharge capacity evolution of D-NMC811 and NMC811 at different rates from 0.1 C to 5.0 C (before test, the batteries were charged/discharged at 0.1 C between 2.8 to 4.3 V for 4 cycles for activation). Battery cycling performance (c,d) of D-NMC811 and NMC811 at 1/3 C at the temperature of 25 °C and 55 °C, respectively. The loading was controlled to be 5-6 mg/cm<sup>2</sup>. The interrupted data were originated from the temperature perturbation upon operation.

The galvanostatic charge/discharge curves of NMC811 and D-NMC811 are shown in **Figure 2.15 a**. At 0.1 C, the NMC811 and D-NMC811 deliver initial specific discharge capacity of 199.88 mAh/g and 203.47 mAh/g with CE of 80.61% and 83.47%, respectively. **Figure 2.15 b** shows the rate performance of NMC811 and D-NMC811 from 0.1 C to 5.0 C. It can be found that the rate performance of D-NMC811 is significantly improved compared with the NMC811 especially at high rate. For example, the D-NMC811 exhibits specific discharge capacity of 165.64, 149.17, and 136.71 mAh/g at current density of 1.0 C, 2.0 C, and 5.0 C, respectively. For comparison, NMC811 only delivers specific discharge capacity of 158.28, 139.64, and 119.12 mAh/g under the same current densities. The enhanced rate performance can be attributed to the better Li<sup>+</sup> diffusion kinetics as shown in the CV curve (**Figure 2.14**).<sup>68</sup> After cycled at each rate for 5 cycles, when the current density is changed back to 0.1 C, the discharge capacity of NMC811 returns to 160.09 mAh/g. However, D-NMC811 is still able to deliver a specific discharge capacity of 191.38 mAh/g when the current density returns to 0.1 C, which is much higher than that of the regular NMC811, indicating high cycling stability.

The galvanostatic charge/discharge cycling test is performed at 1/3 C at 25 °C and 55 °C, and 1.0 C at 25 °C, respectively. At 25 °C, the initial specific discharge capacity of NMC811 is 188.0 mAh/g, and it maintains capacity retention of 86.14%, 77.02%, and 71.60%, after 100, 200, and 300 cycles at 1/3 C, respectively (**Figure 2.15 c**). In contrast, D-NMC811 shows enhanced cycling stability. Though similar initial specific discharge capacity of 188.8 mAh/g is reached by D-NMC811, it delivers higher specific capacity of 181.8, 176.3, and 167.1 mAh/g after 100, 200, and 300 cycles at 1/3 C, respectively, and maintains 96.27%, 93.38%, and 88.50% of its initial capacity after the corresponding cycles. The capacity fading rate is only 0.038% decay per cycle. At 1.0 C, NMC811 shows specific discharge capacity of 106.23 mAh/g with CE of 99.62% after 300 cycles

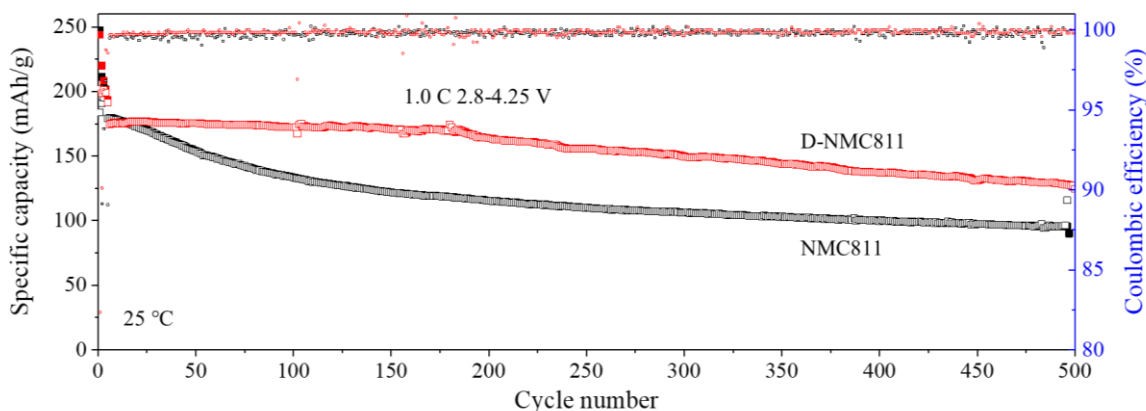


**Figure 2.16** Cycling performance of half-cell batteries with the D-NMC811 and conventional NMC811 as cathode electrode materials at 1.0 C and 25°C, respectively. Before cycling at 1.0 C, the batteries were charged/discharged three times at 0.1 C for activation. The mass loading of D-NMC811 and NMC811 is 5-6 mg/cm<sup>2</sup>.

(Figure 2.16). It maintains 59.37% of its initial capacity. The specific discharge capacity of D-NMC811 is 149.38 mAh/g after cycling at 1 C for 300 cycles. The capacity retention is largely increased to 85.54% compared with regular NMC811. To further evaluate the cycling stability of the obtained samples, the coin cells assembled with NMC811 and D-NMC811 were tested at 55 °C (Figure 2.15d). Compared with room temperature, cycling at elevated temperature is more likely to accelerate the structural degradation due to the release of molecular oxygen from the NMC lattice and make the cells exhibit worse cycling stability.<sup>33, 136</sup> The specific capacity of D-NMC811 drops from 200.27 mAh/g to 152.51 mAh/g with CE of 99.47% at 1/3 C after 300 cycles, with capacity retention of 76.15%. Under the same condition, NMC811 only shows specific capacity of 117.16 mAh/g with CE of 98.78% after 300 cycles and maintains 58.95% of its initial capacity. The results demonstrate enhanced rate and cycling stability of D-NMC811 at both room temperature and elevated temperature, as a result of the optimal Li<sup>+</sup> diffusion kinetics and improved structural stability.

### 2.4.3 EIS characterization

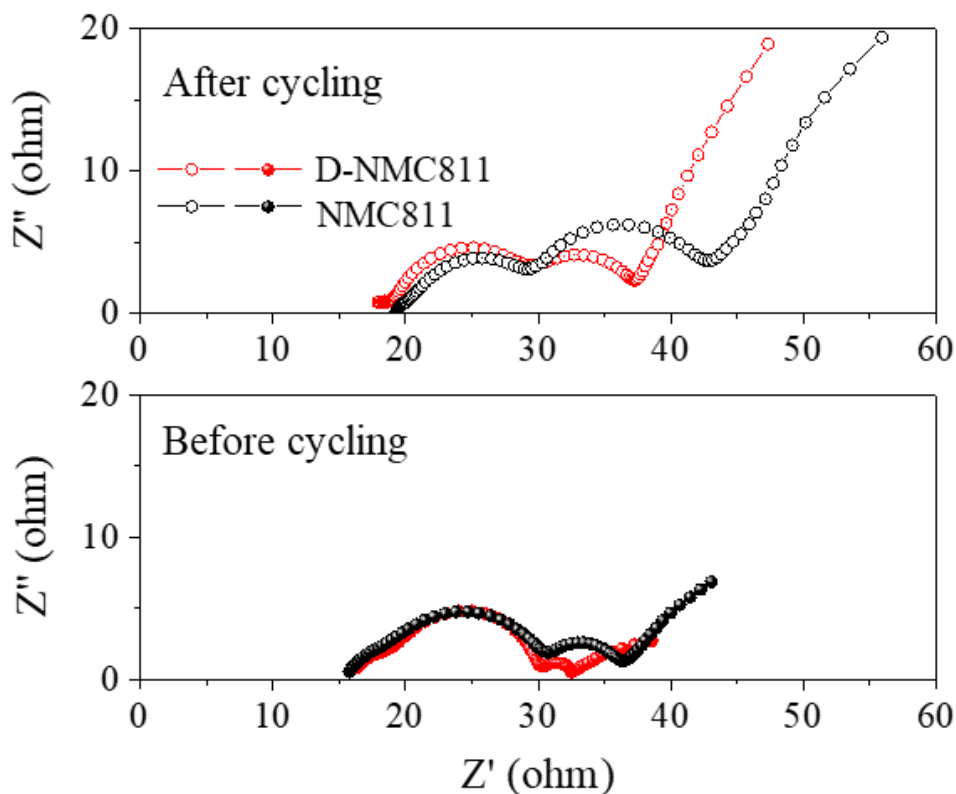


**Figure 2.17** Nyquist plots of the cells with D-NMC811 (red) and conventional NMC811 (black) before and after 100 cycles at 1 C, respectively (the coin cells were charged to 4.3 V and kept for 2 h before test).

Electrochemical impedance spectroscopy (EIS) was conducted on both NMC811 and D-NMC811 in the charged state of 4.3 V before and after cycling. The Nyquist plots of the two samples are shown in **Figure 2.17**. Before cycling, the charge transfer resistance ( $R_{ct}$ ), which can be determined by the second semicircle, is determined to be 36.9 and 32.7  $\Omega$  for NMC811 and D-NMC811, respectively. After cycling at 1 C for 100 cycles, the  $R_{ct}$  of D-NMC811 is 37.4  $\Omega$ , which is much lower than that of the regular NMC811 (43.0  $\Omega$ ). The resistance behaviors are related to the structural stability and SEI film on the surface.

## 2.4.4 dQ/dV characterization

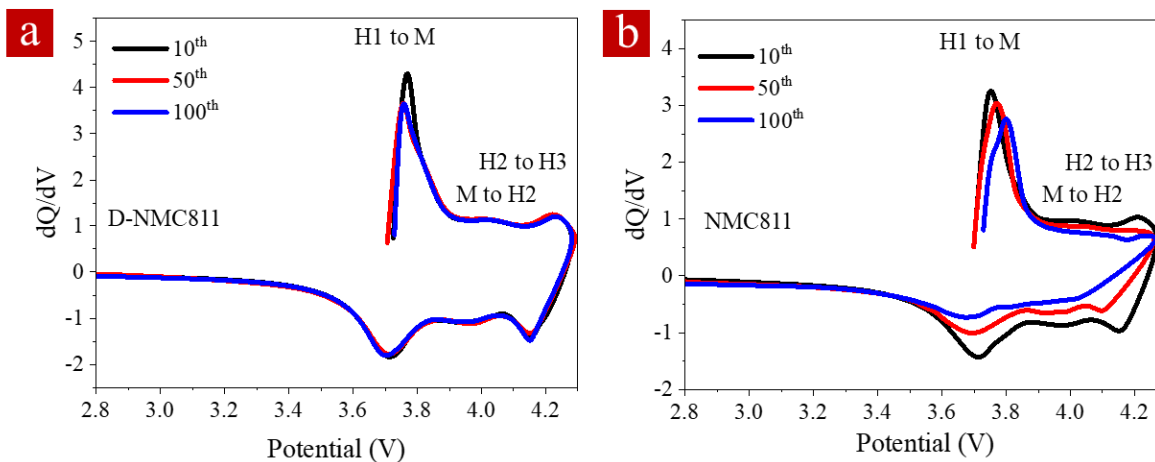


**Figure 2.18** dQ/dV vs potential plots of D-NMC811 (a) and conventional NMC811 (b) at 10th, 50th and 100th cycles.

To analyze the phase transformation behavior, dQ/dV curves of NMC811 and D-NMC811 after 10, 50 and 100 cycles are collected and plotted, as shown in **Figure 2.18 a and b**. The three redox peaks can be attributed to the phase transformation from hexagonal to monoclinic (H1 to M), monoclinic to hexagonal (M to H2), and hexagonal to hexagonal (H2 to H3). With increase of the cycle numbers, it can be found that the peaks corresponding to the phase transformation of M to H2 and H2 to H3 decrease. However, no obvious decrease is found on the peaks of D-NMC811, indicating high reversibility during cycling.

## 2.4.5 DSC measurement

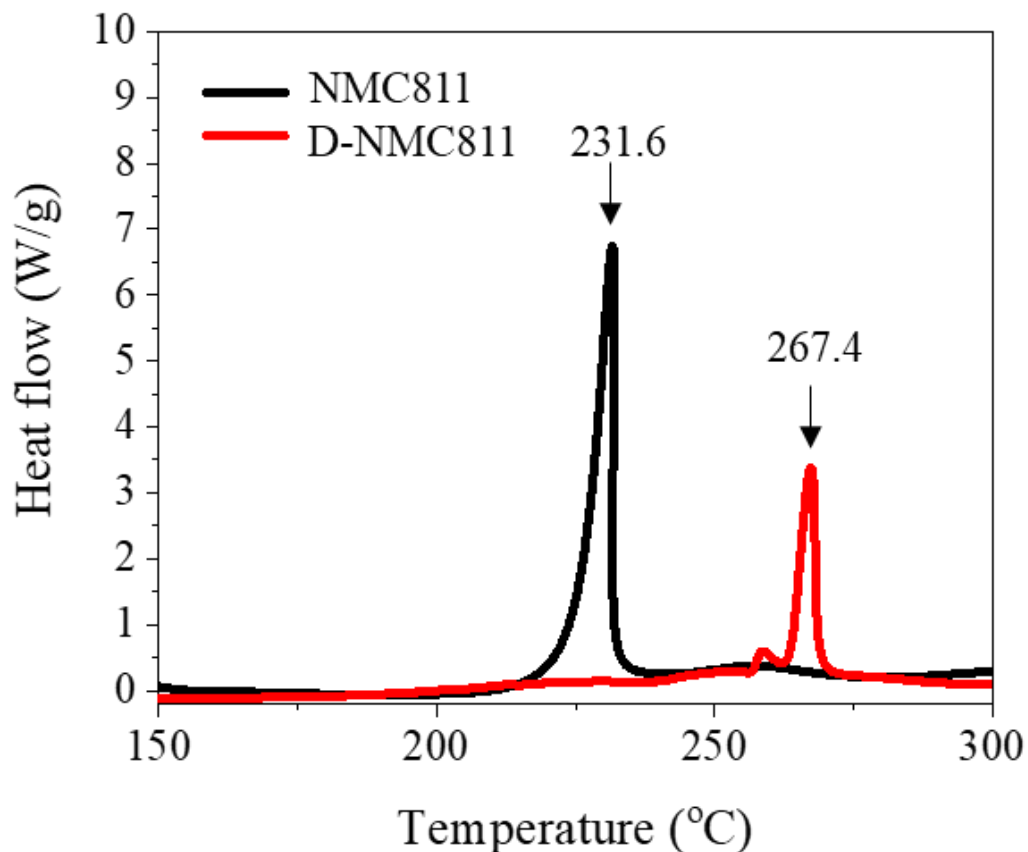


**Figure 2.19** DSC profiles of D-NMC811 and NMC811 at a scan rate of 10 °C/min in N<sub>2</sub> (The coin cells were charged to 4.3 V and kept for 2 h before disassembling in glovebox. The obtained electrode material and electrolyte with total mass of 10 mg were collected and sealed in aluminum pan in glovebox for test. ).

Differential scanning calorimetry (DSC) was used to further analyze the performance and thermal stability at elevated temperature. DSC of delithiated NMC811 and D-NMC811 at charged state of 4.3 V from coin cells are collected and shown in **Figure 2.19**. The phase transformation from layered structure to disordered spinel structure can happen on the surface due to the oxygen loss<sup>137</sup> It can be found that the regular NMC811 shows an exothermic peak at around 231.6 °C, which is

shifted to 267.4 °C by D-NMC811. At the same time, the reduced exothermic heat generation from 187.7 J/g to 71.1 J/g is also achieved by D-NMC811 (**Table S3**). As the layered-to-spinel phase transition propagates from the surface to the bulk,<sup>138</sup> the enhanced thermal stability can be attributed to the reduced Ni content and the presence of stable self-induced cation mixing layer on the surface. It has been reported that the thermal stability of Ni-rich cathode material can be significantly increased through increasing the relative Mn content and decreasing the Ni content, especially in the outer layer of the particles.<sup>77, 139</sup>

**Table 2-2** Calculated change in enthalpy for charged NMC811 and D-NMC811 cathode materials obtained from DSC curves as shown in Figure 2.19.

	<b>NMC811</b>	<b>D-NMC811</b>
Exothermic heat (J/g)	-187.7	-71.1
Exothermic Temperature (°C)	231.6	267.4

## 2.5 Full cell performance

Full cells were assembled by coupling the obtained NMC samples with graphite powders to evaluate the practicability in commercial application. The battery using regular NMC811 with negative/positive (N/P) ratio of 1.16 shows initial specific capacity of 173.22 mAh/g after activation and specific capacity of 125.05 mAh/g with CE of 98.61% after 300 cycles at 1/3 C, which maintains capacity retention of 72.19% (**Figure 2.20 a**). However, the battery using D-NMC811 exhibits specific capacity of 153.26 mAh/g with CE of 99.86% and higher capacity retention of 86.67% after cycling 300 times at 1/3 C. Pouch cells with total capacity of 300 mAh were also assembled as shown in **Figure 2.20 b**. After formation and activation process, the pouch cell using D-NMC811 delivers a total capacity of 297.62 mAh with CE of 99.48%. The specific capacity and energy density are calculated to be 172.81 mAh/g and 216.41 Wh/kg (**Figure 2.21 and Table 3**). After 500 cycles at 1 C, it still delivers a total capacity of 250.35 mAh, with capacity retention of 84.12%. For comparison, the pouch cell using NMC811 shows similar initial total capacity of 285.82 mAh and specific capacity of 166.03 mAh/g with CE of 96.50%. But the total capacity drops to 151.57 mAh with capacity retention of 53.03% after only 400 cycles.

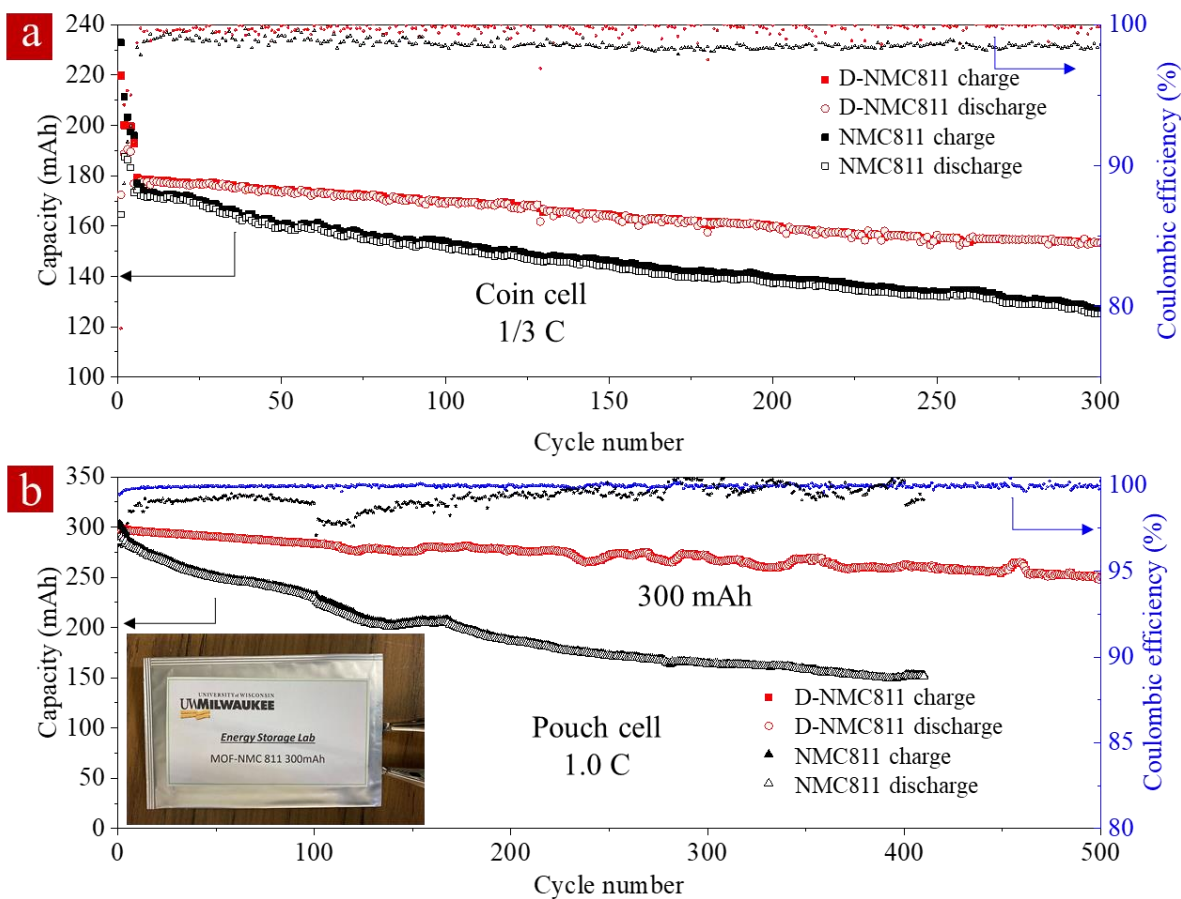


**Figure 2.20** (a) Full-cell battery cycling performance with D-NMC811 and NMC811 at 1/3 C. The cathode mass loading of the active material is  $\sim 8.2$  mg/cm<sup>2</sup>. The N/P ratio is 1.16. The battery was activated at 0.1 C for 4 cycles before cycling. (b) 300 mAh pouch-cell battery cycling performance with D-NMC811 and NMC811 at 1.0 C.

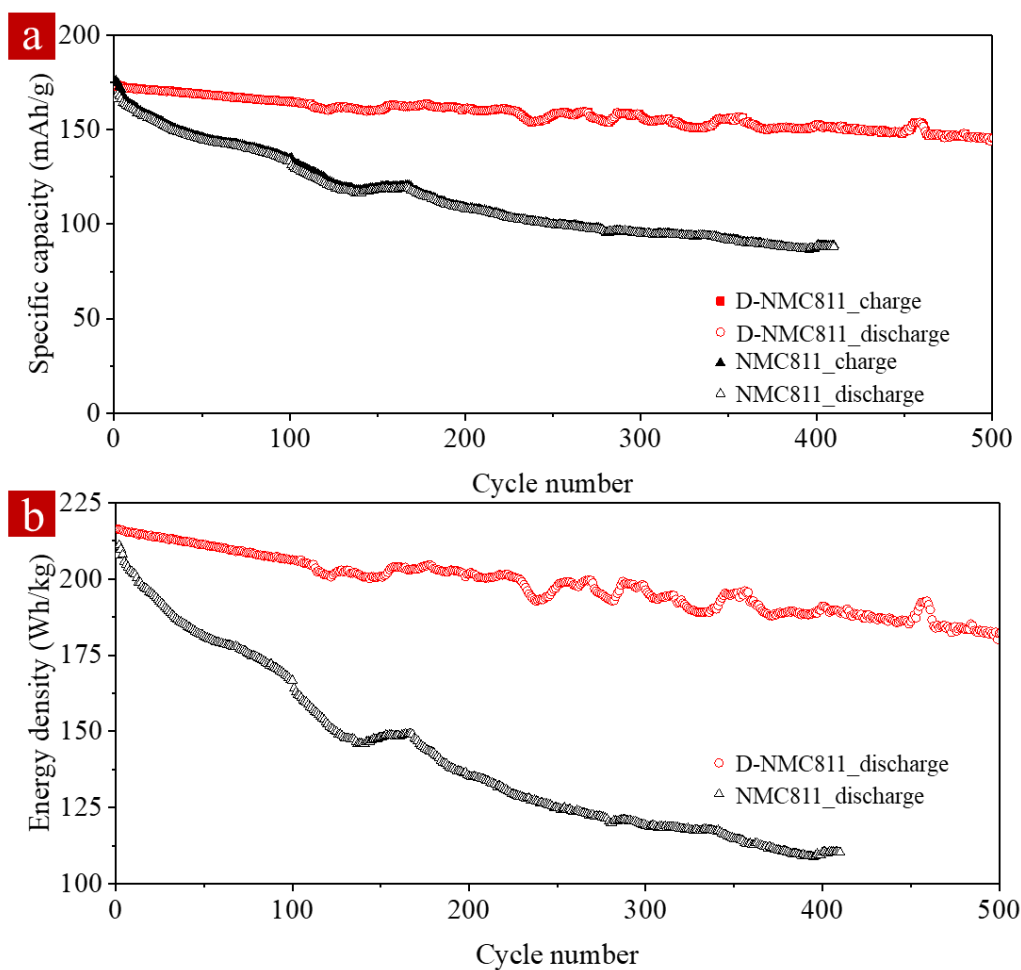


**Figure 2.21** Specific capacity (a) and the estimated energy density (b) evolution upon cycling of the full-cell pouch cells with D-NMC811 and conventional NMC811 as cathode electrode materials at 1.0 C, respectively. The pouch cell electrode was made with double-side coated cathode materials with a single side mass loading of  $\sim 12.2$  mg/cm<sup>2</sup> and a N/P ratio of 1.16.

**Table 2-3** Pouch cell detailed parameters

<b>Parameters</b>	<b>Mass (mg)</b>
Loading of graphite/(mg/cm <sup>2</sup> ) (double side coating)	13.6
Loading of NMC/(mg/cm <sup>2</sup> ) (double side coating)	24.4
Cathode areal capacity/(mAh/cm <sup>2</sup> )	4.22
Anode areal capacity/(mAh/cm <sup>2</sup> )	5.03
N/P ratio	1.19
E/C ratio/(g/Ah)	3
Discharge capacity (cathode)/(mAh/g)	172.8
Average discharge voltage/(V)	3.6
Anode/(mg/cm <sup>2</sup> )	14.4
Cathode/ (mg/cm <sup>2</sup> )	26.1
Al foil (T: 25μm)/(mg/cm <sup>2</sup> )	3.9
Cu foil/(mg/cm <sup>2</sup> )	7.65
Electrolyte/(mg/cm <sup>2</sup> )	12.6
Separator/(mg/cm <sup>2</sup> )	3.4
Estimated package foil and tabs (~3 wt%)	2.04
Total weight/(mg)	70.14
Energy density/(Wh/kg)	<b>216.4</b>

## 2.6 Characterization after cycling

### 2.6.1 Morphology and structure

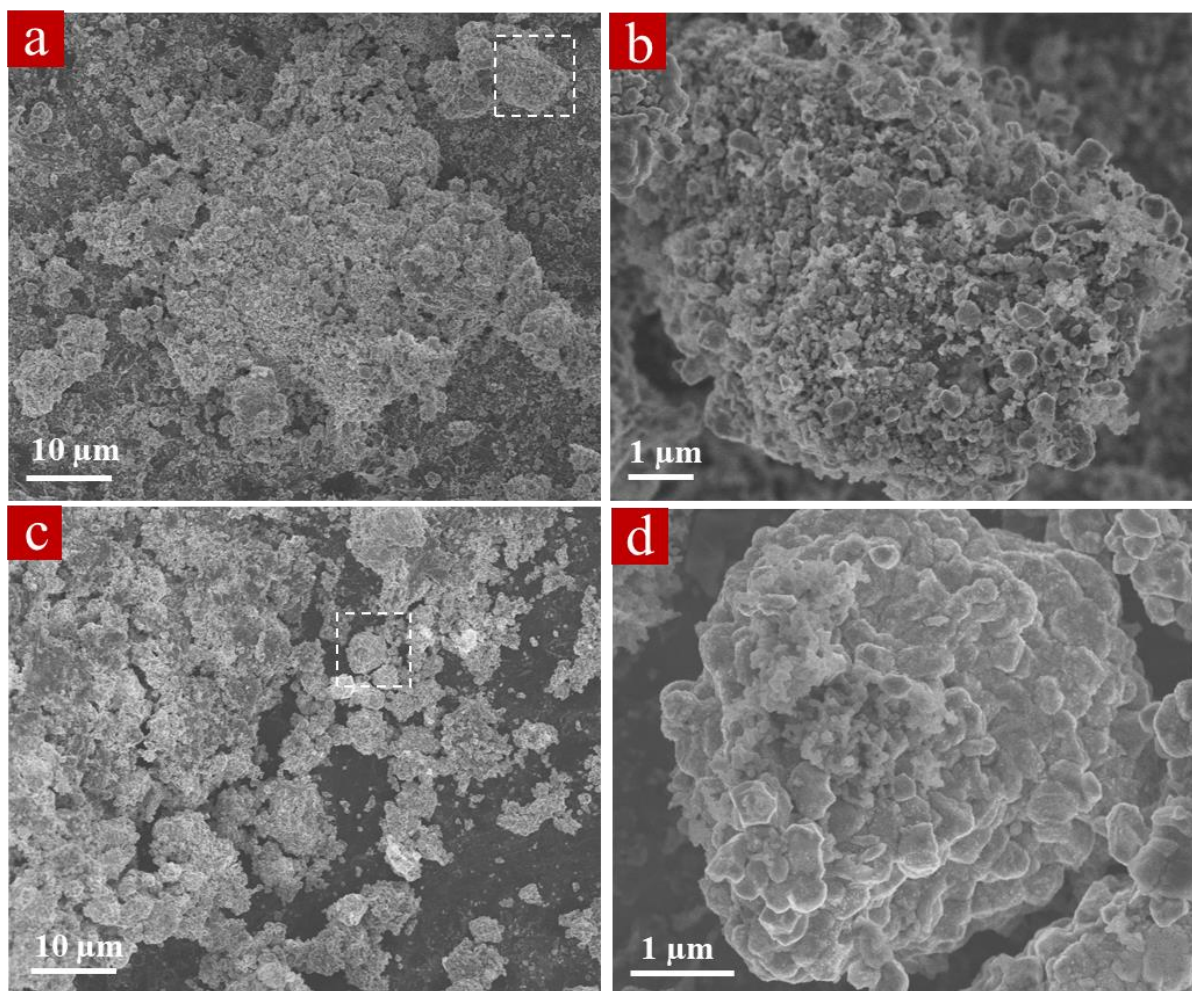


**Figure 2.22** Active material morphology evolution after 300 cycles at 1.0 C. SEM morphologies of the conventional NMC811 (a,b) and the D-NMC811 (c,d).

The structural and chemical stability are closely related to the electrochemical performance of NMC, which are further evaluated using SEM, HRTEM and XPS after cycling. **Figure 2.22** shows the SEM images of NMC811 and D-NMC811 after cycling 300 times at 1.0 C. As shown in **Figure 2.22 a and b**, severe pulverization of the secondary particles of the regular NMC811 is found after

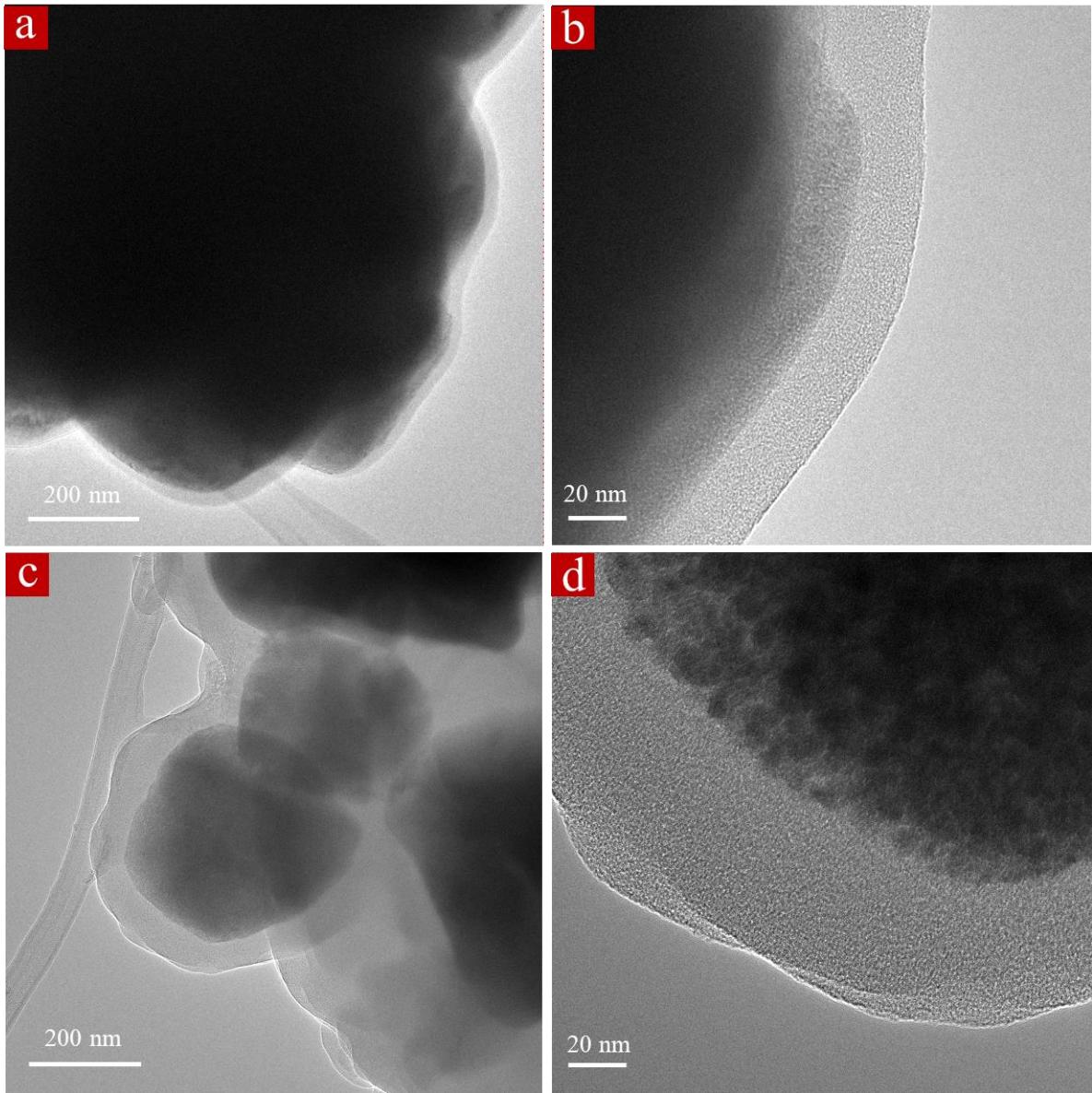


**Figure 2.23** TEM morphologies of the D-NMC811 (a,b) and conventional NMC811 (c, d) after 300 cycles at 1.0 C.

cycling, where individual primary particles with diameter of several hundred nanometers are loosely packed and formed large particles with diameter of  $\sim 10 \mu\text{m}$ . It is believed that intense microstrain at the grain boundaries is produced resulted from the anisotropic lattice variation during the repeated insertion/extraction of  $\text{Li}^+$  ions. The accumulation of strain may promote the initiation and development of cracks along the grain boundaries, resulting pulverization of the

secondary particles. At the same time, the primary particles spalled off from the secondary particles and lose electric contact with each other, resulting in the increase of resistance and capacity fading. The penetration of electrolyte along the cracks and grain boundaries would initiate side reaction on the new formed electrode/electrolyte interface. The induced  $\text{Ni}^{2+}$  by the side reaction can further migrate from the transition metal slab to lithium position due to similar ionic radius with  $\text{Li}^+$ , leading to structure degradation at the particle surface and resulting obvious capacity fading.<sup>69, 72</sup>

Thicker SEI and structure degradation are also found on the surface of NMC811 from the TEM image (**Figure 2.24 a and b**). However, the self-induced cation mixing thin layer on the surface of D-NMC811 effectively alleviate the generation of internal cracks by resisting the internal strain and suppressing phase transition within primary particles during cycling process. The unique feature of protective layer with concentration gradient on both primary and secondary particles can reduce the volume change and suppress the internal strain during de/lithiation process. Ni-rich cathode material is believed to undergo a volume change of approximately 9-10% due to phase transformation during lithiation/delithiation process, which would result in severe pulverization and cracking during cycling.<sup>73, 140, 141</sup> Surface coating can be applied to suppress the intergranular cracking caused by the microstrain during repetitive charge/discharge process. Here, the protective layer on the surface of primary particles can reduce the volume change as the function of coating layer. At the same time, the concentration gradient is believed to reduce the structure mismatch of conventional coating layer caused by the different degrees of expansion/shrinkage of the core and shell.<sup>73</sup> As a result, after 300 cycles at 1 C, the D-NMC811 still maintain its original secondary particles with closely packed primary particles (**Figure 2.22 c and d**). The TEM images (**Figure 2.23 c and d**) also exhibit relatively thinner SEI and undegraded surface of the primary particles.

## 2.6.2 XPS characterization

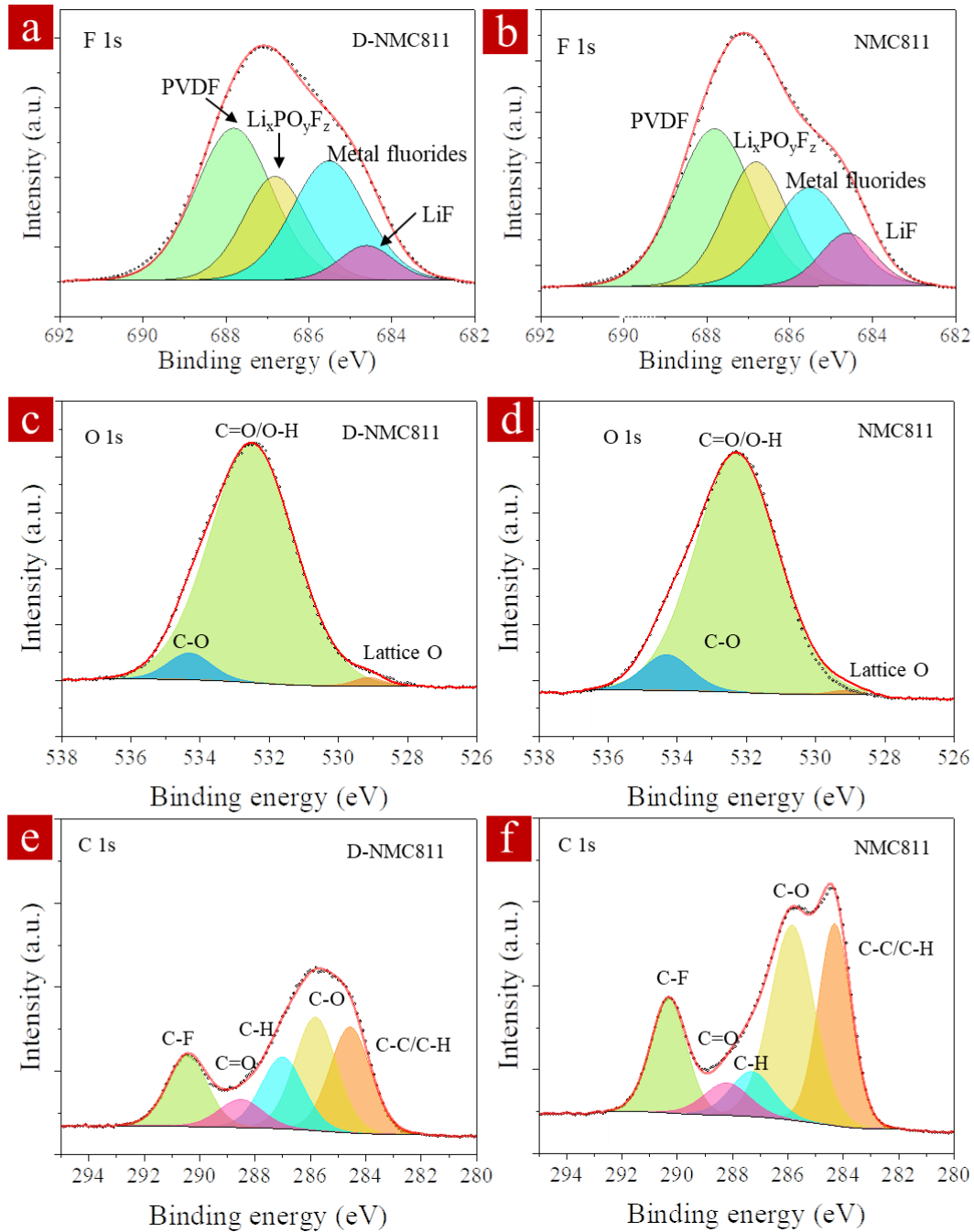


**Figure 2.24** The corresponding XPS spectra of F1s, O1s, and C1s of D-NMC811 (a, c, e) and the conventional NMC811 (b, d, e).

XPS was also applied to analyze the chemical bonding change after cycling, as shown in **Figure 2.24**. The F 1s spectra of D-NMC811 and the conventional NMC811 after 300 cycles at 1.0 C are shown in **Figure 2.24 a and b**. The F 1s profile was fitted to four separated peaks at 684.6 eV, 685.5 eV, 686.8 eV, and 687.8 eV, corresponding to LiF, metal fluorides,  $\text{Li}_x\text{PO}_y\text{F}_z$ , and PVDF, respectively. The peak intensity of NMC811 at 684.6 eV and 686.8 eV, corresponding to LiF and  $\text{Li}_x\text{PO}_y\text{F}_z$ , are greater than that of D-NMC811. The relative areal ratio of  $\text{Li}_x\text{PO}_y\text{F}_z$  and LiF to PVDF for NMC811 and D-NMC811 are calculated to be 88.3% and 72.3%, respectively, which indicates the presence of thicker SEI.<sup>142</sup> This can be attributed to the effective suppression of side reaction and the formation of thicker SEI by the unique structure on both primary and secondary particles of D-NMC811. The O 1s peak can be assigned to TM-O, C=O/O-H, and C-O at 529.2 eV, 532.4 eV, and 534.2 eV, respectively. Compared with NMC811, D-NMC811 shows much greater peak of TM-O at 529.2 eV, providing further evidence of the thinner SEI. At the same time, similar peaks of C=O/O-H and C-O are found on both NMC811 and D-NMC, suggesting the possible involvement of the solvent in the formation of SEI.<sup>143</sup>

### 2.6.3 Ex situ XRD

*Ex situ* XRD was used to check the lattice parameter change of the NMC811 and D-NMC811 at 4.3 V and 4.5 V, respectively, as shown in **Figure S10**. The lattice parameters were obtained from the Rietveld refinement (**Table S4**). Compared with the original state, the unit cell volume shrinkage at 4.5 V for NMC811 is 4.80%. Due to the benefits from the unique structural feature,

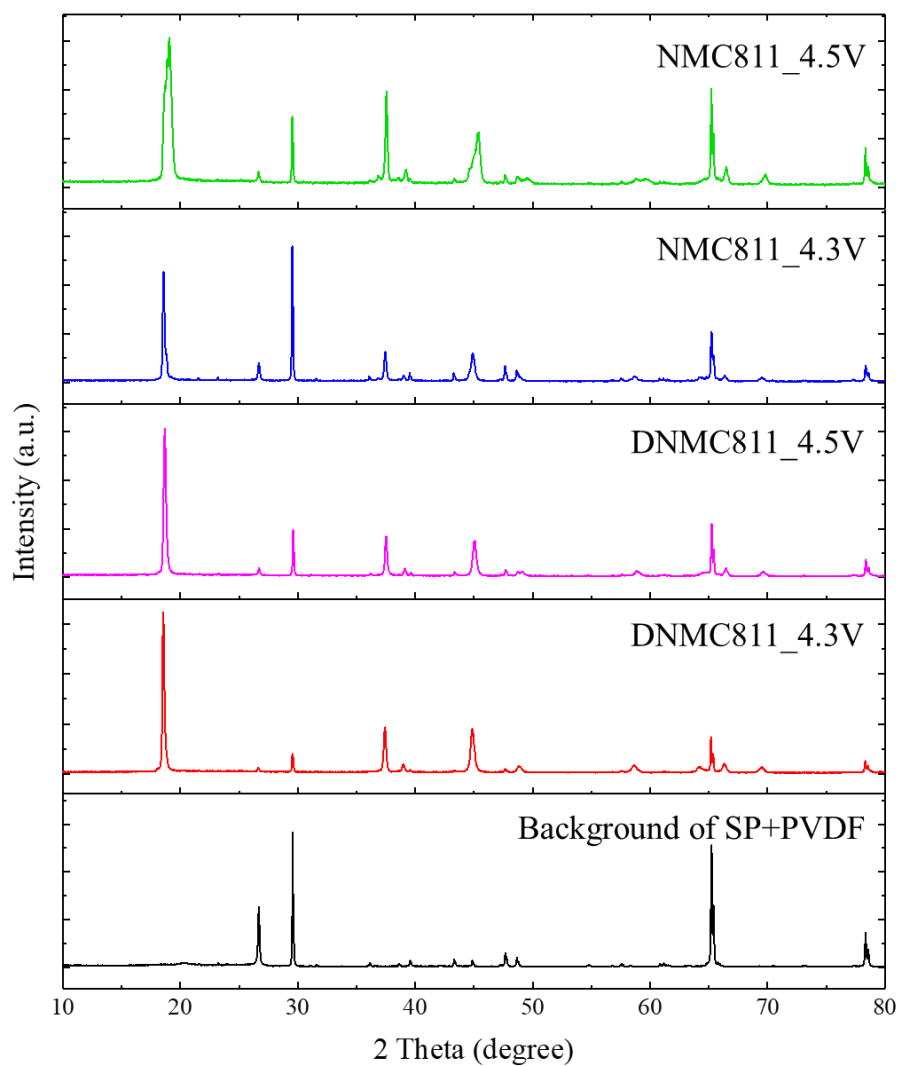


**Figure 2.25** EX situ XRD patterns for NMC811, D-NMC811 at 4.3 V and 4.5 V, respectively.

the volume change of D-NMC811 is suppressed as 2.35% (**Figure 6g**).

**Table 2-4** Lattice parameters from the Rietveld refinement of the D-NMC811 and conventional NMC811.

Samples	Potential (V)	$a$ (Å)	$c$ (Å)	$V$ (Å <sup>3</sup> )	$R_{wp}$ (%)
NMC811	4.3	2.81892	14.31922	98.543	5.71
	4.5	2.81256	14.07644	96.433	6.21
D-NMC811	4.3	2.82437	14.44514	99.792	6.54
	4.5	2.81781	14.34937	98.670	8.81

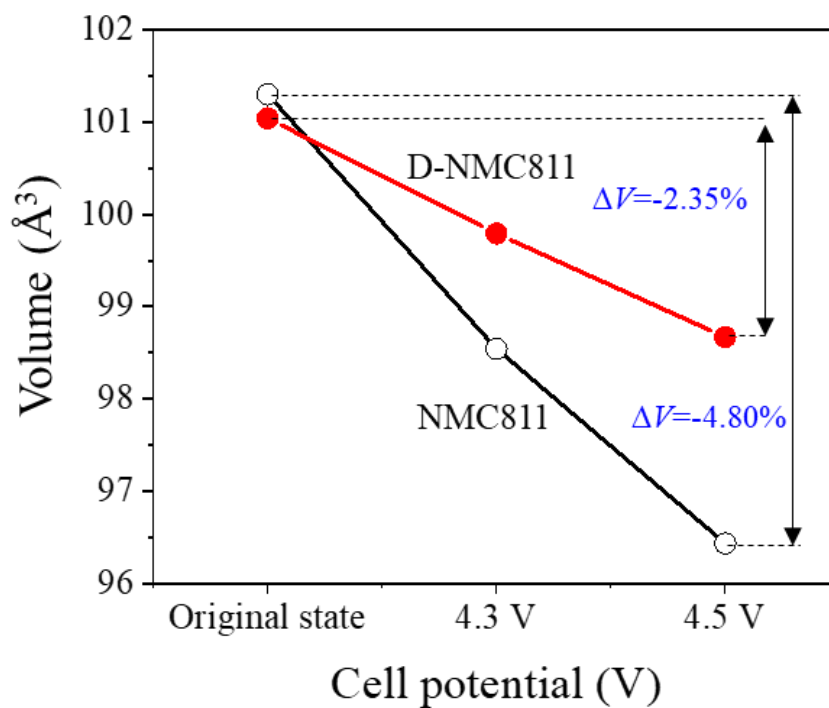


**Figure 2.26** The lattice parameter of  $V$  calculated by Rietveld refinement of the XRD patterns for NMC811 and D-NMC811 at original state, 4.3 V, and 4.5 V, respectively.

## 2.7 Conclusion

In this work, a novel designed Ni-rich cathode material with concentration gradient on both primary and secondary particles was synthesized through incorporation of Ni-MOF during the coprecipitation process. The reduced Ni content and oxidation state on the surface of primary particles significantly enhance the electrochemical stability during cycling and thermal stability at elevated temperature through inhibiting the generation of internal cracks through resisting the internal strain and suppressing phase transition within primary particles during cycling process. At the same time, the high Ni content in the bulk of the secondary particles still promotes high specific capacity of the material, while the outer shell with low Ni content further improves the stability. And the self-induced cation mixing layer on the surface of primary particles due to the presence of Ni-MOFs during calcination process can significantly reduce the  $\text{Li}^+/\text{Ni}^{2+}$  disordering through blocking the Li diffusion pathway from the bulk to the surface. All these features make the prepared D-NMC811 deliver high thermal stability, favorable specific capacity, and excellent cycling stability. Compared with regular NMC material and other modification methods, easy operation and high capacity retention at different rates were achieved, which significantly improves the practicability for commercial application. The building of gradient on both primary and secondary particles also provides a promising design route for the optimization of Ni-rich cathode materials with high energy density, long life, and enhanced safety. In addition, the synthesis method through incorporation of Ni-MOFs does not change the conventional production process of NMC, which makes it a more promising candidate to be scaled up.

## 2.8 Experimental

### 2.4.1 Synthesis of Ni-MOF

Ni-MOF was synthesized based on previous reported method.<sup>144</sup> Certain amount of  $\text{Ni}(\text{CH}_3\text{CO}_2)_2 \cdot 4\text{H}_2\text{O}$  (99%, Acros Organics) was added and dissolved in the solution of dimethylformamide (DMF, Sigma-Aldrich), ethanol and DI water with ratio of 1:1:1 under magnetic stirring at room temperature. After the addition of 2,5-dihydroxyterephthalic acid (98%, Sigma-Aldrich), the mixture was stirred at room temperature to get a homogeneous solution. The obtained solution was transferred into a 100 ml Teflon liner and sealed in stainless steel autoclave. It was then reacted at 120 °C for 24 h. The obtained solid was collected through centrifugation. After washing with fresh DMF and methanol, the collected powders were dried at 80 °C under vacuum. Before used as seeds for the synthesis of NMC811, the Ni-MOF powders were treated at 180 °C for 5 h to remove the residual.

### 2.4.2 Synthesis of NMC811 and D-NMC811

Coprecipitation method was used to prepare D-NMC811. For more details, 100 ml of transition-metal solution containing 0.76 M  $\text{NiSO}_4 \cdot 6\text{H}_2\text{O}$  (Aldon Corp Se), 0.1 M  $\text{CoSO}_4 \cdot 7\text{H}_2\text{O}$  (99%, Acros Organics), and 0.1 M  $\text{MnSO}_4 \cdot \text{H}_2\text{O}$  (99%, Acros Organics) was prepared. Certain amount of Ni-MOF was dispersed in the obtained transition-metal solution to make the ratio of Ni:Co:Mn to be 8:1:1. The amount of Ni-MOF was calculated based on the Ni content from TGA. All the solutions were stored under the protection of  $\text{N}_2$ . Certain amount of DI water was poured into the reactor as base solution. After adjusting the pH to desired value using solution of NaOH and  $\text{NH}_3 \cdot \text{H}_2\text{O}$ , the base solution was stirred and heated under the protection of  $\text{N}_2$  gas. After 30 min, the transition-metal solution with Ni-MOF was pumped into the reactor with flow rate of ~0.5 ml/min.

Simultaneously, a solution of NaOH and  $\text{NH}_3 \cdot \text{H}_2\text{O}$  was pumped into the reactor at the similar rate. The pumping rate was further tuned to maintain the stable pH value. The pH and temperature were carefully controlled during the reaction. The stirring rate was also increased gradually. After the feeding was completed, the reaction was continued for 5 h. After washing with DI water for several times, the precipitate was collected through vacuum filtration and dried at 100 °C for 12 h. The precursor was mixed with 105% stoichiometric amount of  $\text{LiOH} \cdot \text{H}_2\text{O}$  (98%, Alfa Aesar) through ball milling. The mixture was calcinated at 800 °C for 16 h in pure oxygen. The obtained sample was marked as D-NMC811. For comparison, NMC811 was prepared using the same method only without the adding of Ni-MOF.

### **2.4.3 Electrochemical measurement**

The slurry was prepared by mixing active material, conductive carbon (SuperP) and PVDF with the ratio of 80:10:10 in N-methyl-2-pyrrolidone (NMP, Honeywell). To form the electrode, the slurry was coated on carbon coated Al foil (MTI Corp.), and dried in vacuum oven at 60 °C for 12 h. After being pressed under 6–10 MPa using a benchtop hydraulic press (Northern Tool+ Equipment), the electrode was pouted into the circle disc using a disc cutter (MSK-T-07, MTI Corp.). The stainless-steel coin cells (CR2032, Xingye Co., Ltd.) with the obtained electrode, polyethylene separator (Celgard 2400), and lithium foil (MTI Corp.) were assembled at room temperature in an argon-filled glovebox. The electrolyte used was 1 M  $\text{LiPF}_6$  in ethylene carbonate (EC) and ethyl methyl carbonate (EMC) (3:7 volume ratio) with 10 % FEC and 2 % vinylene carbonate (VC) as additives. The assembled coin cells were tested by galvanostatic cycling using a battery tester system (2001CT, Landt Instruments, Inc.) after resting at room temperature for 4 h. Before cycling at different rates, all the coin cells were subjected three cycles at 0.1 C for initial activation. The charge and discharge rates were calculated based on the theoretical capacity of

NMC811 (1 C=200 mAh/g). NMC811 and D-NMC811 with mass loading of 5-6 mg/cm<sup>2</sup> were used as cathode material to assemble full cell battery with (MCMB) graphite powder (MesoCarbon MicroBeads, MTI Corp.). All the full cells were activated for three cycles at 0.1 C. Pouch cells with total capacity of 300 mAh and N/P ratio of 1.16 were also assembled. Detailed

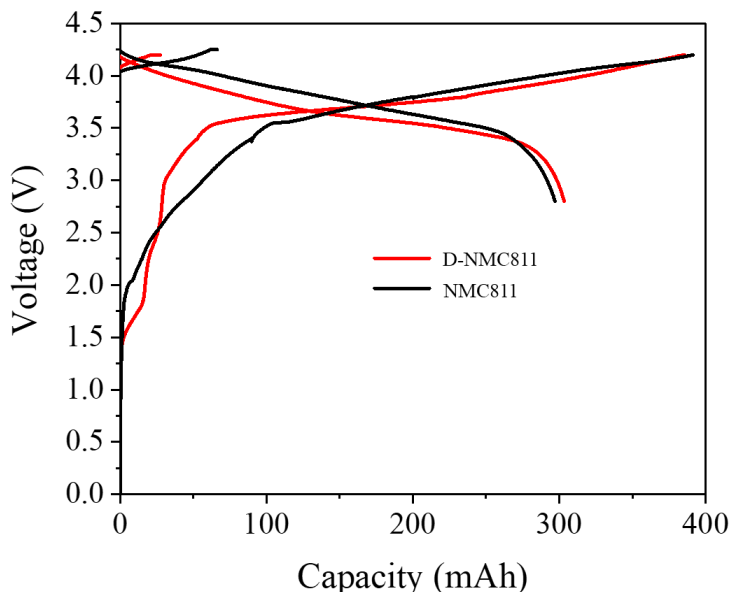


**Figure 2.27** Formation and activation process of the obtained pouch cells with D-NMC811 and conventional NMC811 as cathode electrode materials, respectively.

formation curves are listed in **Figure 2.27**. The detailed formation and activation process of pouch cells can be described as: charge at 0.05 C to 3.4 V, rest for 5 min, charge at 0.1 C to 3.8 V, rest for 5 min, charge at 0.2 C to 4.25 V, rest for 24 h at 45 °C under pressure. After release the gas and seal the cell, the pouch cell is charged at 0.1 C to 4.25 V, followed by charging at 4.25 V until the current is lower than 1 mA. After resting for 5 min, it is discharged to 2.8 V at 0.1 C. Then all the pouch cells were charged/discharged at 1 C. The cyclic voltammetry (CV) was measured using a Gamry Reference 600+ potentiostat with a scan rate of 0.1 mV/s at room temperature.

Potentiostatic EIS was measured using Gamary Reference 600+ potentiostat in the range of 0.01 to  $10^5$  Hz at charged state.

#### **2.4.4 Sample characterization**

Hitachi S4800 ultrahigh resolution field emission scanning electron microscopy (FESEM) and JEOL JEM-ARM200CF 200 kV STEM/TEM, which was affiliated with a probe aberration corrected high-angle annular dark-field scanning transmission electron microscopy (HAADF-STEM) mode imaging were used to characterize the structure and morphology of NMC samples. The EDS element mapping was checked under 200 kV accelerating voltage with an image resolution of less than 0.08 nm and energy resolution of 0.35 eV. The surface area and pore volume of the samples were carried out by nitrogen sorption/desorption using a Micromeritics ASAP 2020 system at 77 K and analyzed based on Brunauer-Emmett-Teller theory. X-ray diffraction (XRD) was measured on a Bruker D8 Discover X-ray Diffractometer using Ni filtered Cu  $K\alpha$  radiation with applied current and voltage of 40 mA and 40 kV, respectively. after being dissolved in aqua regia ( $\text{HNO}_3\text{:HCl}$  in ratio of 1:3), the elementary composition of the obtained NMC cathode materials were determined using inductively coupled plasma mass spectrometer (ICP-MS, Thermo Fisher Element 2). X-ray photoelectron spectroscopy (XPS) was performed on Thermo Scientific ESCALAB 250Xi equipped with an electron flood gun and a scanning ion gun. The spectra were collected using an ultrahigh vacuum (UHV) apparatus with a base pressure below  $1 \times 10^{-10}$  Pa. The sample was irradiated using an Al  $K\alpha$  line (a photon energy of 1486.6 eV) of a non-monochromatic X-ray source. The emitted electrons were detected using a hemispherical analyzer under an angle of  $45^\circ$  to the surface normal. All the data were calibrated using the C 1s peak at 284.8 eV. Thermal gravimetric analyzer (TGA, TA Instruments SDT650) with a heating rate of  $10^\circ\text{C}/\text{min}$  and air flow rate of 50 ml/min was used to determine the Ni content in the obtained Ni-

MOFs. The differential scanning calorimetry (DSC) analysis was conducted using TA Instruments Q200 with a heating rate of 10 °C/min under N<sub>2</sub> atmosphere. Before the test, the NMC cathode materials were fully charged to 4.3 V at 0.1 C and kept at 4.3 V for 2 h in coin cells. 10 mg of electrode materials with electrolyte were collected from the current collector and sealed in aluminum pan for test after disassembling in glovebox. *Ex situ* XRD were obtained using cathodes, which were charged to the target voltage at 0.1 C and kept at target voltage for 2 h before disassembling. Before test, the cathodes were immersed in DME (Dimethoxy ethane) for 30 min to remove the electrolyte residual and dried in glovebox at room temperature.

# CHAPTER 3 Development of Si-Based Anode for Li-Ion Battery with Largely Improved Performance

## 3.1 Introduction

The most commonly used anode material for LIBs is graphite currently. However, the low specific capacity of 372 mAh/g limits the application of graphite as the anode for next-generation LIBs. A lot of efforts have been spent on the research of anode materials with high performance. Except graphite, Si, Sn, Ge and some other materials are showing great potential as advanced anode with high performance. Among them, Si is regarded as the most promising candidate for next generation anode for LIBs, due to its high capacity and availability. Compared to graphite, the theoretical capacity of silicon can reach 4200 mAh/g, which is much higher than that of the current used graphite and other anode materials. However, as discussed in **section 1.3**, some problems still limit the application of Si, including severe crystallographic expansion upon lithiation process, slow lithium diffusion, and high reactivity at high states of charge, resulting in particle cracking, particle isolation, electrolyte reactivity, and electrode delamination issues. A lot of efforts have been applied to overcome the issues limiting the application of silicon, such as core-shell structure, yolk-shell structure, porous structure, SiO<sub>x</sub>/C composite, Si nanoparticles, and some other 2d and 3d structures. But the complex manufacturing and high cost become another obstacle blocking the practical application of Si anode material.

Instead of pure Si, Si-based materials have been successfully applied as an additive in traditional graphite anode to increase the capacity. Currently, the commercial Si-based anode includes SiO<sub>x</sub>/C (420 mAh/g), SiC (450 mAh/g) anode, Si-graphene anode (600 mAh/g). There are only several

commercially available products of Si anode in the market. More research facilities and companies are spending a lot of effort on developing and promoting the commercialization of Si anode.

Among various modification and construction methods applied on Si anode, micro-sized architectures with nano-structured Si have demonstrated promising battery performance. At the same time, it is more favorable for industrial application. However, bare micro-sized Si without further modification showed a capacity loss of about 80% of its initial capacity with poor cycling stability due to the severe pulverization.<sup>18</sup> Building of a thin protective layer on the surface of Si has been proved to be effective on improving the electrochemical performance.<sup>145-147</sup> Polymer-based materials also provide a promising choice as the protective layer for Si materials, due to its light-weight, relative easy synthesis procedure, low cost, and some other advantages.<sup>148-150</sup> Some conductive polymers, such as polypyrrole (PPy), have been successfully applied as conductive additives or advanced binders in LIBs, which can be regarded as candidates as the protective layer for Si anodes.<sup>119, 151-154</sup>

In this section, a novel scalable synthesis of large silicon cage composite (micrometers) which is composed of a Si skeleton and an ultra-thin (<5 nm) mesoporous polypyrrole (PPy) skin *via* a facile wet-chemical method is proposed. Toward practical application, commercial available micro-sized AlSi alloy was used as the precursor. Under this configuration, the hollow skeleton with empty space provides sufficient space to accommodate the drastic volume expansion/shrinkage upon charging/discharging. The conductive PPy can provide protection and increased conductivity as a protective layer to enhance fast channel for Li<sup>+</sup>/e<sup>-</sup> transport. During the electrochemical performance test, the battery with the micro-silicon ( $\mu$ -Si) cage as anode displays an excellent capacity retention upon long cycling at high charge/discharge rates and high material loadings. A specific capacity of ~1660 mAh/g with Coulombic efficiency (CE) of ~99.8% was

achieved after 500 cycles at 0.2 C with mass loading of 3 mg/cm<sup>2</sup>. Similar specific capacity with CE of 99.4 % was also obtained after 400 cycles at 0.2 C with loading of 4.4 mg/cm<sup>2</sup>. At 1.0 C, a capacity as high as 1149 mAh/g was remained after 500 cycles with high mass loading. The areal capacity of as high as 6.4 mAh/cm<sup>2</sup> with 4.4 mg/cm<sup>2</sup> loading was obtained, which ensures a high battery energy density in powering large devices such as electric vehicles.

The data shown in this section has been summarized and published.<sup>155</sup>

### 3.2 Design strategies and preparation of $\mu$ -Si cage

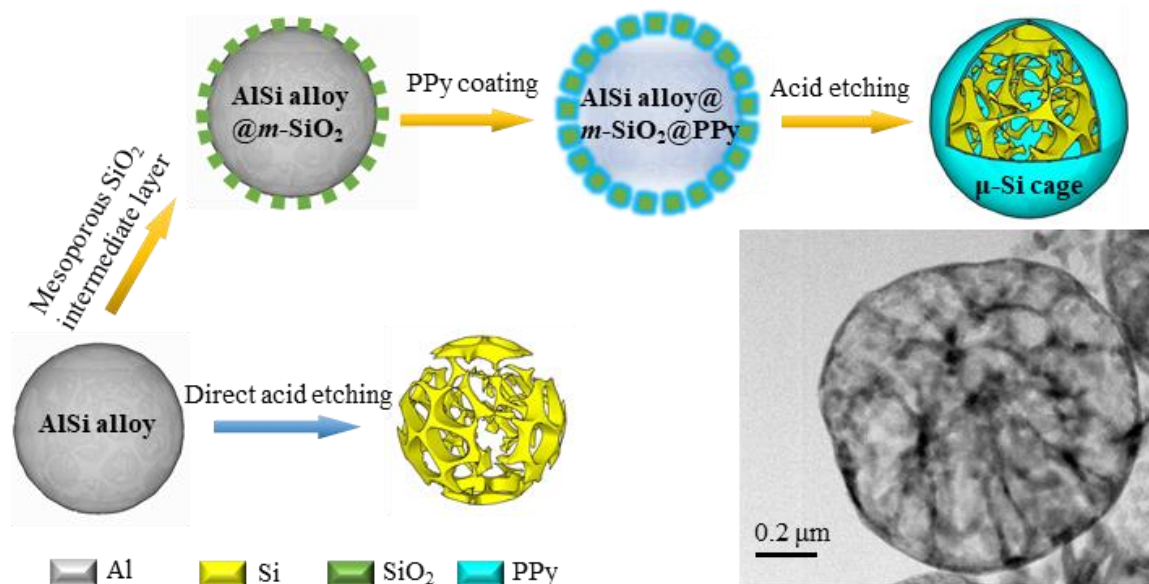


**Figure 3.1** Scalable synthesis of  $\mu$ -Si cage using AlSi micro-spheres as precursor by chemical method (Copyright © 2019, American Chemical Society).<sup>155</sup>

In this work, a micrometer silicon skeleton caged inside a mesoporous PPy layer *via* a simple chemical process was synthesized.<sup>155</sup> First, compared with Si nanoparticles, the application of micro-sized Si ensures the high tapped density, which is important to maintain high mass loading when applied as anode for practical application. Second, the commercially available micro-sized AlSi alloy is selected as the precursor, which can significantly reduce the difficulty during scalable production. Third, the synthesis of conductive PPy is relatively easy and low-cost, which shows great potential for scalable production. Based on the above features, the mass loading of  $\mu$ -Si cage can reach as high as 4.4 mg/cm<sup>2</sup> with an areal capacity of 6.4 mAh/cm<sup>2</sup> under 0.2 C. In addition, the high cycling stability upon long cycling and high charge/discharge rate capability, which can be attributed to the presence of Si skeleton and PPy with enhanced conductivity, make the  $\mu$ -Si

cage a promising candidate for high performance LIBs targeting the broad applications.

The synthesis route of the the  $\mu$ -Si cage is shown in **Figure 3.1**. Typically, the AlSi alloy microspheres (Al: 87-89 wt%; Si: 11-13 wt%) were first covered with an intermediate, mesoporous  $\text{SiO}_2$  ( $m$ - $\text{SiO}_2$ ) layer, through a classic sol-gel reaction using TEOS. The presence of this  $m$ - $\text{SiO}_2$  leads to the adsorption of PPy precursor and the formation of uniform PPy layer on the surface. Subsequently pyrrole monomer was added into the mixture, generating a thin PPy layer on the surface *via* polymerization using iron chloride as oxidant in an ice bath. Hydrochloride acid was used to remove the Al component in the AlSi alloy to form the Si skeleton. Then, hydrofluoric acid with low concentration was used to remove the Al residual and  $m$ - $\text{SiO}_2$  to form the hollow Si skeleton encaged by PPy layer, as shown in the TEM image of **Figure 3.1**.

### 3.3 Characterization

#### 3.3.1 Morphology of the $\mu$ -Si cage

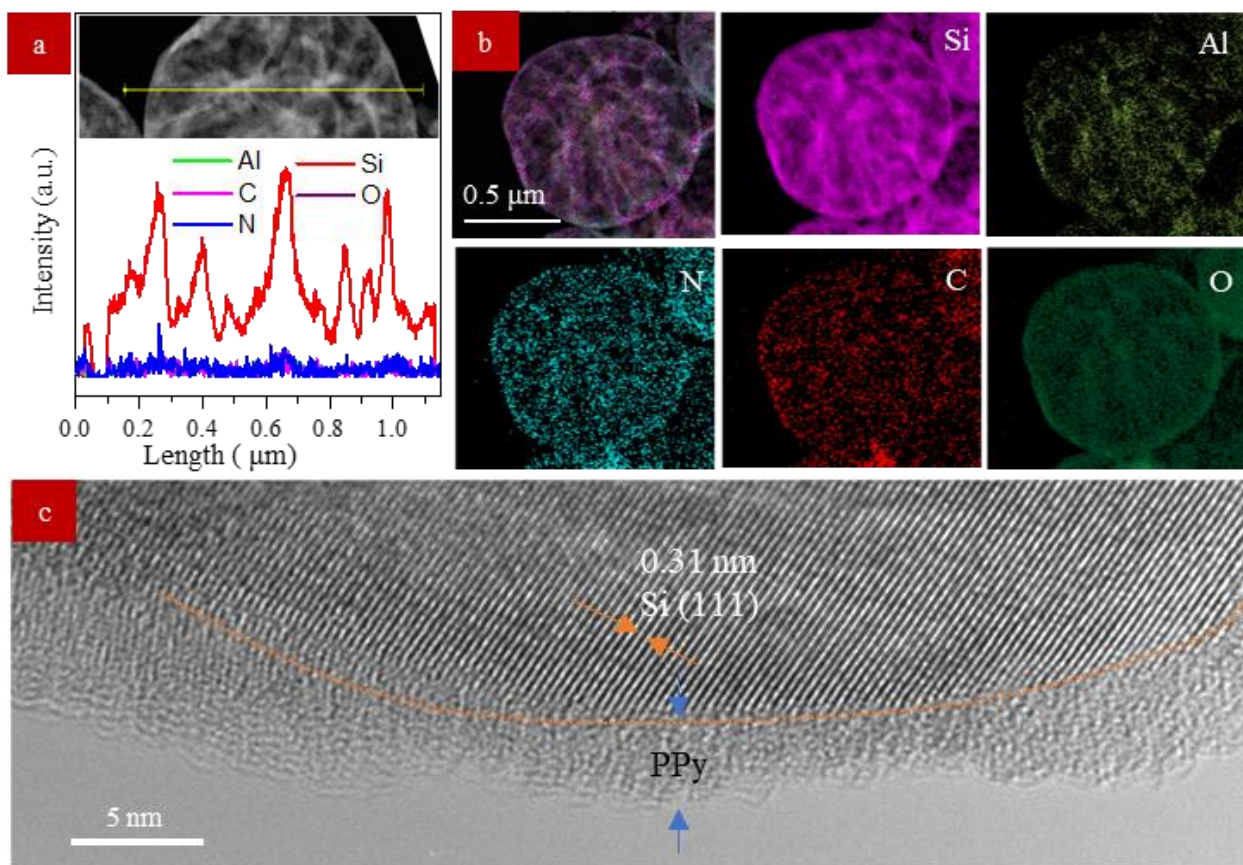


**Figure 3.2** TEM morphology (inset) of  $\mu$ -Si cage. Line elemental mapping (a) and area elemental mapping (b) of a  $\mu$ -Si cage. High-resolution TEM image of the edge of a  $\mu$ -Si cage (c).<sup>155</sup>

The chemical composition and element distribution of the formed  $\mu$ -Si cage was checked using EDS, as shown in **Figure 3.2**. As observed from the element linear scanning (**Figure 3.2 a**), a series of strong Si peaks appear intermittently across the cage, indicating a hollow, tree-like skeleton structure. However, the intensity of N and C, which are the main components of the PPy polymer, are very low. It confirms the ultra-thin thickness of the PPy coating layer. Figure 3.2 b

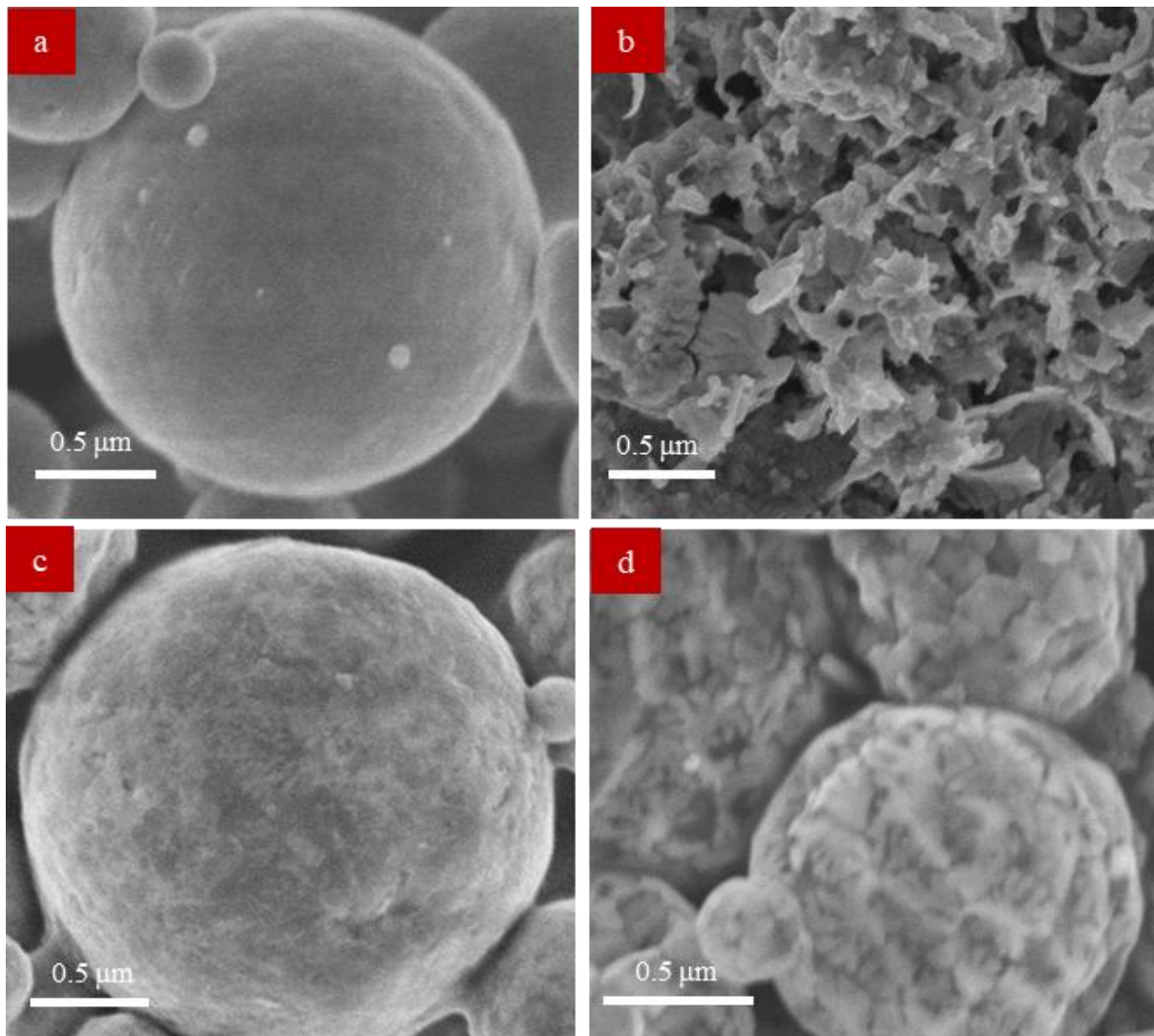


**Figure 3.3** Morphology and chemical composition of the sample with different etching processes. SEM images of pure AlSi alloy before (a) and after (b) direct acid etching. SEM images of  $\mu$ -Si cage before (c) and after (d) acid etching (Copyright © 2019, American Chemical Society).<sup>155</sup>

shows the EDS element mapping of the obtained  $\mu$ -Si cage. First, the tree-like mapping of the Si was observed, revealing the structure of the Si skeleton. While the spherical shape of the N and C confirms the uniform coverage of PPy. At the same time, there are very small amounts of Al and O are found on the surface of Al/SiO<sub>2</sub>, which is produced from the possible surface oxidation. A single crystal structure with clear lattice fringes of a  $\sim 0.31$  nm spacing corresponding to the Si (111) plane are found on the HRTEM (**Figure 3.2c**). **Additionally, the thickness of amorphous**

PPy layer was determined to be about 4-5 nm from the HRTEM image.

The morphology and chemical composition of the samples were further investigated using scanning electron microscopy (SEM). The AlSi alloy precursor shows spherical shape with a size of  $\sim 3 \mu\text{m}$  and a smooth surface (**Figure 3.3 a**). A collapsed morphology with randomly ordered silicon flakes was observed after removing the Al by direct acid etching (**Figure 3.3 b**). However, after covered by the intermediate  $m\text{-SiO}_2$  and PPy layer, the spherical shape of the alloy was

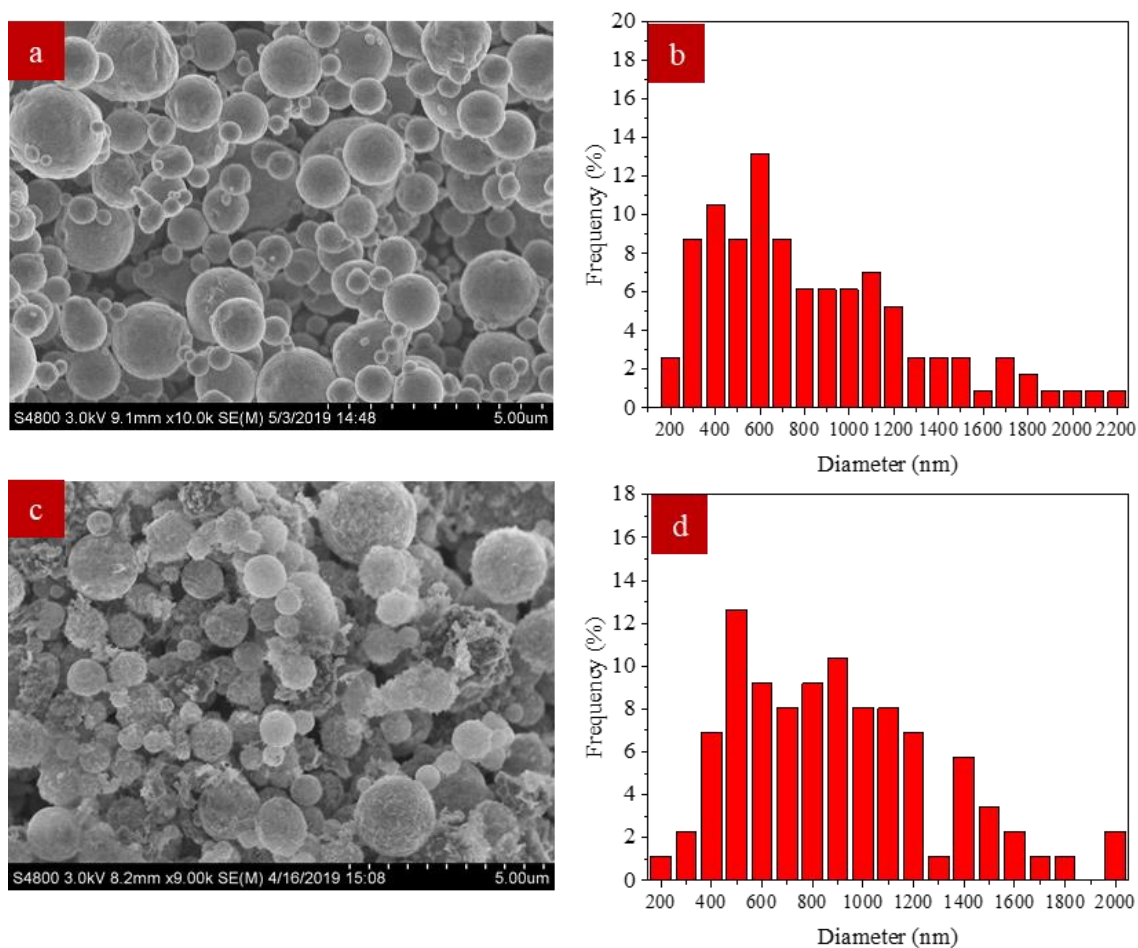


**Figure 3.4** SEM images and corresponding size distribution of the AlSi alloy (a, b) and  $\mu\text{-Si}$  cage (c, d) (Copyright © 2019, American Chemical Society).<sup>155</sup>

maintained while with a relatively rough surface, as displayed in **Figure 3.3 c**. A rougher surface with more porous configurations was formed after selectively removing the Al and the  $m\text{-SiO}_2$

layer (**Figure 3.3 d**), which is in agreement with the pore analysis from the BET results as shown in **Figure 3.8**.

The particle size distribution of the original AlSi alloy and obtained  $\mu$ -Si cage were also analyzed through SEM images, as shown in **Figure 3.4**. The particle size was measured based the corresponding SEM images. And it can be found that the general size of the particle was still remained after the polymer coating, compared with the original AlSi alloy particles.

### 3.2.2 XRD characterization

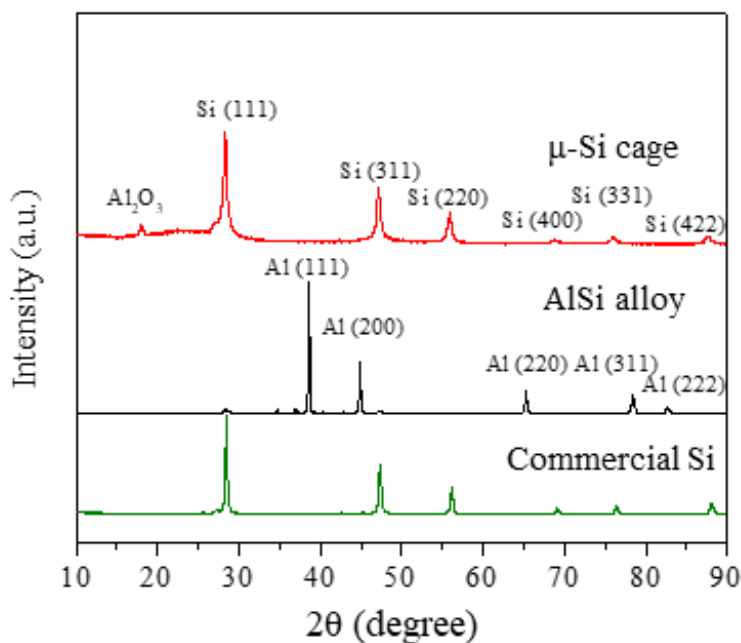


**Figure 3.5** XRD patterns of the  $\mu$ -Si cage (red), AlSi alloy (black) and commercial Si (green) (Copyright © 2019, American Chemical Society).<sup>155</sup>

The phase information of the samples was further checked using X-ray diffraction (**Figure 3.5**). It is seen that the AlSi alloy precursor has two phases: large portion of Al and small portion of Si

(black). After forming the  $\mu$ -Si cage, the relatively strong peaks of Si with the major crystalline planes of (111), (220), (311), (400), (331) and (422) remain while the Al peaks disappear (red). A very weak peak of  $\text{Al}_2\text{O}_3$  is also found due to the incomplete reaction in the etching step. More Al residues can be found with less etching (6 hours) while the Si can also be removed if over-etched (24 hours). In order to obtain a high purity of silicon skeleton, a moderate etching of 12 hours is selected.

### 3.2.3 TGA

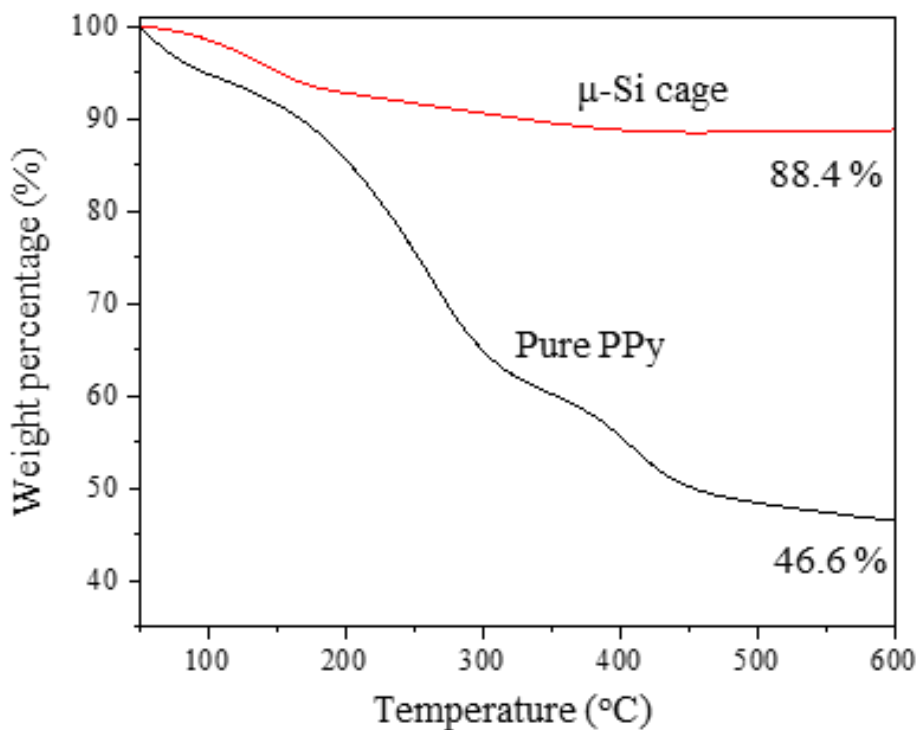


**Figure 3.6** TGA analysis of the  $\mu$ -Si cage (red) and pure PPy (black) under  $\text{N}_2$  (Copyright © 2019, American Chemical Society).<sup>155</sup>

The specific capacity of the composite is closely related to the accurate Si content in the  $\mu$ -Si cage composite. Thermogravimetric analysis (TGA) of  $\mu$ -Si cage and pure PPy were applied with a heating rate of  $5^\circ\text{C}/\text{min}$  under  $\text{N}_2$  flow of  $50\text{ mL}/\text{min}$  (Figure 3.6). It can be found that the Si ratio

in the  $\mu$ -Si cage composite is as high as 78.3 wt% along with a small amount of PPy, ensuring the high specific capacity of the composite.

### 3.2.4 BET analysis

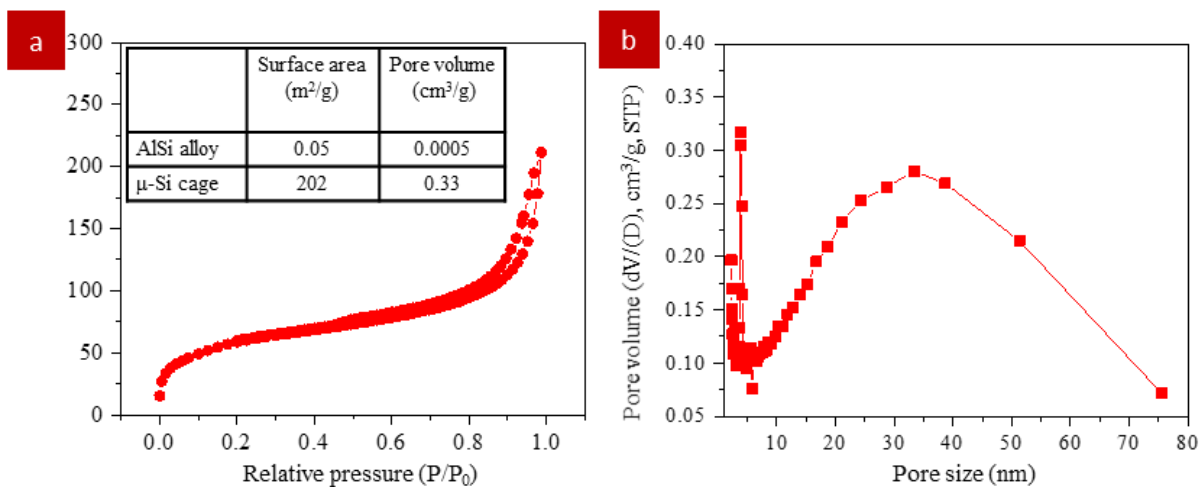


**Figure 3.7** Nitrogen sorption-desorption isotherm (a) and the pore size distribution curve (b) of  $\mu$ -Si cage. The inset of (a) is the comparison of surface area and pore volume between AlSi alloy and  $\mu$ -Si cage (Copyright © 2019, American Chemical Society).<sup>155</sup>

The surface area and the pore structure were analyzed using the nitrogen-adsorption isotherm (**Figure 3.7**). A remarkably lifted surface area of 202 m<sup>2</sup>/g with a pore volume of 0.33 cm<sup>3</sup>/g of the  $\mu$ -Si cage was received based on the Brunauer-Emmett-Teller (BET) calculation. In contrast, the AlSi alloy only shows a very low surface area of 0.05 cm<sup>2</sup>/g and a pore volume of 0.0005 cm<sup>3</sup>/g. The type IV isotherm of the  $\mu$ -Si cage with a sharp capillary condensation at high relative pressure and H1 hysteresis loop indicates the existing large amounts of channel-like mesopores. The pore size distribution curve elucidates two major sizes: ~3.6 nm and 34.0 nm (**Figure 3.7 b**). The pores centered at ~34.0 nm is originated from the large interval of the PPy layer and the space inside the skeleton, which provide sufficient pathways for fast diffusion of Li ions through the electrolyte. It should be noted the volume larger than 100 nm inside the cage was not calculated by the BET measurement.

### 3.2.5 Etching process analysis

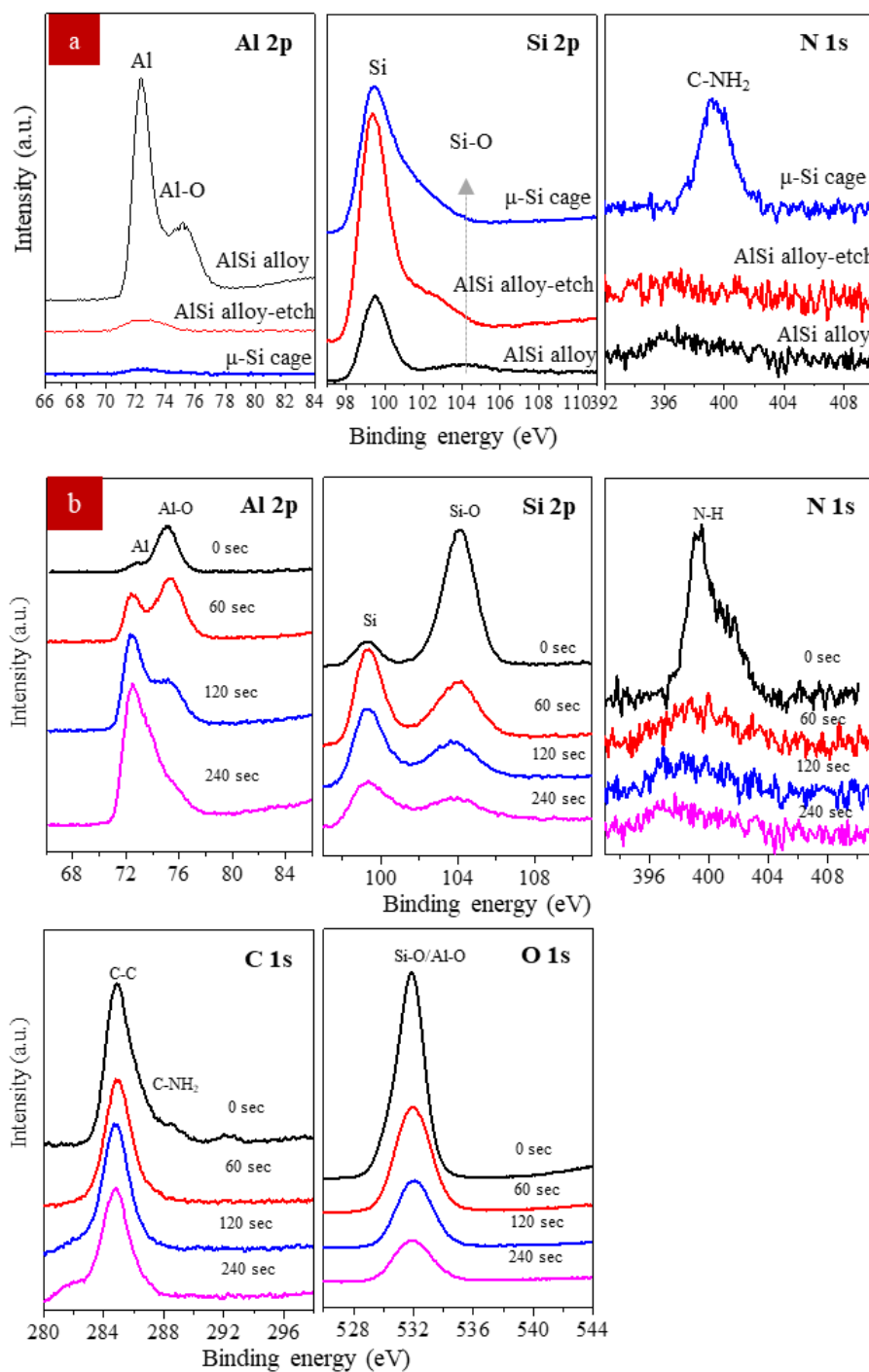


**Figure 3.8** XPS analysis (a) of pure AlSi alloy (black), AlSi alloy after direct etching (red) and  $\mu$ -Si cage (blue). (b) XPS depth profiling of the  $\mu$ -Si cage before etching (Copyright © 2019, American Chemical Society).<sup>155</sup>

As shown from the XPS data, two strong peaks of Al 2p at 72.3 eV and 75.3 eV are derived from the abundant Al and Al<sub>2</sub>O<sub>3</sub> of the AlSi alloy (**Figure 3.8 a, black**). A weak hump peak of the alloy after direct etching is found (**red**) while this peak becomes more negligible with PPy layer (**blue**), indicating the most Al of the  $\mu$ -Si cage was successfully removed. Compared to Al 2p, the peaks of Si 2p show an opposite evolution (**Figure 3.8**). The AlSi alloy exhibits a Si 2p peak at 99.4 eV along with a shoulder peak at 103.9 eV those are related to Si and SiO<sub>2</sub>, respectively (**black**). After removing Al, both samples show a clear increase of the silicon peak at 99.4 eV (**red and blue**).

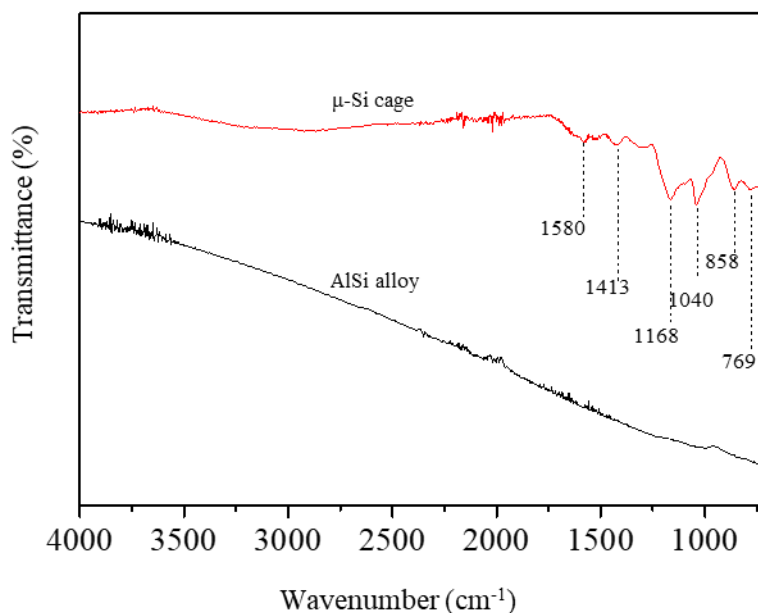


**Figure 3.9** FTIR curves of pure AlSi alloy (black) and the  $\mu$ -Si cage (red) (Copyright © 2019, American Chemical Society).<sup>155</sup>

However, the  $\mu$ -Si cage with PPy shows only the peak of silicon, which implies the covered polymer layer suppressed the oxidation. The N 1s peak at 400.0 eV corresponding to -NH<sub>2</sub> bonding in PPy is only found in the  $\mu$ -Si cage sample. The structure of the PPy layer on  $\mu$ -Si cage was further confirmed using Fourier-transform infrared spectroscopy (FTIR) analysis (**Figure 3.10**). The peak at 1580 cm<sup>-1</sup> is assigned to the C=C and C-C bonds in ring-stretching mode while the

peak at  $1413\text{ cm}^{-1}$  corresponds to the C=C and C–N bonds in stretching mode. The bond vibration at  $1040\text{ cm}^{-1}$  is related to the –C–H group in-plane deformation. The peaks at below  $900\text{ cm}^{-1}$  are ascribed to C–H/N–H/C=C–C/C=C–N/C–N–C out-of-plane bending.<sup>156</sup> The characteristic bipolaron bands at  $1168\text{ cm}^{-1}$  indicate that the PPy is in its doped state.<sup>157</sup>

In order to better understand the structure evolution during the synthesis, the AlSi alloy@PPy before etching was also investigated (**Figure 3.10**). The high contrast Al, Si and O mappings show the spherical morphology with certain oxides inside (**Figure 3.10**), which are similar to the AlSi alloy precursor. The circle shapes of C and N present the formation of PPy layer outside (**Figure 3.10**) while the original alloy does not. The images in **Figure 3.10** display a uniform, thin coverage of PPy on the alloy. XPS depth measurements were carried out to study the chemical composition

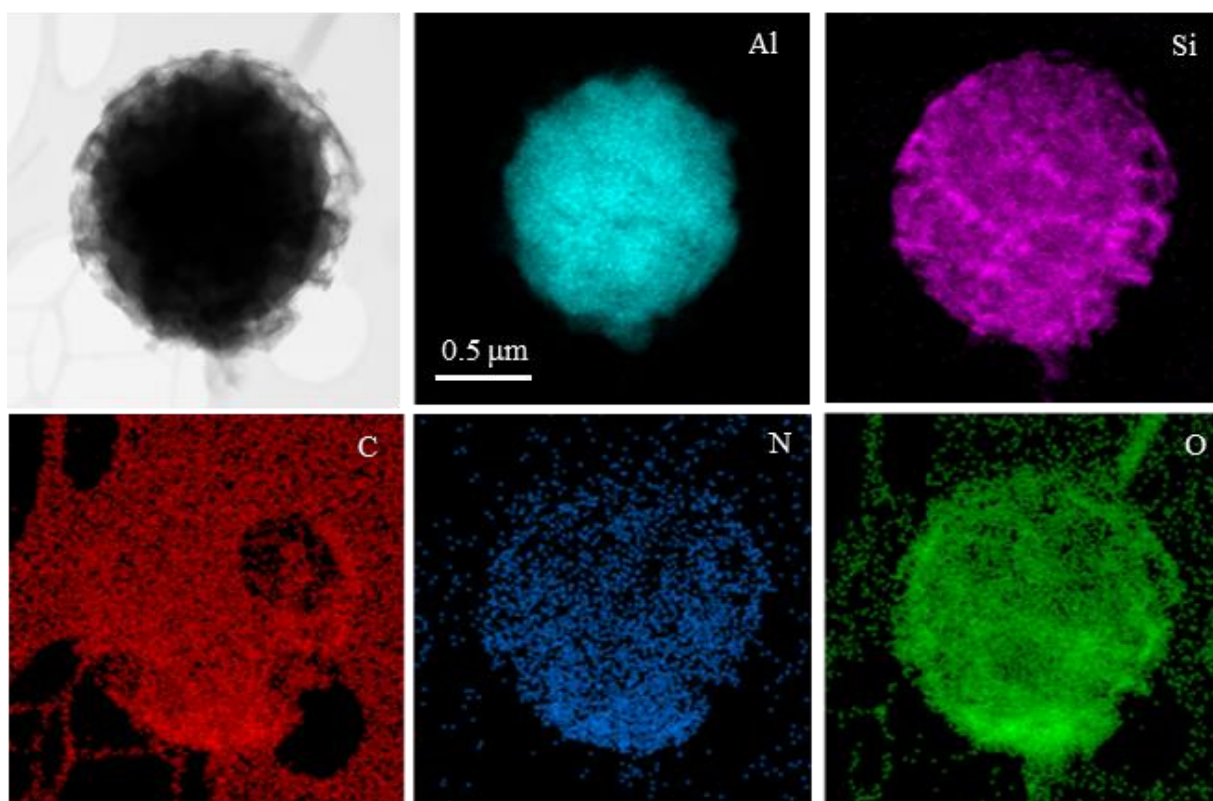


**Figure 3.10** Morphology and chemical composition of  $\mu$ -Si cage before etching. Elemental mapping of the  $\mu$ -Si cage before etching (Copyright © 2019, American Chemical Society).<sup>155</sup>

of the  $\mu$ -Si cage. As shown in **Figure 3.8 b**, the intensity of the peaks of Al 2p and Si 2p gradually increases while the intensity of peaks of C 1s, N 1s and O 1s decreases with longer ion etching time, indicating the PPy layer is located outside the AlSi alloy. The peaks of Al 2p at 75.3 eV ( $\text{Al}_2\text{O}_3$ ) and Si 2p at 103.9 eV ( $\text{SiO}_2$ ) are decreased from the surface to center, indicating most oxides exist outside the particles.

### 3.3 Electrochemical performance

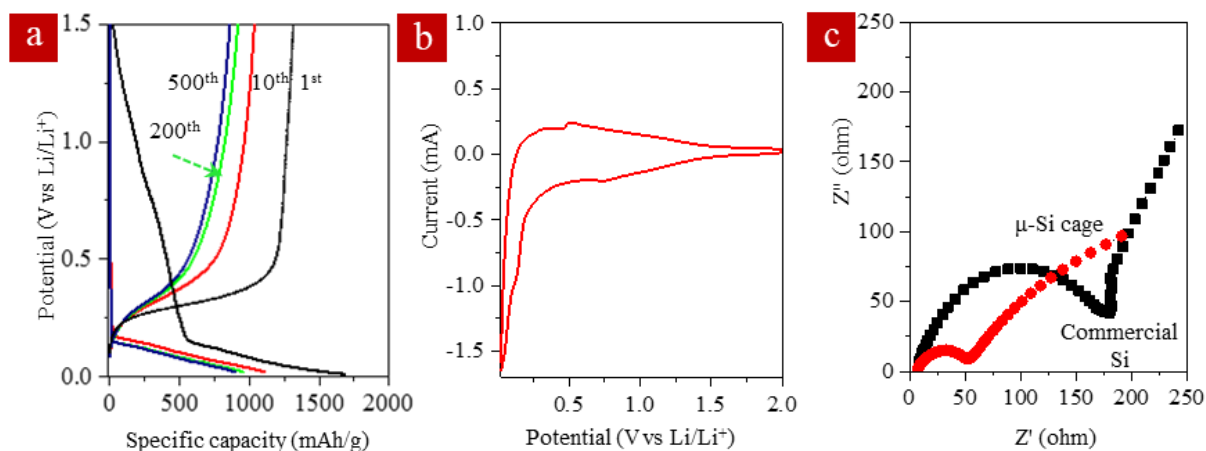


**Figure 3.11** Galvanostatic charge/discharge profile of  $\mu$ -Si cage with a loading of 3 mg/cm<sup>2</sup> at 1.0 C (a) (the first cycle is activation at 0.2 C with a coulombic efficiency of 78.17%). Cyclic voltammetry of the battery with  $\mu$ -Si cage as anode at 2nd cycle with a scan rate of 0.05 mV/s (b). Nyquist plots of  $\mu$ -Si cage (red) and commercial Si (black) at 5th cycle at 0.2 C obtained from EIS measurements (c) (Copyright © 2019, American Chemical Society).<sup>155</sup>

The charge/discharge profiles of the battery under varying rates with the  $\mu$ -Si cage as anode and Li metal as counter electrode display the typical charge potential at 0.32 V and discharge potential at 0.08 V (**Figure 3.11 a**). The  $\mu$ -Si cage composites also show a Coulombic efficiency of 78.2% in the first cycle. It is seen that the voltage platform increased significantly during the first 10 cycles. However, it only displayed slightly change in the following cycles, especially from 200th cycle to 500th cycle, which indicates an improved cycling stability. The corresponding cyclic voltammetry curve shows the negligible peak over 0.5 V, which indicates a less SEI layer formation (**Figure 3.11 b**). The two broad delithiation peaks centered at 0.35 and 0.53 V during charge process are attributed to the de-alloying of  $\text{Li}_x\text{Si}$  to Si, while the lithiation peaks around 0.02-0.2 V during discharge process are from the electrochemically-driven solid-state alloying  $\text{Li}_x\text{Si}$  (in fully lithiated status,  $x \approx 4.4$ ). The reduced charge transfer resistance with the  $\mu$ -Si cage

(~50 ohms) in contrast to the commercial silicon particles (~183 ohms) after 5 cycles from the EIS result (**Figure 3.11 c**) implies the enhanced charge transfer kinetics through the mesoporous membrane.

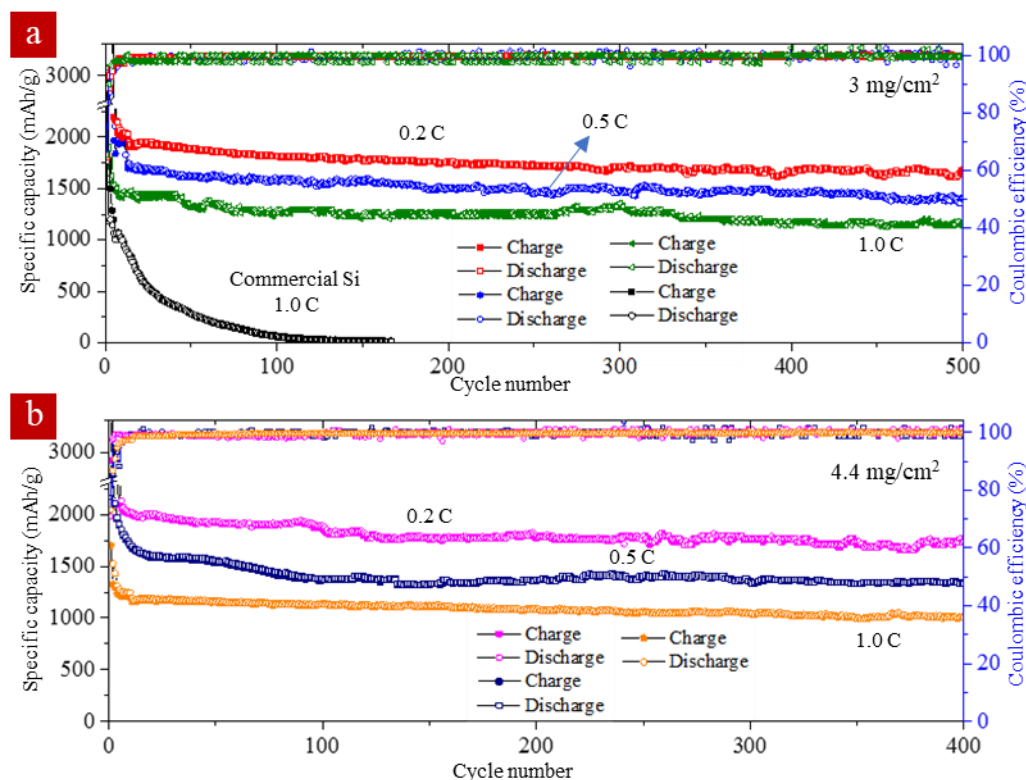


**Figure 3.12** Cycling performance of the battery with  $\mu$ -Si cage as anode with loadings of  $3 \text{ mg/cm}^2$  (a) and  $4.4 \text{ mg/cm}^2$  (b) at various rates of 0.2, 0.5 and 1.0 C, respectively. The specific capacity was calculated based on the pure silicon inside  $\mu$ -Si cage. The black curve in (a) is the battery performance with commercial silicon as anode. The Coulombic efficiency was calculated at 0.2 C (Copyright © 2019, American Chemical Society).<sup>155</sup>

The cycling performance of the batteries with different  $\mu$ -Si cage loadings at various rates was investigated. As seen from **Figure 3.12 a**, the battery with  $3 \text{ mg/cm}^2$   $\mu$ -Si cage exhibits high specific capacities of  $\sim 1980 \text{ mAh/g}$  at 0.2 C (**red**),  $\sim 1700 \text{ mAh/g}$  at 0.5 C (**blue**) and  $1430 \text{ mAh/g}$  at 1.0 C (**green**) at the 20<sup>th</sup> cycle, respectively. High capacity retention of 1660, 1430 and 1149 mAh/g along with a high CE of 99.8 % was respectively achieved after 500 cycles. As a

comparison, the battery with commercial silicon exhibits a fast capacity decay only after 100 cycles at 1.0 C (**black**). To reach a high energy density and fast charge/discharge of the battery, a high active material loading and a high rate are required. The battery with a high loading of 4.4 mg/cm<sup>2</sup> displays initial charge capacities of ~1941 mAh/g at 0.2 C (**pink**), 1571 mAh/g at 0.5 C (**gray**) and 1161 mAh/g at 1.0 C (**yellow**) (**Figure 3.12 b**). After 400 cycles, the capacities up to 1660, 1328 and 1073 mAh/g with a CE of 99.4 % are still retained, enabling an excellent cycling capability.

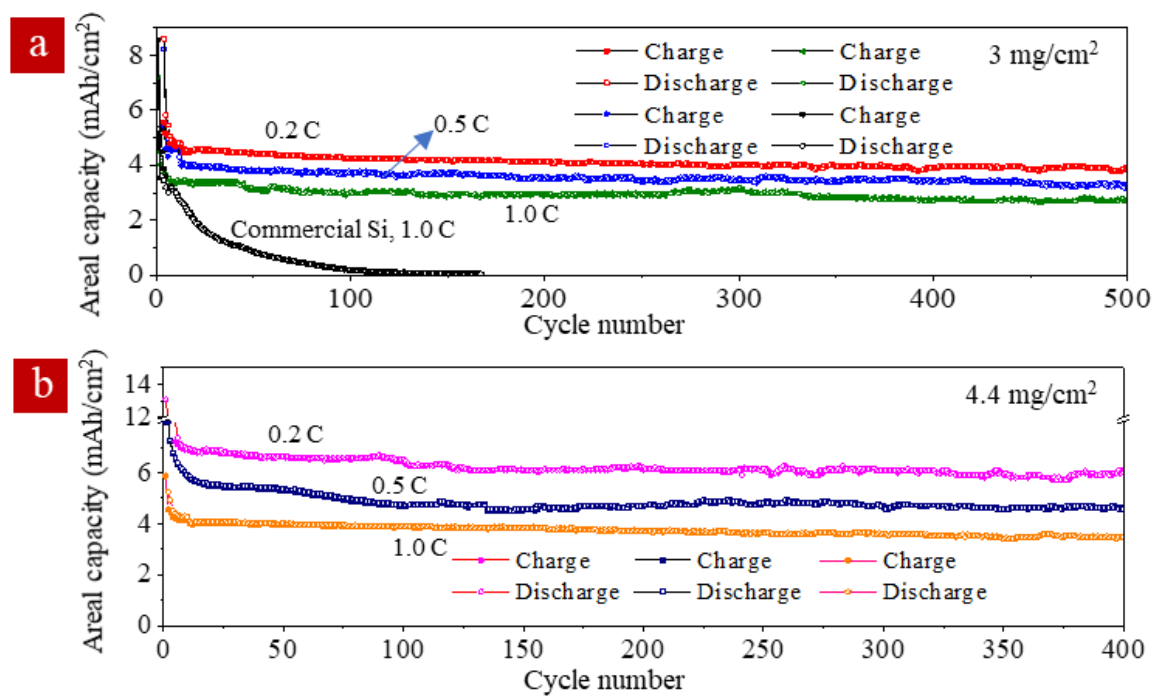


**Figure 3.13** Areal capacity vs cycle number of the battery with the active material loading of 3 mg/cm<sup>2</sup> (a) and 4.4 mg/cm<sup>2</sup> (b), respectively (Copyright © 2019, American Chemical Society).<sup>155</sup>

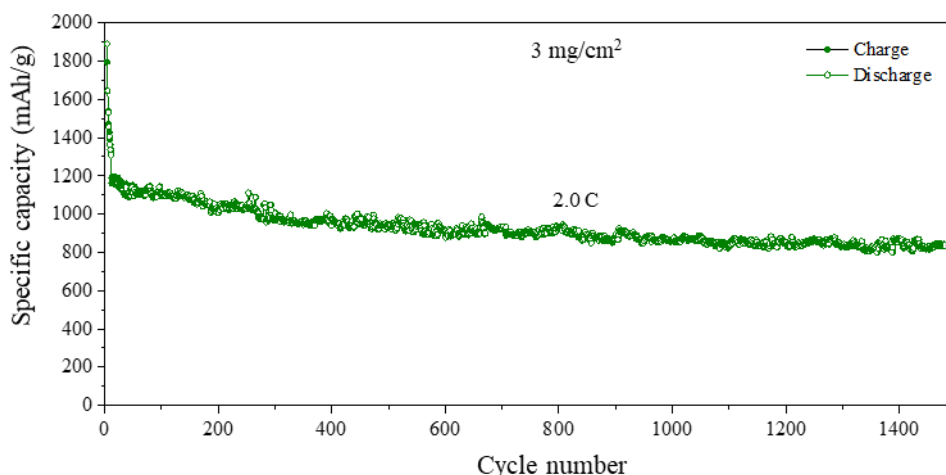


**Figure 3.15** Cycling performance of the battery with the  $\mu$ -Si cage as anode with a loading of 3  $\text{mg}/\text{cm}^2$  at 2.0 C. The specific capacity was calculated based on the pure silicon inside  $\mu$ -Si cage (Copyright © 2019, American Chemical Society).<sup>155</sup>

The correlated areal capacities of as high as 4.3  $\text{mAh}/\text{cm}^2$  and 6.4  $\text{mAh}/\text{cm}^2$  after long cycles with 3 and 4.4  $\text{mg}/\text{cm}^2$  were obtained (**Figure 3.13**), which displays promising potential in making large energy-density batteries. Meanwhile, the battery under the higher 2.0 C shows capacity retention at 868  $\text{mAh}/\text{g}$  after ultra-long 1500 cycles (**Figure 3.14**), indicating a largely improved rate performance.

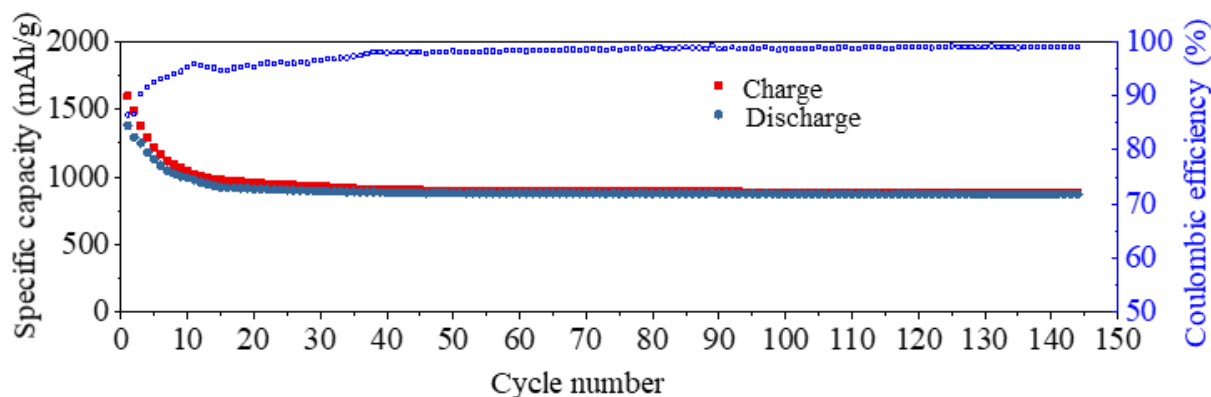


**Figure 3.14** Cycling performance of  $\mu$ -Si cage in a NMC 622/ $\mu$ -Si cage full cell at 0.2 C (the loading of  $\mu$ -Si cage and NMC 622 are 0.6  $\text{mg}/\text{cm}^2$  and 11  $\text{mg}/\text{cm}^2$ , respectively) (Copyright © 2019, American Chemical Society).<sup>155</sup>

The full cell battery (total capacity: 1.06 mAh) paired with  $\text{LiNi}_{0.6}\text{Mn}_{0.2}\text{Co}_{0.2}\text{O}_2$  (NMC622) was checked at 0.2 C (**Figure 3.15**). The battery with a negative/position (N/P) ratio of  $\sim 0.72$  displays a high charge/discharge capacity of  $\sim 900$  mAh/g along with a CE of 98.5% after about 150 cycles.

### 3.4 Characterization after cycling

Compared to pure nano-Si anode, the  $\mu$ -Si cage shows better capacity retention even with higher mass loading/rate. This is mainly due to the large pore volume which allows volume change of silicon during charge/discharge. Meanwhile, the micro-sized cage consists of interconnected silicon particles, which is beneficial in fast ion transportation (**Figure 3.16**). If we do not consider the volume mitigation due to the alloying process, according to the density of Al ( $2.7 \text{ g/cm}^3$ ) and Si ( $2.3 \text{ g/cm}^3$ ) and the mass ratio, the Al occupies a 570% volume, which provides enough space

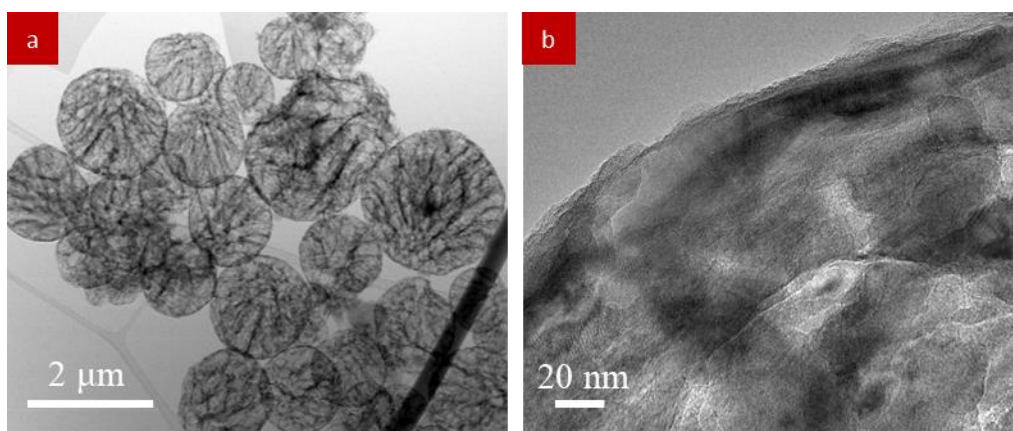


**Figure 3.16** Low-mag (a) and high-mag (b) TEM images of the  $\mu$ -Si cage (Copyright © 2019, American Chemical Society).<sup>155</sup>

to accommodate almost 300% volume change of Si during the cycling. Also, the volume contributed from the space over 100 nm inside the cage (not measured by the BET) provides additional accommodation even with a reduced Al initial volume. The silicon skeleton has a strong mechanical strength that maintains the tree-like framework even suffering drastic morphology deformation. As seen from the morphology observation after cycling in **Figure 3.17**, the overall framework of the  $\mu$ -Si cage was still remained after 20 cycles. The additional spaces also expand the channel for electrolyte and improve the contact with active silicon, thus to enhance the charge transfer kinetics on the solid-liquid interface.<sup>158</sup> In parallel, the mesoporous, conductive PPy layer

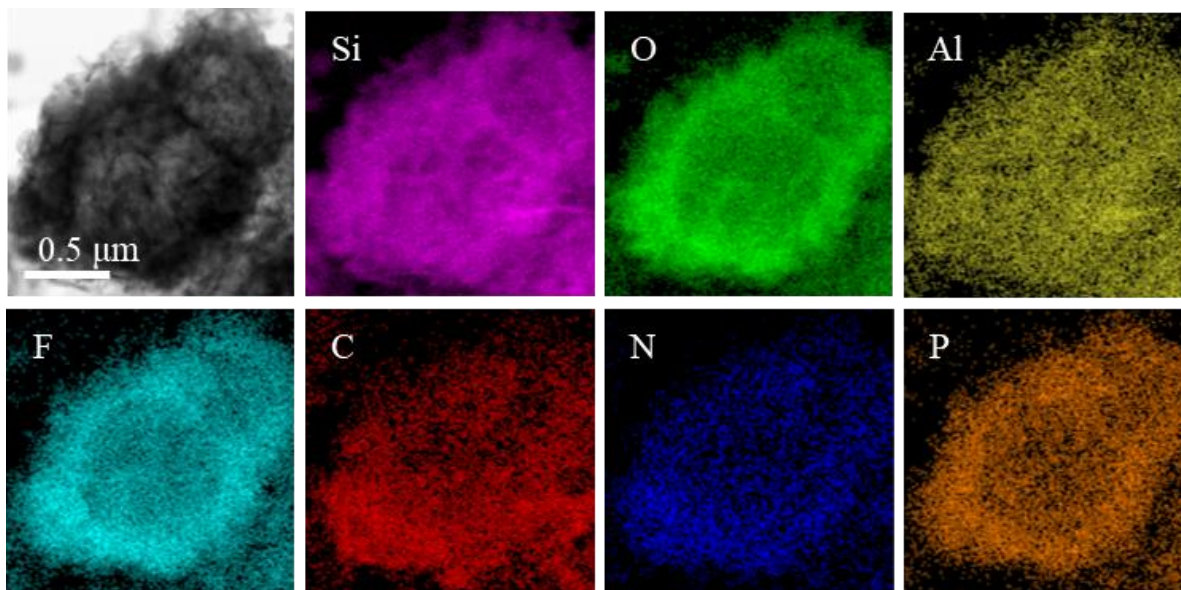


**Figure 3.17** Elemental mapping of the  $\mu$ -Si cage after 20 cycle at 0.5 C. Cycling performance of the battery using  $\mu$ -Si cage as anode with different loadings (Copyright © 2019, American Chemical Society).<sup>155</sup>

encapsulates the whole silicon skeleton to further avoid any loss while also serves as an efficiency gateway for  $\text{Li}^+/\text{e}^-$  transport. Further, the minimum amount of PPy will not introduce additional electrode volume and impurity, leading to an as-received density of  $\sim 950.2 \text{ mg/cm}^3$  (**Figure 3.18**). As shown in **Figure 3.19** and **Table 3.1**, about 5 times higher tapped density of the  $\mu$ -Si cage

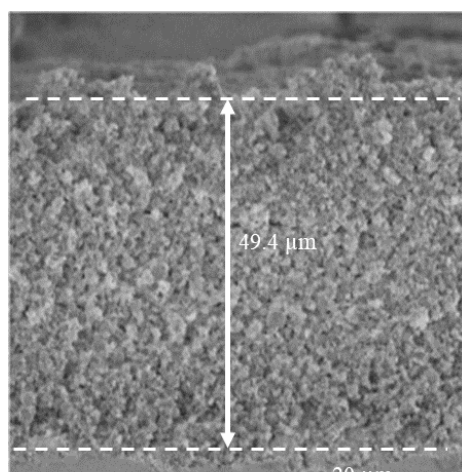


**Figure 3.18** Cross-section SEM image of  $\mu$ -Si cage coating (the loading is  $4.7 \text{ mg/cm}^2$  with an as-received density of  $950.2 \text{ mg/cm}^3$ ) (Copyright © 2019, American Chemical Society).<sup>155</sup>

sample than 30nm Si nanoparticles was achieved. In addition, the packing density of the  $\mu$ -Si cage pellet up to  $1.32 \text{ g/cm}^3$  was obtained (**Figure 3.19 b**),<sup>159</sup> which indicates promising potential in making high energy-density batteries. The intermediate  $\text{SiO}_2$  layer was created as a template to introduce meso-pores for the PPy layer. Regarding to the Al residuals, we found most Al was removed. We prepared the Al-Si composite with 20-70% Al residuals *via* insufficient etching. It was found the battery capacity with  $\sim 70\%$  Al residuals decreased to  $\sim 30\%$  of initial capacity in a few cycles even with a flat feature plateau of Al. Thus, in our experiments, the high capacity retention implies the trace amount of Al is negligible in term of the electrochemical performance.

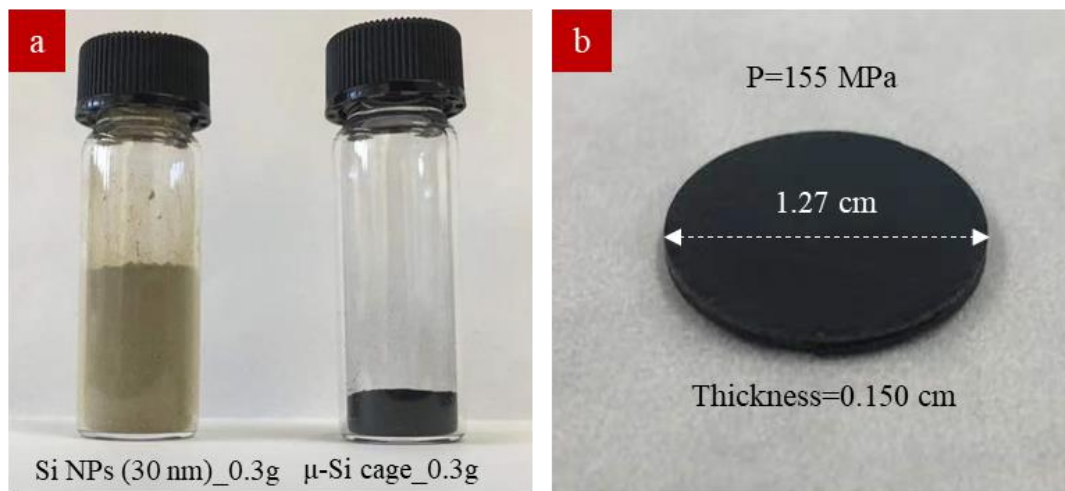


**Figure 3.19** (a) Volume comparison with 0.3g sample. (b) Produced pellet under the pressure of 155 Mpa displays a density of  $1.32 \text{ g/cm}^3$  (Copyright © 2019, American Chemical Society).<sup>155</sup>

**Table 3-1** Tapped density comparison of  $\mu$ -Si and Si nanoparticles.

Samples	Tapped density ( $\text{g/cm}^3$ )
$\mu$ -Si cage	0.59
Si nanoparticles (30nm)	0.12

### 3.5 Conclusions

To summarize, we developed a scalable production of  $\mu$ -Si cage that is composed of micro-sized silicon and a protective PPy polymer layer. The sufficient space after removing Al from the industry available AlSi alloy precursor greatly accommodates the silicon expansion/shrinkage upon charging/discharging, which results in an improved capacity retention upon long cycling. Particularly the mesoporous structure, the strong skeleton base and better polymer conductivity ensure fast  $\text{Li}^+/\text{e}^-$  transfer kinetics on the interface, leading to a high charge/discharge rate. A battery with the silicon loading of as high as  $4.4 \text{ mg/cm}^2$  was successfully obtained, which showed a specific capacity over  $1660 \text{ mAh/g}$  and an areal capacity over  $6.4 \text{ mAh/cm}^2$  after 400 cycles. The improved battery performance with high silicon loadings opens an avenue in mass production of high gravimetric and high volumetric energy-density batteries.

## 3.6 Methods/Experimental

### 3.6.1 Material synthesis

The  $\mu$ -Si cage sample was synthesized using commercial AlSi alloy micro-spheres (SkySpring Nanomaterials, Inc.) as precursor *via* a modified sol-gel process.<sup>160, 161</sup> In a typical experiment, the AlSi particles were received by centrifugation after immersing into a 4 g/L polyvinylpyrrolidone (PVP, Alfa Aesar) solution for 24 hours at room temperature. Subsequently the sample was uniformly dispersed in a mixture solution of 0.1 g cetyltrimethylammonium bromide (CTAB, Sigma-Aldrich), 30 mL deionized water (DI), 50 mL ethanol, and 0.5 mL ammonia solution (28-30%, Sigma-Aldrich) under ultrasound agitation for 30 min. Then 500  $\mu$ L tetraethoxysilane (TEOS, Sigma-Aldrich) was gradually added into the above solution upon magnetic stirring. After 5 hours reaction, the sample was collected *via* 6000 rpm centrifugation and rinsed with ethanol for three times.

The obtained AlSi alloy@*m*-SiO<sub>2</sub> intermediate product was dispersed in a mixture solution of 30 mL ethanol and 300  $\mu$ L pyrrole. Then 1.5 M FeCl<sub>3</sub> (MP Biomedicals, LLC) was added in a dropwise way under nitrogen flow inside a 0 °C ice bath. After stirring for 24 hours, the sample was recollected *via* centrifugation, washed in sequence with DI water and ethanol several times, and finally dried in a vacuum oven. The dried sample was treated with 6 M hydrochloric acid (VWR Analytical) for 12 hours. An additional hydrofluoric acid (2%, Sigma-Aldrich) treatment for 2 hours was done to remove the SiO<sub>2</sub> and Al/Al<sub>2</sub>O<sub>3</sub> residues. The final  $\mu$ -Si cage sample was received after the further rinsing and dry process.

### 3.6.2 Electrochemical measurements

**Battery fabrication:** The stainless-steel coin cell (CR2032, Xingye Co., Ltd.) was assembled inside an argon-filled glove box with the synthesized material as anode and lithium foil (1 mm thickness) as counter electrode at room temperature. In all tests 1.0 M LiPF<sub>6</sub> dissolved in ethylene carbonate (EC) and diethyl carbonate (DEC) (1:1 volume ratio) with 5 wt% vinylene carbonate (VC, Sigma-Aldrich) as electrolyte (LP47, BASF Corp.) and Celgard 2400 microporous polyethylene film as separator were used. For the anode preparation, the electrode slurry was fabricated by mixing 80 wt% active materials ( $\mu$ -Si cage), 10 wt% poly-vinylidene fluoride (average Mn = 71 000, Sigma-Aldrich), and 10 wt% SuperP (Super C65, Timcal) in N-Methyl-2-pyrrolidone (NMP, Honeywell) solvent. The as-received slurry was coated on Cu foil and then dried at 80 °C overnight in a vacuum oven (Sheldon Manufacturing, Inc). After dry, the electrode was pressed under 6–10 MPa by a benchtop hydraulic press (Northern Tool+ Equipment). The dense electrode was then punched into the circle disc using a disc cutter (MSK-T-07, MTI Corp.). For full cell batteries, the  $\mu$ -Si cage with 0.6 mg/cm<sup>2</sup> loading was used as anode material and NMC622 with a loading of 11 mg/cm<sup>2</sup> was used as cathode material. The charge and discharge rates were calculated based on the theoretical capacity of silicon. The Coulombic efficiency was calculated as  $(C_{\text{charge}}/C_{\text{discharge}}) \times 100\%$ , where  $C_{\text{discharge}}$  and  $C_{\text{charge}}$  are the capacities of the anode for lithium insertion and extraction, respectively.

**Electrochemical measurements:** The electrochemical property of the coin cells was examined by galvanostatic cycling. The sealed cells were rested for 24 h and were then charged/discharged using a battery tester system (LANDT 2001CT, Landt Instruments, Inc.). All the coin cells were subjected to an initial activation at 0.1 C for three cycles. The following cycling tests were operated in a voltage window of 0.02-2.0 V under various rates from 0.2 to 2.0 C, respectively. The cyclic

voltammetry and electrochemical impedance spectroscopy were measured using a Gamry Reference 600+ potentiostat with a scan rate of 0.05 mV/s at room temperature. For the full cell battery test, the  $\mu$ -Si cage electrode was prelithiated with Li metal to reach a capacity of about 1584 mAh/g at 0.1 C. Then the full cell was formed using the prelithiated  $\mu$ -Si cage as anode and NMC622 as cathode. All the full cells were activated at 0.1C for a few cycles before cycling.

### 3.6.3 Sample characterizations

XRD pattern was obtained with a Bruker D8 Discover X-ray Diffractometer using Ni filtered Cu  $K\alpha$  radiation. The applied current and voltage were 40 mA and 40 kV, respectively. SEM images were collected on a Hitachi S4800 ultrahigh resolution field emission scanning electron microscope (FESEM). Atomic resolution TEM images and EDS element mappings were operated on a JEOL JEM-ARM200CF 200 kV STEM/TEM, which is affiliated with a probe aberration corrected high-angle annular bright field/dark-field scanning transmission electron microscopy (STEM) mode imaging. The EDS element mapping was checked under 200 kV accelerating voltage with an image resolution of less than 0.08 nm and energy resolution of 0.35 eV. The surface area and pore volume of the samples were calculated by the Brunauer-Emmett-Teller (BET) method *via* the measurement of N<sub>2</sub> sorption/desorption isotherms using a Micromeritics ASAP 2020 system at 77 K. Thermogravimetric analysis of the samples was done using a thermal gravimetric analyzer (Shimadzu DTG-60AH) with a heating rate of 5 °C/min under N<sub>2</sub> flow of 50 mL/min. XPS measurements were operated by Thermo Scientific ESCALAB 250Xi which is equipped with an electron flood gun and a scanning ion gun. The spectra were collected using an ultrahigh vacuum (UHV) apparatus with a base pressure below  $1 \times 10^{-10}$  Pa. The sample was irradiated using an Al  $K\alpha$  line (a photon energy of 1486.6 eV) of a non-monochromatic X-ray source. The emitted electrons were detected using a hemispherical analyzer under an angle of 45°

to the surface normal. All XPS spectra were fitted with Gaussian–Lorentzian functions and a Shirley-type background and plotted as a function of the binding energy with respect to the Fermi level. All the data were calibrated using the C 1s peak at 284.8 eV. Diffused FTIR was performed on a Shimadzu IRTracer-100 FTIR spectrometer featured with the SN ratio of 0.25 cm<sup>-1</sup> resolution and high-speed scanning capable of 20 spectra/s. The as-received sample density was calculated upon the electrode made by 98 wt% active material and 2 wt% poly-vinylidene fluoride as binder. The tapped density test was to demonstrate the density of Si-cage after coating on Cu foil, which is proportional to the final battery volumetric energy density. The tapped density was measured using an auto-tap density tester (Wincom Company, HY-100A) upon the ASTM 4781-03 standard. The sample was first heated to 400 °C for 3h under argon. Then the sample was weighed and carefully transferred into a 100 ml plastic cylinder. The volume was recorded before and after 1000 taps. The tapped volume of sample was calculated based on the ratio of mass and tapped volume. The denser packing density of pellet sample was also measured<sup>34</sup>. During the test, the pellet was produced by pressing 0.25 g  $\mu$ -Si cage sample in a stainless-steel model with a diameter of 1.27 cm using hydraulic press (Carver, Model 3393) under the pressure of 155 MPa. After 1 min, the pellet was removed from the model for density measurement.

# CHAPTER 4 Other Si-based Anode Materials

## 4.1 Introduction

Except nanostructured Si and micro-sized Si composite, Si alloy also provides another possibility to create Si composite with improved electrochemical performance. For example, graphite, graphene, porous carbon, and some other carbon-based materials are always the first choice as loading material to form composite with Si due to their good conductivity and higher specific surface area.

Recently, the 2D transition-metal carbides, MXene, are attracting great interest due to their outstanding electrical, mechanical and electrochemical properties,<sup>162</sup> which displayed great potential in the area of LIBs and catalysis. The good conductivity and high structure stability make  $\text{Ti}_3\text{C}_2$  MXene a good candidate as loading matrix material to form composite with active material with large volume change upon lithiation/delithiation, like Si,<sup>163</sup> Sn,<sup>164</sup> S,<sup>165</sup> and so on. In our previous study, a composite of amorphous  $\text{GeO}_x$  coated  $\text{Ti}_3\text{C}_2$  MXene ( $\text{GeO}_x@\text{MXene}$ ) synthesized through a facile wet chemical method as anode for LIBs. The unique layered 3D structure of  $\text{Ti}_3\text{C}_2$  can provide stable physical support for the Ge nanoparticles, efficiently shorten

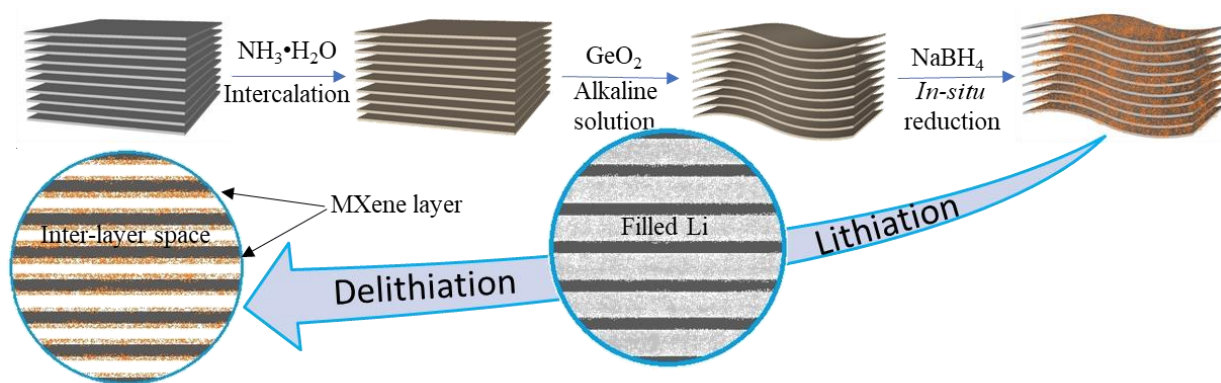


**Figure 4.1** Schematic illustration of the  $\text{GeO}_x@\text{MXene}$ .<sup>166</sup>

the  $\text{Li}^+$  ions diffusion distance and accommodate the volume expansion during charge/discharge

process. All these unique features contribute to the outstanding electrochemical performance of the  $\text{GeO}_x@MXene$  composite (**Figure 4.2**).<sup>166</sup>

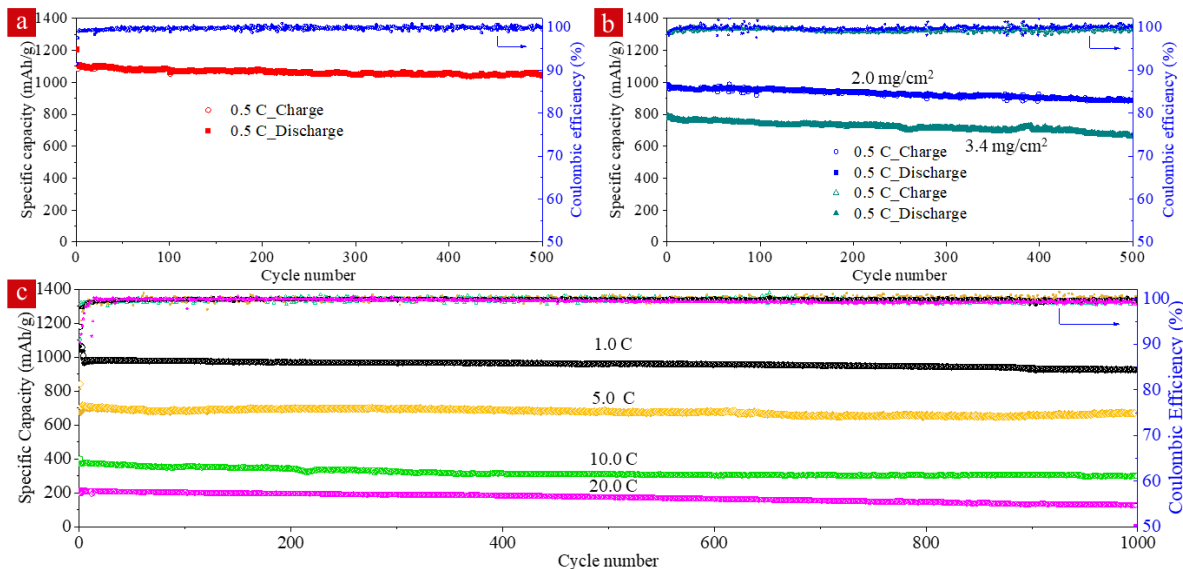


**Figure 4.2** Cycling performance of the battery with  $\text{GeO}_x@MXene$  as anode under (a) 0.5 C and a loading of  $\text{GeO}_x$  of 1.0 mg/cm<sup>2</sup>, (b) 0.5 C and  $\text{GeO}_x$  loadings of 2.0, 3.4 mg/cm<sup>2</sup>, and (c) 1.0 C, 5.0 C, 10.0 C and 20.0 C (1.0 mg/cm<sup>2</sup>), respectively.<sup>166</sup>

Inspired from the strategy of  $\text{GeO}_x@MXene$ , different composite materials were developed. It has been proved that SiGe alloy can significantly improve the rate performance and cycling stability of Si.<sup>167</sup> The improved electrochemical performance can be attributed to the improved structure stability due to the enhanced yield strength.<sup>168</sup> However, specific structure design is also needed to accommodate the volume change upon lithiation/delithiation process. At the same time, the conductivity needs further improvement.

Here, we propose to combine the advantages of MXene and SiGe alloy. In the formed composite, MXene with autoadjustable layer space provides high structural stability, which can effectively accommodate the volume change during cycling. The conductivity of the SiGe alloy can also be improved after combining with MXene. The formation of SiGe alloy will increase the structural

stability of the individual particles during cycling. All these features are beneficial to the enhanced electrochemical stability.

## 4.2 Design strategy and preparation

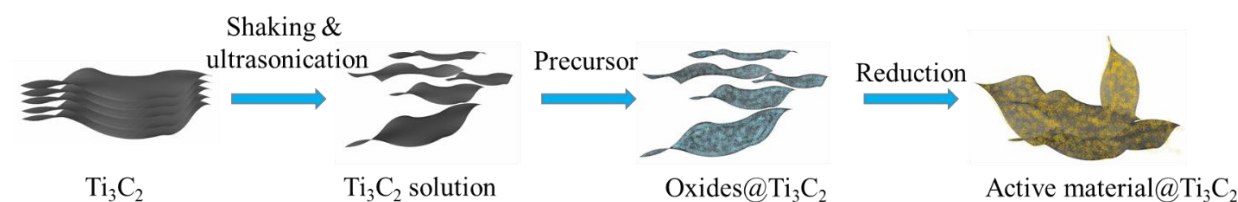


**Figure 4.3** Schematic illustration of the synthesis process of SiGe@MXene.

**Figure 4.3** displays the schematic illustration of the composite of SiGe@MXene. Typically, Ti<sub>3</sub>C<sub>2</sub> MXene was obtained from Ti<sub>3</sub>AlC<sub>2</sub> MAX after HF etching. The space between MXene layers can be further expanded through reaction with NH<sub>3</sub>•H<sub>2</sub>O. After shaking and sonication, MXene with a few layers can be obtained. To form uniform coating on the surface, PVP was used pretreat the surface of MXene in solution. The formation of SiGe alloy can be performed through reduction the corresponding oxides. First, the MXene was coated with SiGe oxide through a reaction with TEOS and germanium ethoxide with appropriate ratio. After reaction at room temperature for 5 h, the SiGe oxide@MXene composite was obtained through vacuum filtration and washing. The collected powders were further dried at 80 °C for 12 h before the reduction process. The reduction of the SiGe oxide was performed through a low temperature method, using AlCl<sub>3</sub> and LiAlH<sub>4</sub>. This reduction can happen at ~250 °C. The low temperature is expected to avoid the growth of SiGe particles to aggregated particles, which will affect the electrochemical performance.

To compare the performance difference, Si@MXene and SiGe@RGO (reduced graphene oxide) were also prepared using same method as SiGe@MXene.

## 4.3 Characterization

### 4.3.1 Morphology characterization

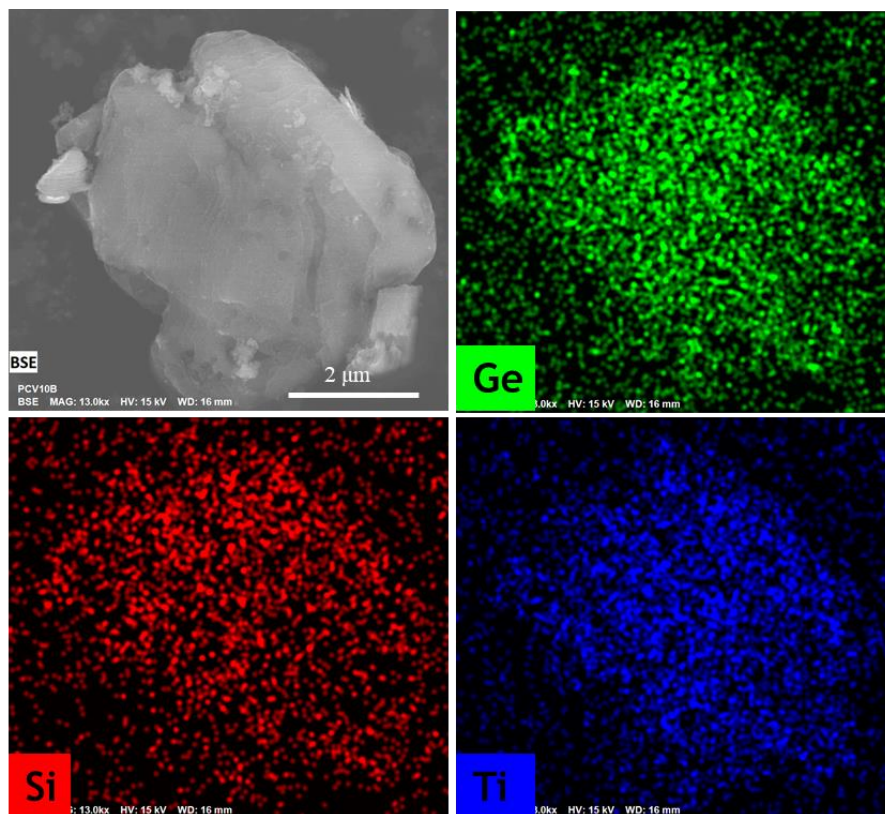


**Figure 4.4** SEM image of SiGe@MXene with corresponding EDS element mapping of Ge, Si, and Ti.

The morphology of the obtained SiGe@MXene was checked using SEM. The SEM image and corresponding EDS element mapping of Ge, Si, and Ti are shown in **Figure 4.4**. It can be found that the mapping of Ge and Si perfectly match the mapping of Ti, the main composition of  $\text{Ti}_3\text{C}_2$  MXene, indicating that the uniform coating of SiGe alloy formed on the surface of MXene layers. The uniform distribution of SiGe particles can be attributed to the presence of abundant functional groups on the surface of MXene layer, such as -F, and -OH groups, which provide numerous sites for the growth of the SiGe oxides.

### 4.3.2 XRD characterization

The crystal structure of the obtained samples was confirmed using XRD, as shown in **Figure 4.5**. After comparison with Si@MXene, the (111) and (311) peak of Ge were found on the XRD pattern of SiGe@MXene, indicating the formation of SiGe alloy in the composite.

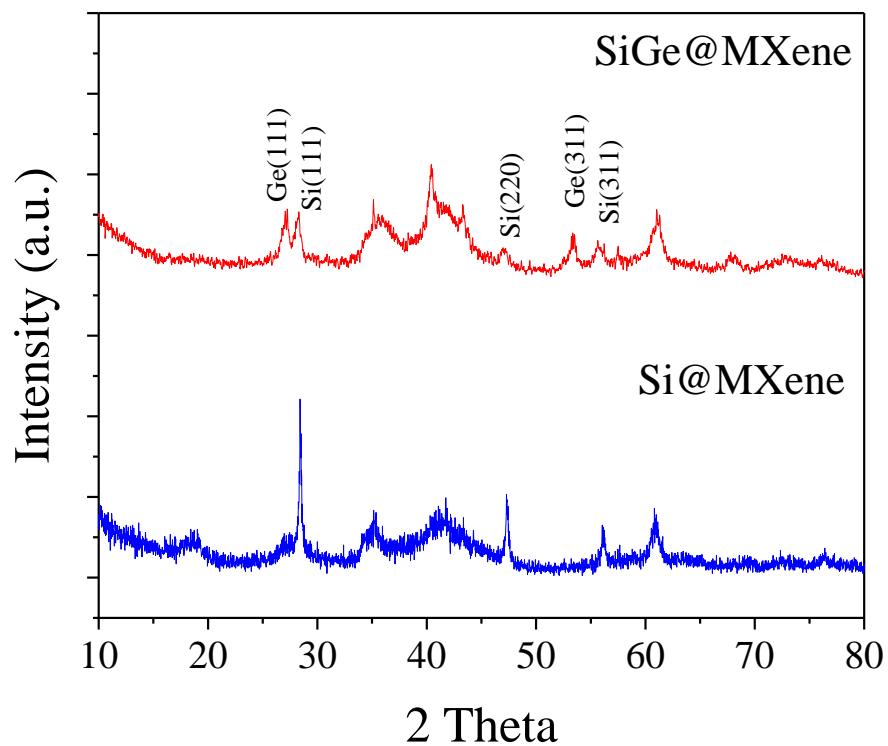


**Figure 4.5** XRD patterns of the SiGe@MXene and Si@MXene.

## 4.4 Electrochemical performance

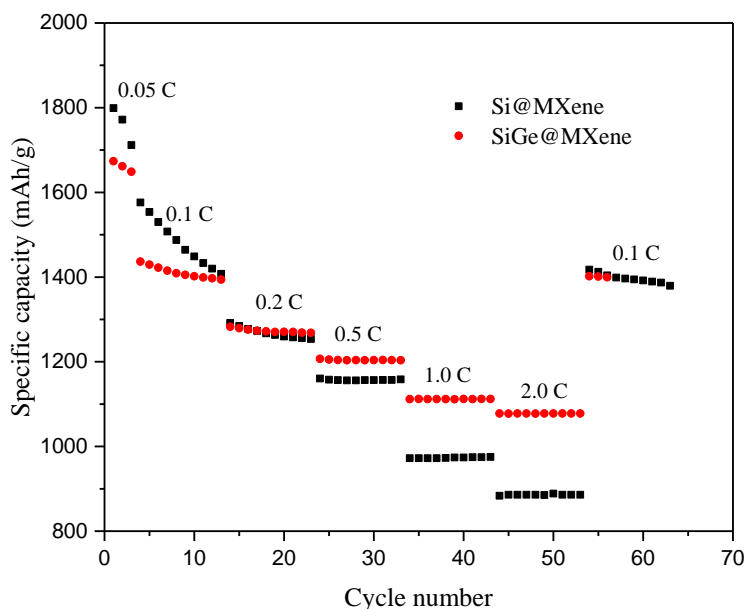


**Figure 4.6** Specific discharge capacity evolution of Si@MXene and SiGe@MXene at different rates from 0.1 to 2.0 C. The batteries were cycled three times at 0.05 C for activation.

The battery with the obtained SiGe@MXene and Si@MXene anodes were cycled at current densities ranging from 0.1 C to 2.0 C (**Figure 4.6**) to characterize the rate performance. At respective current densities of 0.1 C, 0.2 C, 0.5 C, 1.0 C, and 2.0 C, Si@MXene exhibits reversible charge capacity of 1557.8, 1291.4, 1160.3, 972.2, and 883.5 mAh/g, respectively. After cycled at each current density for 10 cycles, when the current density returned to 0.1 C, the Si@MXene maintains the capacity of 1417.5 mAh/g, which is 91.0% of its initial capacity at 0.1 C. For comparison, the SiGe@MXene shows charge capacity of 1436.6, 1282.5, 1206.9, 1111.7, and 1077.9 mAh/g at 0.1 C, 0.2 C, 0.5 C, 1.0 C, and 2.0 C, respectively. It can maintain the capacity of 1402.0 mAh/g which is 97.6% of its initial capacity, when the current was changed back to 0.1 C. The observed excellent rate capability of the SiGe@MXene can be attributed to the improved

structural stability of SiGe on the surface of MXene and the intrinsic high electronic and ionic conductivity of MXene.

The cycling performance was shown in **Figure 4.7**. Before cycling, the batteries were cycled five

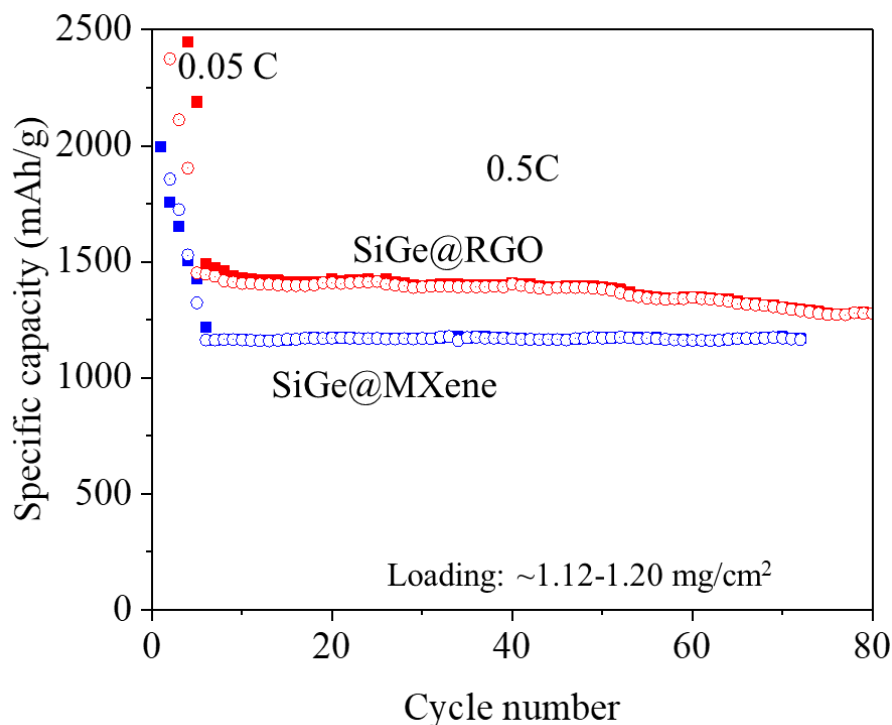


**Figure 4.7** Cycling performance of Si@MXene and SiGe@MXene at 0.5 C.

times at 0.05 C for activation. The SiGe@MXene delivered an initial capacity of 1217.3 mAh/g at 0.5 C, and capacity of 1176.0 after 70 cycle with capacity retention of 96.6%. For contrast, the SiGe@RGO delivered an initial capacity of 1491.4 mAh/g and 1305.7 mAh/g after 70 cycles at 0.5 C. The capacity retention is calculated to be 87.5%. It can be found that RGO is beneficial to improve the specific capacity of SiGe alloy, which can be attributed to the large specific surface area. However, the cycling stability is not as expected. SiGe@MXene shows much better cycling stability, which can maintain more than 96.6% of its initial capacity after 70 cycles, as a result of the high structural stability of the 3d layered structure with auto adjustable layer space.<sup>166</sup>

## 4.5 Conclusion

In this study, a rationally designed SiGe@MXene composite was synthesized through a low temperature reduction method. The expanded  $\text{Ti}_3\text{C}_2$  MXene with autoadjustable layer space provides sufficient space to accommodate the volume expansion of SiGe alloy particles during cycling. At the same time,  $\text{Ti}_3\text{C}_2$  MXene also improves the conductivity and reduces the  $\text{Li}^+$  diffusion distance to ensure fast  $\text{Li}^+/\text{e}^-$  transfer kinetics and provide stable mechanical support to the composite, which enhance both the rate and cycling performance. All these unique features make the obtained composite with large active surface area, favorable electronic conductivity, fast  $\text{Li}^+/\text{e}^-$  transfer kinetics, flexible layer spacing, and excellent mechanical stability, exhibit outstanding high-rate performance and cycling stability. Compared with RGO, the MXene also displayed better cycling stability due to its stable 3d structure. Compared with other synthesis method of Si-based composite, the low temperature reduction process avoids the aggregation of the particles at high temperature, which is beneficial to the improvement of cycling stability. Additionally, the facile synthesis method makes it a more promising candidate for high performance anode with great potential to be scaled up.

## 4.4 Experimental details

**Synthesis of Ti<sub>3</sub>C<sub>2</sub> MXene:** Ti<sub>3</sub>C<sub>2</sub> MXene was synthesized through etching of Ti<sub>3</sub>AlC<sub>2</sub> MAX (200 mesh, Forsman, China) by HF. Typically, 1 g of Ti<sub>3</sub>AlC<sub>2</sub> was slowly added into 10 ml Hydrofluoric acid solution (48-52%, Sigma-Aldrich) in a Teflon container under magnetic stirring over 30 min. After stirring for 1 h at room temperature, the container was moved to a water bath and kept stirring at 60 °C. The reaction time was controlled to be 24 h. After centrifuging and washing using DI water until the pH reach ~6, the Ti<sub>3</sub>C<sub>2</sub> sediment was collected via vacuum-assisted filtration using a polyvinyl difluoride (PVDF) filter membrane with pore size of 0.22 μm and dried in vacuum oven at 80 °C for 24 h.

**Synthesis of SiGe@MXene:** Before the synthesis of SiGe oxide, the obtained Ti<sub>3</sub>C<sub>2</sub> MXene was intercalated with NH<sub>3</sub>•H<sub>2</sub>O. Firstly, certain amount of Ti<sub>3</sub>C<sub>2</sub> was dispersed in 10 ml ammonia solution (20%, Acros Organics) and kept stirring for 3 h. After centrifuge, the sediment was collected and redispersed in 50 ml DI water and sonicated for 10 h under the protection of Ar. TEOS and germanium ethoxide with desired ratio were mixed together in ethanol. 0.01 g polyvinylpyrrolidone (PVP, G-biosciences) and MXene were dissolved in 100 ml of solution containing ethanol and DI water with 800 μL of NH<sub>3</sub>•H<sub>2</sub>O. The mixture of TEOS and germanium ethoxide was slowly dropped into the 100 ml of solution containing ethanol and DI water under stirring. After reaction at room temperature for 5 h, the samples were collected after centrifugation and washing using ethanol and DI water. After drying, the obtained powders were mixed with anhydrous AlCl<sub>3</sub> and LiAlH<sub>4</sub> in glovebox. Then the mixture was sealed in a stainless-steel reaction and heated at 250 °C for 10 h. After reaction, the samples were immersed in 0.05 M of HCl solution

under stirring to remove the residual. After washing with DI water and ethanol, the samples were dried at 80 °C for 12 h under vacuum before making slurry.

**Electrochemical measurement:** To prepare the working electrodes, active material, conductive carbon (SuperP) and PVDF with the ratio of 80:10:10 were mixed in N-methyl-2-pyrrolidone (NMP) to form the slurry. After being coated on carbon coated Cu foil, the electrode was dried in vacuum oven at 60 °C for 12h. Before being punched into the circle disc using a disc cutter (MSK-T-07, MTI Corp.), the electrode was pressed under 6–10 MPa using a benchtop hydraulic press (Northern Tool+ Equipment). The stainless-steel coin cells (CR2032, Xingye Co., Ltd.) were assembled at room temperature in an argon-filled glovebox using the obtained electrode, polyethylene (Celgard 2400), and lithium foil (MTI Corp.) as working electrode, separator and counter electrodes, respectively. The electrolyte used was 1 M LiPF<sub>6</sub> in ethylene carbonate (EC) and diethyl carbonate (DEC) (1:1 volume ratio) (LP47, BASF Corp.) with 10 % FEC and 2 % vinylene carbonate (VC) as additive. The assembled coin cells were tested by galvanostatic cycling using a battery tester system (LANDT 2001CT, Landt Instruments, Inc.) after resting at room temperature for 4 h.

**Sample characterization:** The morphologies and nanostructures of the SiGe@MXene composite were characterized using Hitachi S4800 ultrahigh resolution field emission scanning electron microscopy (FESEM) with EDS mapping.

## CHAPTER 5 Summary and outlooks

To build LIBs with improved energy density, Ni-rich NMC and Si-based composite are selected as the electrode material. To improve the performance, the cathode and anode materials were optimized, respectively.

For the Ni-rich cathode, modification on both primary and secondary particles were applied on NMC811, where the concentration gradient on both primary and secondary particles was built through incorporation of Ni-MOF during the coprecipitation process. On the level of the secondary particles, the reduced Ni content in the out shell can enhance the stability during cycling when contact with electrolyte. And the high Ni content in the bulk ensures the high specific capacity. On the level of primary particles, the reduced Ni oxidation state leads to the formation of cation mixing layer on the surface, which can significantly reduce the  $\text{Li}^+/\text{Ni}^{2+}$  cation mixing in the bulk during calcination process, through blocking the Li diffusion pathway from the bulk to the surface. At the same time, it can improve the cycling stability through inhibiting the generation of internal cracks through resisting the internal strain and suppressing phase transition within primary particles during cycling process. All these features make the prepared D-NMC811 deliver high thermal stability, favorable specific capacity, and excellent cycling stability, showing high potential for high-performance LIBs targeting broad application area. The building of gradient on both primary and secondary particles also provides a promising design route for the optimization of Ni-rich cathode materials.

For the anode part, two strategies were applied for the development of Si-based anode material. The  $\mu$ -Si cage composed of micro-sized Si and a protective PPy polymer layer showed largely improved electrochemical performance. Under the configuration of the  $\mu$ -Si cage, the skeleton

structure under the protection of PPy can provide sufficient space to accommodate the volume change upon lithiation/delithiation. The presence of the mesoporous structure, the strong skeleton base and better polymer conductivity ensure fast  $\text{Li}^+/\text{e}^-$  transfer kinetics on the interface, leading to a high charge/discharge rate. The micro-sized Si with high tapped density is beneficial to reach a high loading and high areal capacity, which is favorable during the practical application. The improved battery performance with high silicon loadings opens an avenue in mass production of high gravimetric and high volumetric energy-density batteries.

The developed SiGe@MXene anode also showed improved electrochemical performance including rate and cycling stability. The MXene with autoadjustable layer space can effectively accommodate the volume change of the Si-based particles. At the same time,  $\text{Ti}_3\text{C}_2$  MXene also improves the conductivity and reduces the  $\text{Li}^+$  diffusion distance to ensure fast  $\text{Li}^+/\text{e}^-$  transfer kinetics and provide stable mechanical support to the composite, which enhance both the rate and cycling performance. Through alloying, the structural stability of SiGe particles is increased. Moreover, the low temperature reduction process avoids the aggregation of the particles at high temperature, which is beneficial to the formation of uniform distribution and improvement of cycling stability. Additionally, the facile synthesis method makes it a more promising candidate for high performance anode with great potential to be scaled up.

Calculated based on the pouch cells made in our lab, the energy density is estimated to be improved by 18-20% when the D-NMC811 is coupled with the  $\mu$ -Si cage, which shows great potential for practical application.

However, this dissertation is only focused on the aspects of materials. There are still many other factors affecting the design and improvement of LIBs. For example, one obstacle affecting the application of Si-based anode material is the prelithiation technique.<sup>169</sup> Basically, the large active

area of Si leads to not only the high specific capacity, but also the low initial CE, which significantly affect the battery performance when coupled with cathode material. Fortunately, thousands of researchers are spending their effort in this area to promote the development of LIBs. We do believe that the LIBs are getting cheaper, stronger, and safer!

## REFERENCES

1. Zubi, G.; Dufo-Lopez, R.; Carvalho, M.; Pasaoglu, G., The lithium-ion battery: State of the art and future perspectives. *Renewable & Sustainable Energy Reviews* **2018**, *89*, 292-308.
2. Kraytsberg, A.; Ein-Eli, Y., Higher, Stronger, Better ... A Review of 5 Volt Cathode Materials for Advanced Lithium-Ion Batteries. *Advanced Energy Materials* **2012**, *2* (8), 922-939.
3. Li, M.; Lu, J.; Chen, Z. W.; Amine, K., 30 Years of Lithium-Ion Batteries. *Advanced Materials* **2018**, *30* (33).
4. (a) Laman, F. C.; Brandt, K., EFFECT OF DISCHARGE CURRENT ON CYCLE LIFE OF A RECHARGEABLE LITHIUM BATTERY. *Journal of Power Sources* **1988**, *24* (3), 195-206. (b) Godshall, N. A., I. D. Raistrick, and R. A. Huggins. Thermodynamic investigations of ternary lithium-transition metal-oxygen cathode materials. *Materials Research Bulletin* **1980**, *15* (5), 561-570.
5. Ohzuku, T.; Brodd, R. J., An overview of positive-electrode materials for advanced lithium-ion batteries. *Journal of Power Sources* **2007**, *174* (2), 449-456.
6. (a) Dey, A. N. Electrochemical alloying of lithium in organic electrolytes. *Journal of The Electrochemical Society* **1971**, *118* (10), 1547. (b) Besenhard, J. O. Cycling behaviour and corrosion of Li-Al electrodes in organic electrolytes. *Journal of Electroanalytical Chemistry and Interfacial Electrochemistry* **1978**, *94* (1), 77-81. (c) Murphy, D. W., F. J. Di Salvo, J. N. Carides, and J. V. Waszczak. Topochemical reactions of rutile related structures with lithium. *Materials Research Bulletin* **1978**, *13* (12), 1395-1402. (d) Yoshino, A., The Birth of the Lithium-Ion Battery. *Angewandte Chemie-International Edition* **2012**, *51* (24), 5798-5800.
7. Li, W. D.; Song, B. H.; Manthiram, A., High-voltage positive electrode materials for lithium-ion batteries. *Chemical Society Reviews* **2017**, *46* (10), 3006-3059.

8. Hannan, M. A.; Lipu, M. S. H.; Hussain, A.; Mohamed, A., A review of lithium-ion battery state of charge estimation and management system in electric vehicle applications: Challenges and recommendations. *Renewable & Sustainable Energy Reviews* **2017**, *78*, 834-854.
9. Cordoba-Arenas, A.; Onori, S.; Guezennec, Y.; Rizzoni, G., Capacity and power fade cycle-life model for plug-in hybrid electric vehicle lithium-ion battery cells containing blended spinel and layered-oxide positive electrodes. *Journal of Power Sources* **2015**, *278*, 473-483.
10. Cano, Z. P.; Banham, D.; Ye, S. Y.; Hintennach, A.; Lu, J.; Fowler, M.; Chen, Z. W., Batteries and fuel cells for emerging electric vehicle markets. *Nature Energy* **2018**, *3* (4), 279-289.
11. Han, X. B.; Ouyang, M. G.; Lu, L. G.; Li, J. Q., A comparative study of commercial lithium ion battery cycle life in electric vehicle: Capacity loss estimation. *Journal of Power Sources* **2014**, *268*, 658-669.
12. Zeng, X. Q.; Li, M.; Abd El-Hady, D.; Alshitari, W.; Al-Bogami, A. S.; Lu, J.; Amine, K., Commercialization of Lithium Battery Technologies for Electric Vehicles. *Advanced Energy Materials* **2019**, *9* (27).
13. House, R. A.; Jin, L. Y.; Maitra, U.; Tsuruta, K.; Somerville, J. W.; Forstermann, D. P.; Massel, F.; Duda, L.; Roberts, M. R.; Bruce, P. G., Lithium manganese oxyfluoride as a new cathode material exhibiting oxygen redox. *Energy & Environmental Science* **2018**, *11* (4), 926-932.
14. Placke, T.; Kloepsch, R.; Duhnen, S.; Winter, M., Lithium ion, lithium metal, and alternative rechargeable battery technologies: the odyssey for high energy density. *Journal of Solid State Electrochemistry* **2017**, *21* (7), 1939-1964.

15. Myung, S. T.; Maglia, F.; Park, K. J.; Yoon, C. S.; Lamp, P.; Kim, S. J.; Sun, Y. K., Nickel-Rich Layered Cathode Materials for Automotive Lithium-Ion Batteries: Achievements and Perspectives. *Acs Energy Letters* **2017**, *2* (1), 196-223.
16. Liu, W.; Oh, P.; Liu, X.; Lee, M. J.; Cho, W.; Chae, S.; Kim, Y.; Cho, J., Nickel-Rich Layered Lithium Transition-Metal Oxide for High-Energy Lithium-Ion Batteries. *Angewandte Chemie-International Edition* **2015**, *54* (15), 4440-4457.
17. Manthiram, A.; Song, B. H.; Li, W. D., A perspective on nickel-rich layered oxide cathodes for lithium-ion batteries. *Energy Storage Materials* **2017**, *6*, 125-139.
18. Thackeray, M. M.; Kang, S. H.; Johnson, C. S.; Vaughey, J. T.; Benedek, R.; Hackney, S. A., Li<sub>2</sub>MnO<sub>3</sub>-stabilized LiMO<sub>2</sub> (M = Mn, Ni, Co) electrodes for lithium-ion batteries. *Journal of Materials Chemistry* **2007**, *17* (30), 3112-3125.
19. Zheng, J. C.; Yang, Z.; He, Z. J.; Tong, H.; Yu, W. J.; Zhang, J. F., In situ formed LiNi<sub>0.8</sub>Co<sub>0.15</sub>Al<sub>0.05</sub>O<sub>2</sub>@Li<sub>4</sub>SiO<sub>4</sub> composite cathode material with high rate capability and long cycling stability for lithium-ion batteries. *Nano Energy* **2018**, *53*, 613-621.
20. Su, Y. F.; Chen, G.; Chen, L.; Li, W. K.; Zhang, Q. Y.; Yang, Z. R.; Lu, Y.; Bao, L. Y.; Tan, J.; Chen, R. J.; Chen, S.; Wu, F., Exposing the {010} Planes by Oriented Self-Assembly with Nanosheets To Improve the Electrochemical Performances of Ni-Rich Li Ni<sub>0.8</sub>Co<sub>0.1</sub>Mn<sub>0.1</sub>O<sub>2</sub> Microspheres. *Acs Applied Materials & Interfaces* **2018**, *10* (7), 6407-6414.
21. Liu, H.; Wolf, M.; Karki, K.; Yu, Y. S.; Stach, E. A.; Cabana, J.; Chapman, K. W.; Chupas, P. J., Intergranular Cracking as a Major Cause of Long-Term Capacity Fading of Layered Cathodes. *Nano Letters* **2017**, *17* (6), 3452-3457.
22. Sun, H.; Zhao, K. J., Electronic Structure and Comparative Properties of LiNi<sub>x</sub>Mn<sub>y</sub>Co<sub>z</sub>O<sub>2</sub> Cathode Materials. *Journal of Physical Chemistry C* **2017**, *121* (11), 6002-6010.

23. Park, K.; Park, J. H.; Choi, B.; Kim, J. H.; Hong, S. G.; Han, H. N., Metal phosphate-coated Ni-rich layered oxide positive electrode materials for Li-ion batteries: improved electrochemical performance and decreased Li residuals content. *Electrochimica Acta* **2017**, *257*, 217-223.
24. Jung, R.; Metzger, M.; Maglia, F.; Stinner, C.; Gasteiger, H. A., Oxygen Release and Its Effect on the Cycling Stability of LiNixMnyCozO2 (NMC) Cathode Materials for Li-Ion Batteries. *Journal of the Electrochemical Society* **2017**, *164* (7), A1361-A1377.
25. Ouyang, M. G.; Ren, D. S.; Lu, L. G.; Li, J. Q.; Feng, X. N.; Han, X. B.; Liu, G. M., Overcharge-induced capacity fading analysis for large format lithium-ion batteries with LiyNi1/3Co1/3Mn1/3O2 + LiyMn2O4 composite cathode. *Journal of Power Sources* **2015**, *279*, 626-635.
26. Ma, L.; Nie, M. Y.; Xia, J.; Dahn, J. R., A systematic study on the reactivity of different grades of charged Li NixMnyCoz O-2 with electrolyte at elevated temperatures using accelerating rate calorimetry. *Journal of Power Sources* **2016**, *327*, 145-150.
27. Bak, S. M.; Hu, E. Y.; Zhou, Y. N.; Yu, X. Q.; Senanayake, S. D.; Cho, S. J.; Kim, K. B.; Chung, K. Y.; Yang, X. Q.; Nam, K. W., Structural Changes and Thermal Stability of Charged LiNixMnyCozO2 Cathode Materials Studied by Combined In Situ Time-Resolved XRD and Mass Spectroscopy. *Acs Applied Materials & Interfaces* **2014**, *6* (24), 22594-22601.
28. Yan, P. F.; Zheng, J. M.; Liu, J.; Wang, B. Q.; Cheng, X. P.; Zhang, Y. F.; Sun, X. L.; Wang, C. M.; Zhang, J. G., Tailoring grain boundary structures and chemistry of Ni-rich layered cathodes for enhanced cycle stability of lithium-ion batteries. *Nature Energy* **2018**, *3* (7), 600-605.

29. Ryu, H. H.; Park, K. J.; Yoon, C. S.; Sun, Y. K., Capacity Fading of Ni-Rich Li NixCoyMn1-x-y O-2 (0.6 <= x <= 0.95) Cathodes for High-Energy-Density Lithium-Ion Batteries: Bulk or Surface Degradation? *Chemistry of Materials* **2018**, *30* (3), 1155-1163.
30. Xia, Y.; Zheng, J. M.; Wang, C. M.; Gu, M., Designing principle for Ni-rich cathode materials with high energy density for practical applications. *Nano Energy* **2018**, *49*, 434-452.
31. Kim, J.; Lee, H.; Cha, H.; Yoon, M.; Park, M.; Cho, J., Prospect and Reality of Ni-Rich Cathode for Commercialization. *Advanced Energy Materials* **2018**, *8* (6).
32. Kleiner, K.; Dixon, D.; Jakes, P.; Melke, J.; Yavuz, M.; Roth, C.; Nikolowski, K.; Liebau, V.; Ehrenberg, H., Fatigue of LiNi0.8Co0.15Al0.05O2 in commercial Li ion batteries. *Journal of Power Sources* **2015**, *273*, 70-82.
33. Yang, H. P.; Wu, H. H.; Ge, M. Y.; Li, L. J.; Yuan, Y. F.; Yao, Q.; Chen, J.; Xia, L. F.; Zheng, J. M.; Chen, Z. Y.; Duan, J.; Kisslinger, K.; Zeng, X. C.; Lee, W. K.; Zhang, Q. B.; Lu, J., Simultaneously Dual Modification of Ni-Rich Layered Oxide Cathode for High-Energy Lithium-Ion Batteries. *Advanced Functional Materials* **2019**, *29* (13).
34. Qiu, L.; Xiang, W.; Tian, W.; Xu, C. L.; Li, Y. C.; Wu, Z. G.; Chen, T. R.; Jia, K.; Wang, D.; He, F. R.; Guo, X. D., Polyanion and cation co-doping stabilized Ni-rich Ni-Co-Al material as cathode with enhanced electrochemical performance for Li-ion battery. *Nano Energy* **2019**, *63*.
35. Liu, Q.; Su, X.; Lei, D.; Qin, Y.; Wen, J. G.; Guo, F. M.; Wu, Y. M. A.; Rong, Y. C.; Kou, R. H.; Xiao, X. H.; Aguesse, F.; Barenó, J.; Ren, Y.; Lu, W. Q.; Li, Y. X., Approaching the capacity limit of lithium cobalt oxide in lithium ion batteries via lanthanum and aluminium doping. *Nature Energy* **2018**, *3* (11), 936-943.

36. Weigel, T.; Schipper, F.; Erickson, E. M.; Susai, F. A.; Markovsky, B.; Aurbach, D., Structural and Electrochemical Aspects of  $\text{LiNi}_{0.8}\text{Co}_{0.1}\text{Mn}_{0.1}\text{O}_2$  Cathode Materials Doped by Various Cations. *Acs Energy Letters* **2019**, *4* (2), 508-516.
37. Wu, Y. P.; Rahm, E.; Holze, R., Effects of heteroatoms on electrochemical performance of electrode materials for lithium ion batteries. *Electrochimica Acta* **2002**, *47* (21), 3491-3507.
38. Whittingham, M. S., Lithium batteries and cathode materials. *Chemical Reviews* **2004**, *104* (10), 4271-4301.
39. Cai, L.; Liu, Z. C.; An, K.; Liang, C. D., Probing Li-Ni Cation Disorder in  $\text{Li}_{1-x}\text{Ni}_{1+x-y}\text{Al}_y\text{O}_2$  Cathode Materials by Neutron Diffraction. *Journal of the Electrochemical Society* **2012**, *159* (7), A924-A928.
40. Stoyanova, R.; Zhecheva, E.; Kuzmanova, E.; Alcantara, R.; Lavela, P.; Tirado, J. L., Aluminium coordination in  $\text{LiNi}_{1-y}\text{Al}_y\text{O}_2$  solid solutions. *Solid State Ionics* **2000**, *128* (1-4), 1-10.
41. Ceder, G.; Aydinol, M. K.; Kohan, A. F., Application of first-principles calculations to the design of rechargeable Li-batteries. *Computational Materials Science* **1997**, *8* (1-2), 161-169.
42. Kang, K.; Ceder, G., Factors that affect Li mobility in layered lithium transition metal oxides. *Physical Review B* **2006**, *74* (9).
43. Dixit, M.; Markovsky, B.; Schipper, F.; Aurbach, D.; Major, D. T., Origin of Structural Degradation During Cycling and Low Thermal Stability of Ni-Rich Layered Transition Metal-Based Electrode Materials. *Journal of Physical Chemistry C* **2017**, *121* (41), 22628-22636.
44. Kondrakov, A. O.; Gesswein, H.; Galdina, K.; de Biasi, L.; Meded, V.; Filatova, E. O.; Schumacher, G.; Wenzel, W.; Hartmann, P.; Brezesinski, T.; Janek, J., Charge-Transfer-Induced

Lattice Collapse in Ni-Rich NCM Cathode Materials during Delithiation. *Journal of Physical Chemistry C* **2017**, *121* (44), 24381-24388.

45. Li, L.; Song, B. H.; Chang, Y. L.; Xia, H.; Yang, J. R.; Lee, K. S.; Lu, L., Retarded phase transition by fluorine doping in Li-rich layered  $\text{Li}_{1.2}\text{Mn}_{0.54}\text{Ni}_{0.13}\text{Co}_{0.13}\text{O}_2$  cathode material. *Journal of Power Sources* **2015**, *283*, 162-170.

46. Zheng, J. M.; Wu, X. B.; Yang, Y., Improved electrochemical performance of  $\text{Li}_{1.2}\text{Mn}_{0.54}\text{Ni}_{0.13}\text{Co}_{0.13}\text{O}_2$  cathode material by fluorine incorporation. *Electrochimica Acta* **2013**, *105*, 200-208.

47. Kong, F. T.; Liang, C. P.; Longo, R. C.; Yeon, D. H.; Zheng, Y. P.; Park, J. H.; Doo, S. G.; Cho, K., Conflicting Roles of Anion Doping on the Electrochemical Performance of Li-Ion Battery Cathode Materials. *Chemistry of Materials* **2016**, *28* (19), 6942-6952.

48. Su, Z.; Lu, Z. W.; Gao, X. P.; Shen, P. W.; Liu, X. J.; Wang, J. Q., Preparation and electrochemical properties of indium- and sulfur-doped  $\text{LiMnO}_2$  with orthorhombic structure as cathode materials. *Journal of Power Sources* **2009**, *189* (1), 411-415.

49. Sun, Y. K.; Oh, S. W.; Yoon, C. S.; Bang, H. J.; Prakash, J., Effect of sulfur and nickel doping on morphology and electrochemical performance of  $\text{LiNi}_{0.5}\text{Mn}_{1.5}\text{O}_{4-x}\text{S}_x$  spinel material in 3-V region. *Journal of Power Sources* **2006**, *161* (1), 19-26.

50. Sun, Z. H.; Xu, L. Q.; Dong, C. Q.; Zhang, H. T.; Zhang, M. T.; Ma, Y. F.; Liu, Y. Y.; Li, Z. J.; Zhou, Y.; Han, Y.; Chen, Y. S., A facile gaseous sulfur treatment strategy for Li-rich and Ni-rich cathode materials with high cycling and rate performance. *Nano Energy* **2019**, *63*.

51. Cheng, X. P.; Zheng, J. M.; Lu, J. X.; Li, Y. H.; Yan, P. F.; Zhang, Y. F., Realizing superior cycling stability of Ni-Rich layered cathode by combination of grain boundary engineering and surface coating. *Nano Energy* **2019**, *62*, 30-37.

52. Lee, S. W.; Kim, M. S.; Jeong, J. H.; Kim, D. H.; Chung, K. Y.; Roh, K. C.; Kim, K. B., Li<sub>3</sub>PO<sub>4</sub> surface coating on Ni-rich LiNi<sub>0.6</sub>Co<sub>0.2</sub>Mn<sub>0.2</sub>O<sub>2</sub> by a citric acid assisted sol-gel method: Improved thermal stability and high-voltage performance. *Journal of Power Sources* **2017**, *360*, 206-214.
53. Zhao, E. Y.; Chen, M. M.; Hu, Z. B.; Chen, D. F.; Yang, L. M.; Xiao, X. L., Improved cycle stability of high-capacity Ni-rich LiNi<sub>0.8</sub>Mn<sub>0.1</sub>Co<sub>0.1</sub>O<sub>2</sub> at high cut-off voltage by Li<sub>2</sub>SiO<sub>3</sub> coating. *Journal of Power Sources* **2017**, *343*, 345-353.
54. Qing, R. P.; Shi, J. L.; Xiao, D. D.; Zhang, X. D.; Yin, Y. X.; Zhai, Y. B.; Gu, L.; Guo, Y. G., Enhancing the Kinetics of Li-Rich Cathode Materials through the Pinning Effects of Gradient Surface Na<sup>+</sup> Doping. *Advanced Energy Materials* **2016**, *6* (6).
55. Song, H. G.; Kim, J. Y.; Kim, K. T.; Park, Y. J., Enhanced electrochemical properties of Li(Ni<sub>0.4</sub>Co<sub>0.3</sub>Mn<sub>0.3</sub>)O<sub>2</sub> cathode by surface modification using Li<sub>3</sub>PO<sub>4</sub>-based materials. *Journal of Power Sources* **2011**, *196* (16), 6847-6855.
56. Jo, C. H.; Cho, D. H.; Noh, H. J.; Yashiro, H.; Sun, Y. K.; Myung, S. T., An effective method to reduce residual lithium compounds on Ni-rich Li Ni<sub>0.6</sub>Co<sub>0.2</sub>Mn<sub>0.2</sub> O<sub>2</sub> active material using a phosphoric acid derived Li<sub>3</sub>PO<sub>4</sub> nanolayer. *Nano Research* **2015**, *8* (5), 1464-1479.
57. Seteni, B.; Rapulenyane, N.; Ngila, J. C.; Mpelane, S.; Luo, H. Z., Coating effect of LiFePO<sub>4</sub> and Al<sub>2</sub>O<sub>3</sub> on Li<sub>1.2</sub>Mn<sub>0.54</sub>Ni<sub>0.13</sub>Co<sub>0.13</sub>O<sub>2</sub> cathode surface for lithium ion batteries. *Journal of Power Sources* **2017**, *353*, 210-220.
58. Zhu, L.; Yan, T. F.; Jia, D.; Wang, Y.; Wu, Q.; Gu, H. T.; Wu, Y. M.; Tang, W. P., LiFePO<sub>4</sub>-Coated LiNi<sub>0.5</sub>Co<sub>0.2</sub>Mn<sub>0.3</sub>O<sub>2</sub> Cathode Materials with Improved High Voltage Electrochemical Performance and Enhanced Safety for Lithium Ion Pouch Cells. *Journal of the Electrochemical Society* **2019**, *166* (3), A5437-A5444.

59. Chen, S.; He, T.; Su, Y. F.; Lu, Y.; Ban, L. Y.; Chen, L.; Zhang, Q. Y.; Wang, J.; Chen, R. J.; Wu, F., Ni-Rich  $\text{LiNi}_{0.8}\text{Co}_{0.1}\text{Mn}_{0.1}\text{O}_2$  Oxide Coated by Dual-Conductive Layers as High Performance Cathode for Lithium-Ion Batteries. *Acs Applied Materials & Interfaces* **2017**, *9* (35), 29732-29743.
60. Wang, D.; Li, X. H.; Wang, Z. X.; Guo, H. J.; Xu, Y.; Fan, Y. L., Co-modification of  $\text{LiNi}_{0.5}\text{Co}_{0.2}\text{Mn}_{0.3}\text{O}_2$  cathode materials with zirconium substitution and surface polypyrrole coating: towards superior high voltage electrochemical performances for lithium ion batteries. *Electrochimica Acta* **2016**, *196*, 101-109.
61. Cho, W.; Kim, S. M.; Song, J. H.; Yim, T.; Woo, S. G.; Lee, K. W.; Kim, J. S.; Kim, Y. J., Improved electrochemical and thermal properties of nickel rich  $\text{LiNi}_{0.6}\text{Co}_{0.2}\text{Mn}_{0.2}\text{O}_2$  cathode materials by  $\text{SiO}_2$  coating. *Journal of Power Sources* **2015**, *282*, 45-50.
62. Liang, L. W.; Hu, G. R.; Jiang, F.; Cao, Y. B., Electrochemical behaviours of  $\text{SiO}_2$ -coated  $\text{LiNi}_{0.8}\text{Co}_{0.1}\text{Mn}_{0.1}\text{O}_2$  cathode materials by a novel modification method. *Journal of Alloys and Compounds* **2016**, *657*, 570-581.
63. Schipper, F.; Bouzaglo, H.; Dixit, M.; Erickson, E. M.; Weigel, T.; Talianker, M.; Grinblat, J.; Burstein, L.; Schmidt, M.; Lampert, J.; Erk, C.; Markovsky, B.; Major, D. T.; Aurbach, D., From Surface  $\text{ZrO}_2$  Coating to Bulk Zr Doping by High Temperature Annealing of Nickel-Rich Lithiated Oxides and Their Enhanced Electrochemical Performance in Lithium Ion Batteries. *Advanced Energy Materials* **2018**, *8* (4).
64. Wang, Z. Y.; Liu, E. Z.; Guo, L. C.; Shi, C. S.; He, C. N.; Li, J. J.; Zhao, N. Q., Cycle performance improvement of Li-rich layered cathode material  $\text{LiLi}_{0.2}\text{Mn}_{0.54}\text{Ni}_{0.13}\text{Co}_{0.13}\text{O}_2$  by  $\text{ZrO}_2$  coating. *Surface & Coatings Technology* **2013**, *235*, 570-576.

65. Zhang, X. F.; Belharouak, I.; Li, L.; Lei, Y.; Elam, J. W.; Nie, A. M.; Chen, X. Q.; Yassar, R. S.; Axelbaum, R. L., Structural and Electrochemical Study of Al<sub>2</sub>O<sub>3</sub> and TiO<sub>2</sub> Coated Li<sub>1.2</sub>Ni<sub>0.13</sub>Mn<sub>0.54</sub>Co<sub>0.13</sub>O<sub>2</sub> Cathode Material Using ALD. *Advanced Energy Materials* **2013**, *3* (10), 1299-1307.
66. Dong, M. X.; Wang, Z. X.; Li, H. K.; Guo, H. J.; Li, X. H.; Shih, K. M.; Wang, J. X., Metallurgy Inspired Formation of Homogeneous Al<sub>2</sub>O<sub>3</sub> Coating Layer To Improve the Electrochemical Properties of LiNi<sub>0.8</sub>Co<sub>0.1</sub>Mn<sub>0.1</sub>O<sub>2</sub> Cathode Material. *Acs Sustainable Chemistry & Engineering* **2017**, *5* (11), 10199-10205.
67. Xu, G. L.; Liu, Q.; Lau, K. K. S.; Liu, Y.; Liu, X.; Gao, H.; Zhou, X. W.; Zhuang, M. H.; Ren, Y.; Li, J. D.; Shao, M. H.; Ouyang, M. G.; Pan, F.; Chen, Z. H.; Amine, K.; Chen, G. H., Building ultraconformal protective layers on both secondary and primary particles of layered lithium transition metal oxide cathodes. *Nature Energy* **2019**, *4* (6), 484-494.
68. Zhang, J. C.; Yang, Z. Z.; Gao, R.; Gu, L.; Hu, Z. B.; Liu, X. F., Suppressing the Structure Deterioration of Ni-Rich LiNi<sub>0.8</sub>Co<sub>0.1</sub>Mn<sub>0.1</sub>O<sub>2</sub> through Atom-Scale Interfacial Integration of Self-Forming Hierarchical Spinel Layer with Ni Gradient Concentration. *Acs Applied Materials & Interfaces* **2017**, *9* (35), 29794-29803.
69. Kim, J.; Cho, H.; Jeong, H. Y.; Ma, H.; Lee, J.; Hwang, J.; Park, M.; Cho, J., Self-Induced Concentration Gradient in Nickel-Rich Cathodes by Sacrificial Polymeric Bead Clusters for High-Energy Lithium-Ion Batteries. *Advanced Energy Materials* **2017**, *7* (12).
70. Wei, G. Z.; Lu, X.; Ke, F. S.; Huang, L.; Li, J. T.; Wang, Z. X.; Zhou, Z. Y.; Sun, S. G., Crystal Habit-Tuned Nanoplate Material of Li Li<sub>1/3-2x/3</sub>Ni<sub>x</sub>Mn<sub>2/3-x/3</sub>O<sub>2</sub> for High-Rate Performance Lithium-Ion Batteries. *Advanced Materials* **2010**, *22* (39), 4364-+.

71. Kondrakov, A. O.; Schmidt, A.; Xu, J.; Gesswein, H.; Monig, R.; Hartmann, P.; Sommer, H.; Brezesinski, T.; Janek, J., Anisotropic Lattice Strain and Mechanical Degradation of High- and Low-Nickel NCM Cathode Materials for Li-Ion Batteries. *Journal of Physical Chemistry C* **2017**, *121* (6), 3286-3294.
72. Xu, X.; Huo, H.; Jian, J. Y.; Wang, L. G.; Zhu, H.; Xu, S.; He, X. S.; Yin, G. P.; Du, C. Y.; Sun, X. L., Radially Oriented Single-Crystal Primary Nanosheets Enable Ultrahigh Rate and Cycling Properties of  $\text{LiNi}_{0.8}\text{Co}_{0.1}\text{Mn}_{0.1}\text{O}_2$  Cathode Material for Lithium-Ion Batteries. *Advanced Energy Materials* **2019**, *9* (15).
73. Sun, Y. K.; Myung, S. T.; Park, B. C.; Prakash, J.; Belharouak, I.; Amine, K., High-energy cathode material for long-life and safe lithium batteries. *Nature Materials* **2009**, *8* (4), 320-324.
74. Kim, U. H.; Ryu, H. H.; Kim, J. H.; Mucke, R.; Kaghazchi, P.; Yoon, C. S.; Sun, Y. K., Microstructure-Controlled Ni-Rich Cathode Material by Microscale Compositional Partition for Next-Generation Electric Vehicles. *Advanced Energy Materials* **2019**, *9* (15).
75. Lim, B. B.; Myung, S. T.; Yoon, C. S.; Sun, Y. K., Comparative Study of Ni-Rich Layered Cathodes for Rechargeable Lithium Batteries:  $\text{Li Ni}_{0.85}\text{Co}_{0.11}\text{Al}_{0.04}\text{O}_2$  and  $\text{Li Ni}_{0.84}\text{Co}_{0.06}\text{Mn}_{0.09}\text{Al}_{0.01}\text{O}_2$  with Two-Step Full Concentration Gradients. *Acs Energy Letters* **2016**, *1* (1), 283-289.
76. Lim, B. B.; Yoon, S. J.; Park, K. J.; Yoon, C. S.; Kim, S. J.; Lee, J. J.; Sun, Y. K., Advanced Concentration Gradient Cathode Material with Two-Slope for High-Energy and Safe Lithium Batteries. *Advanced Functional Materials* **2015**, *25* (29), 4673-4680.

77. Sun, Y. K.; Chen, Z. H.; Noh, H. J.; Lee, D. J.; Jung, H. G.; Ren, Y.; Wang, S.; Yoon, C. S.; Myung, S. T.; Amine, K., Nanostructured high-energy cathode materials for advanced lithium batteries. *Nature Materials* **2012**, *11* (11), 942-947.
78. Lee, E. J.; Chen, Z. H.; Noh, H. J.; Nam, S. C.; Kang, S.; Kim, D. H.; Amine, K.; Sun, Y. K., Development of Microstrain in Aged Lithium Transition Metal Oxides. *Nano Letters* **2014**, *14* (8), 4873-4880.
79. Shim, J.; KostECKI, R.; Richardson, T.; Song, X.; StriEBEL, K. A., Electrochemical analysis for cycle performance and capacity fading of a lithium-ion battery cycled at elevated temperature. *Journal of Power Sources* **2002**, *112* (1), 222-230.
80. Abraham, D. P.; TwEStEN, R. D.; BalASUBRAMANIAN, M.; PETROV, I.; MCBREEN, J.; AMINE, K., Surface changes on LiNi<sub>0.8</sub>Co<sub>0.2</sub>O<sub>2</sub> particles during testing of high-power lithium-ion cells. *Electrochemistry Communications* **2002**, *4* (8), 620-625.
81. Wright, R. B.; Christophersen, J. P.; Motloch, C. G.; Belt, J. R.; Ho, C. D.; Battaglia, V. S.; Barnes, J. A.; Duong, T. Q.; Sutula, R. A., Power fade and capacity fade resulting from cycle-life testing of Advanced Technology Development Program lithium-ion batteries. *Journal of Power Sources* **2003**, *119*, 865-869.
82. Belharouak, I.; Lu, W. Q.; Vissers, D.; Amine, K., Safety characteristics of Li(Ni<sub>0.8</sub>Co<sub>0.15</sub>Al<sub>0.05</sub>)O<sub>2</sub> and Li(Ni<sub>1/3</sub>CO<sub>1/3</sub>Mn<sub>1/3</sub>)O<sub>2</sub>. *Electrochemistry Communications* **2006**, *8* (2), 329-335.
83. Dahn, J. R.; Fuller, E. W.; Obrovac, M.; Vonsacken, U., THERMAL-STABILITY OF LIXCOO<sub>2</sub>, LIXNIO<sub>2</sub> AND LAMBDA-MNO<sub>2</sub> AND CONSEQUENCES FOR THE SAFETY OF LI-ION CELLS. *Solid State Ionics* **1994**, *69* (3-4), 265-270.

84. Arai, H.; Okada, S.; Sakurai, Y.; Yamaki, J., Electrochemical and thermal behavior of  $\text{LiNi}_{1-z}\text{MzO}_2$  (M = Co, Mn, Ti). *Journal of the Electrochemical Society* **1997**, *144* (9), 3117-3125.
85. Noh, H. J.; Chen, Z. H.; Yoon, C. S.; Lu, J.; Amine, K.; Sun, Y. K., Cathode Material with Nanorod Structure-An Application for Advanced High-Energy and Safe Lithium Batteries. *Chemistry of Materials* **2013**, *25* (10), 2109-2115.
86. Wei, Q. L.; Wang, X. Y.; Yang, X. K.; Ju, B. W.; Hu, B. N.; Shu, H. B.; Wen, W. C.; Zhou, M.; Song, Y. F.; Wu, H.; Hu, H., Spherical concentration-gradient  $\text{LiMn}_{1.87}\text{Ni}_{0.13}\text{O}_4$  spinel as a high performance cathode for lithium ion batteries. *Journal of Materials Chemistry A* **2013**, *1* (12), 4010-4016.
87. Sun, Y. K.; Kim, D. H.; Jung, H. G.; Myung, S. T.; Amine, K., High-voltage performance of concentration-gradient  $\text{LiNi}_{0.67}\text{Co}_{0.15}\text{Mn}_{0.18}\text{O}_2$  cathode material for lithium-ion batteries. *Electrochimica Acta* **2010**, *55* (28), 8621-8627.
88. Hou, P. Y.; Zhang, L. Q.; Gao, X. P., A high-energy, full concentration-gradient cathode material with excellent cycle and thermal stability for lithium ion batteries. *Journal of Materials Chemistry A* **2014**, *2* (40), 17130-17138.
89. Armand, M.; Tarascon, J. M., Building better batteries. *Nature* **2008**, *451* (7179), 652-657.
90. Tarascon, J. M.; Armand, M., Issues and challenges facing rechargeable lithium batteries. *Nature* **2001**, *414* (6861), 359-367.
91. Chan, C. K.; Peng, H. L.; Liu, G.; McIlwrath, K.; Zhang, X. F.; Huggins, R. A.; Cui, Y., High-performance lithium battery anodes using silicon nanowires. *Nature Nanotechnology* **2008**, *3* (1), 31-35.

92. Etacheri, V.; Marom, R.; Elazari, R.; Salitra, G.; Aurbach, D., Challenges in the development of advanced Li-ion batteries: a review. *Energy & Environmental Science* **2011**, *4* (9), 3243-3262.
93. Zhu, B.; Jin, Y.; Tan, Y. L.; Zong, L. Q.; Hu, Y.; Chen, L.; Chen, Y. B.; Zhang, Q.; Zhu, J., Scalable Production of Si Nanoparticles Directly from Low Grade Sources for Lithium-Ion Battery Anode. *Nano Letters* **2015**, *15* (9), 5750-5754.
94. Wu, H.; Yu, G. H.; Pan, L. J.; Liu, N. A.; McDowell, M. T.; Bao, Z. A.; Cui, Y., Stable Li-ion battery anodes by in-situ polymerization of conducting hydrogel to conformally coat silicon nanoparticles. *Nature Communications* **2013**, *4*.
95. Ko, M.; Chae, S.; Ma, J.; Kim, N.; Lee, H. W.; Cui, Y.; Cho, J., Scalable synthesis of silicon-nanolayer-embedded graphite for high-energy lithium-ion batteries. *Nature Energy* **2016**, *1*.
96. Szczech, J. R.; Jin, S., Nanostructured silicon for high capacity lithium battery anodes. *Energy & Environmental Science* **2011**, *4* (1), 56-72.
97. Lv, G. X.; Zhu, B.; Li, X. Q.; Chen, C. L.; Li, J. L.; Jin, Y.; Hu, X. Z.; Zhu, J., Simultaneous Perforation and Doping of Si Nanoparticles for Lithium-Ion Battery Anode. *Acs Applied Materials & Interfaces* **2017**, *9* (51), 44452-44457.
98. Lee, S. W.; McDowell, M. T.; Choi, J. W.; Cui, Y., Anomalous Shape Changes of Silicon Nanopillars by Electrochemical Lithiation. *Nano Letters* **2011**, *11* (7), 3034-3039.
99. Liu, N. A.; Cui, Y.; Sun, Y.; Liu, N.; Cui, Y., Promises and challenges of nanomaterials for lithium-based rechargeable batteries. *Nature Energy* **2016**, *1* (7).
100. Goodenough, J. B.; Kim, Y., Challenges for Rechargeable Li Batteries. *Chemistry of Materials* **2010**, *22* (3), 587-603.

101. Wu, H.; Chan, G.; Choi, J. W.; Ryu, I.; Yao, Y.; McDowell, M. T.; Lee, S. W.; Jackson, A.; Yang, Y.; Hu, L. B.; Cui, Y., Stable cycling of double-walled silicon nanotube battery anodes through solid-electrolyte interphase control. *Nature Nanotechnology* **2012**, *7* (5), 309-314.
102. Roduner, E., Size matters: why nanomaterials are different. *Chemical Society Reviews* **2006**, *35* (7), 583-592.
103. Hochbaum, A. I.; Fan, R.; He, R. R.; Yang, P. D., Controlled growth of Si nanowire arrays for device integration. *Nano Letters* **2005**, *5* (3), 457-460.
104. Li, X. L.; Meduri, P.; Chen, X. L.; Qi, W.; Engelhard, M. H.; Xu, W.; Ding, F.; Xiao, J.; Wang, W.; Wang, C. M.; Zhang, J. G.; Liu, J., Hollow core-shell structured porous Si-C nanocomposites for Li-ion battery anodes. *Journal of Materials Chemistry* **2012**, *22* (22), 11014-11017.
105. Hu, J. Q.; Bando, Y.; Liu, Z. W.; Zhan, J. H.; Golberg, D.; Sekiguchi, T., Synthesis of crystalline silicon tubular nanostructures with ZnS nanowires as removable templates. *Angewandte Chemie-International Edition* **2004**, *43* (1), 63-66.
106. Ge, M. Y.; Rong, J. P.; Fang, X.; Zhang, A. Y.; Lu, Y. H.; Zhou, C. W., Scalable preparation of porous silicon nanoparticles and their application for lithium-ion battery anodes. *Nano Research* **2013**, *6* (3), 174-181.
107. Xiao, Q. F.; Gu, M.; Yang, H.; Li, B.; Zhang, C. M.; Liu, Y.; Liu, F.; Dai, F.; Yang, L.; Liu, Z. Y.; Xiao, X. C.; Liu, G.; Zhao, P.; Zhang, S. L.; Wang, C. M.; Lu, Y. F.; Cai, M., Inward lithium-ion breathing of hierarchically porous silicon anodes. *Nature Communications* **2015**, *6*.

108. Li, X. L.; Gu, M.; Hu, S. Y.; Kennard, R.; Yan, P. F.; Chen, X. L.; Wang, C. M.; Sailor, M. J.; Zhang, J. G.; Liu, J., Mesoporous silicon sponge as an anti-pulverization structure for high-performance lithium-ion battery anodes. *Nature Communications* **2014**, *5*.
109. Chan, C. K.; Patel, R. N.; O'Connell, M. J.; Korgel, B. A.; Cui, Y., Solution-Grown Silicon Nanowires for Lithium-Ion Battery Anodes. *Acs Nano* **2010**, *4* (3), 1443-1450.
110. Park, M. H.; Kim, M. G.; Joo, J.; Kim, K.; Kim, J.; Ahn, S.; Cui, Y.; Cho, J., Silicon Nanotube Battery Anodes. *Nano Letters* **2009**, *9* (11), 3844-3847.
111. Hassan, F. M.; Batmaz, R.; Li, J. D.; Wang, X. L.; Xiao, X. C.; Yu, A. P.; Chen, Z. W., Evidence of covalent synergy in silicon-sulfur-graphene yielding highly efficient and long-life lithium-ion batteries. *Nature Communications* **2015**, *6*.
112. Zhang, X. H.; Qiu, X. Y.; Kong, D. B.; Zhou, L.; Li, Z. H.; Li, X. L.; Zhi, L. J., Silicene Flowers: A Dual Stabilized Silicon Building Block for High-Performance Lithium Battery Anodes. *Acs Nano* **2017**, *11* (7), 7476-7484.
113. Sun, Y. M.; Liu, N. A.; Cui, Y., Promises and challenges of nanomaterials for lithium-based rechargeable batteries. *Nature Energy* **2016**, *1*.
114. Wang, C.; Wu, H.; Chen, Z.; McDowell, M. T.; Cui, Y.; Bao, Z. A., Self-healing chemistry enables the stable operation of silicon microparticle anodes for high-energy lithium-ion batteries. *Nature Chemistry* **2013**, *5* (12), 1042-1048.
115. Tian, H. J.; Tan, X. J.; Xin, F. X.; Wang, C. S.; Han, W. Q., Micro-sized nano-porous Si/C anodes for lithium ion batteries. *Nano Energy* **2015**, *11*, 490-499.
116. Kim, H.; Han, B.; Choo, J.; Cho, J., Three-Dimensional Porous Silicon Particles for Use in High-Performance Lithium Secondary Batteries. *Angewandte Chemie-International Edition* **2008**, *47* (52), 10151-10154.

117. Yi, R.; Dai, F.; Gordin, M. L.; Chen, S. R.; Wang, D. H., Micro-sized Si-C Composite with Interconnected Nanoscale Building Blocks as High-Performance Anodes for Practical Application in Lithium-Ion Batteries. *Advanced Energy Materials* **2013**, *3* (3), 295-300.
118. Xu, Q.; Li, J. Y.; Sun, J. K.; Yin, Y. X.; Wan, L. J.; Guo, Y. G., Watermelon-Inspired Si/C Microspheres with Hierarchical Buffer Structures for Densely Compacted Lithium-Ion Battery Anodes. *Advanced Energy Materials* **2017**, *7* (3).
119. Liu, G.; Xun, S. D.; Vukmirovic, N.; Song, X. Y.; Olalde-Velasco, P.; Zheng, H. H.; Battaglia, V. S.; Wang, L. W.; Yang, W. L., Polymers with Tailored Electronic Structure for High Capacity Lithium Battery Electrodes. *Advanced Materials* **2011**, *23* (40), 4679-+.
120. Li, X. Z.; Fang, Y. Y.; Lin, X. Q.; Tian, M.; An, X. C.; Fu, Y.; Li, R.; Jin, J.; Ma, J. T., MOF derived Co<sub>3</sub>O<sub>4</sub> nanoparticles embedded in N-doped mesoporous carbon layer/MWCNT hybrids: extraordinary bi-functional electrocatalysts for OER and ORR. *Journal of Materials Chemistry A* **2015**, *3* (33), 17392-17402.
121. Li, S. W.; Fu, X. T.; Zhou, J. W.; Han, Y. Z.; Qi, P. F.; Gao, X.; Feng, X.; Wang, B., An effective approach to improve the electrochemical performance of LiNi<sub>0.6</sub>Co<sub>0.2</sub>Mn<sub>0.2</sub>O<sub>2</sub> cathode by an MOF-derived coating. *Journal of Materials Chemistry A* **2016**, *4* (16), 5823-5827.
122. Xiao, Z. T.; Meng, J. S.; Li, Q.; Wang, X. P.; Huang, M.; Liu, Z.; Han, C. H.; Mai, L. Q., Novel MOF shell-derived surface modification of Li-rich layered oxide cathode for enhanced lithium storage. *Science Bulletin* **2018**, *63* (1), 46-53.
123. Boulineau, A.; Simonin, L.; Colin, J. F.; Bourbon, C.; Patoux, S., First Evidence of Manganese-Nickel Segregation and Densification upon Cycling in Li-Rich Layered Oxides for Lithium Batteries. *Nano Letters* **2013**, *13* (8), 3857-3863.

124. Carrasco, J. A.; Romero, J.; Abellan, G.; Hernandez-Saz, J.; Molina, S. I.; Marti-Gastaldo, C.; Coronado, E., Small-pore driven high capacitance in a hierarchical carbon via carbonization of Ni-MOF-74 at low temperatures. *Chemical Communications* **2016**, 52 (58), 9141-9144.
125. Zhang, H. L.; May, B. M.; Omenya, F.; Whittingham, M. S.; Cabana, J.; Zhou, G. W., Layered Oxide Cathodes for Li-Ion Batteries: Oxygen Loss and Vacancy Evolution. *Chemistry of Materials* **2019**, 31 (18), 7790-7798.
126. Yin, C. J.; Zhou, H. M.; Yang, Z. H.; Li, J., Synthesis and Electrochemical Properties of LiNi<sub>0.5</sub>Mn<sub>1.5</sub>O<sub>4</sub> for Li-Ion Batteries by the Metal-Organic Framework Method. *Acs Applied Materials & Interfaces* **2018**, 10 (16), 13625-13634.
127. Noh, H. J.; Youn, S.; Yoon, C. S.; Sun, Y. K., Comparison of the structural and electrochemical properties of layered Li NixCoyMnz O-2 (x=1/3, 0.5, 0.6, 0.7, 0.8 and 0.85) cathode material for lithium-ion batteries. *Journal of Power Sources* **2013**, 233, 121-130.
128. Yu, H. J.; Qian, Y. M.; Otani, M. R.; Tang, D. M.; Guo, S. H.; Zhu, Y. B.; Zhou, H. S., Study of the lithium/nickel ions exchange in the layered LiNi<sub>0.42</sub>Mn<sub>0.42</sub>Co<sub>0.16</sub>O<sub>2</sub> cathode material for lithium ion batteries: experimental and first-principles calculations. *Energy & Environmental Science* **2014**, 7 (3), 1068-1078.
129. Lin, F.; Markus, I. M.; Nordlund, D.; Weng, T. C.; Asta, M. D.; Xin, H. L. L.; Doeff, M. M., Surface reconstruction and chemical evolution of stoichiometric layered cathode materials for lithium-ion batteries. *Nature Communications* **2014**, 5.
130. Yan, P. F.; Nie, A. M.; Zheng, J. M.; Zhou, Y. G.; Lu, D. P.; Zhang, X. F.; Xu, R.; Belharouak, I.; Zu, X. T.; Xiao, J.; Amine, K.; Liu, J.; Gao, F.; Shahbazian-Yassar, R.; Zhang, J. G.; Wang, C. M., Evolution of Lattice Structure and Chemical Composition of the Surface

Reconstruction Layer in  $\text{Li}_{1.2}\text{Ni}_{0.2}\text{Mn}_{0.6}\text{O}_2$  Cathode Material for Lithium Ion Batteries. *Nano Letters* **2015**, *15* (1), 514-522.

131. Qiu, B.; Zhang, M. H.; Wu, L. J.; Wang, J.; Xia, Y. G.; Qian, D. N.; Liu, H. D.; Hy, S.; Chen, Y.; An, K.; Zhu, Y. M.; Liu, Z. P.; Meng, Y. S., Gas-solid interfacial modification of oxygen activity in layered oxide cathodes for lithium-ion batteries. *Nature Communications* **2016**, *7*.

132. Kim, H.; Kim, M. G.; Jeong, H. Y.; Nam, H.; Cho, J., A New Coating Method for Alleviating Surface Degradation of  $\text{LiNi}_{0.6}\text{Co}_{0.2}\text{Mn}_{0.2}\text{O}_2$  Cathode Material: Nanoscale Surface Treatment of Primary Particles. *Nano Letters* **2015**, *15* (3), 2111-2119.

133. Sun, Y. K.; Kim, D. H.; Yoon, C. S.; Myung, S. T.; Prakash, J.; Amine, K., A Novel Cathode Material with a Concentration-Gradient for High-Energy and Safe Lithium-Ion Batteries. *Advanced Functional Materials* **2010**, *20* (3), 485-491.

134. Zhuang, G. V.; Chen, G. Y.; Shim, J.; Song, X. Y.; Ross, P. N.; Richardson, T. J.,  $\text{Li}_2\text{CO}_3$  in  $\text{LiNi}_{0.8}\text{Co}_{0.15}\text{Al}_{0.05}\text{O}_2$  cathodes and its effects on capacity and power. *Journal of Power Sources* **2004**, *134* (2), 293-297.

135. Lee, J. I.; Shin, M.; Hong, D.; Park, S., Efficient Li-Ion-Conductive Layer for the Realization of Highly Stable High-Voltage and High-Capacity Lithium Metal Batteries. *Advanced Energy Materials* **2019**, *9* (13).

136. Fan, X. M.; Hu, G. R.; Zhang, B.; Ou, X.; Zhang, J. F.; Zhao, W. G.; Jia, H. P.; Zou, L. F.; Li, P.; Yang, Y., Crack-free single-crystalline Ni-rich layered NCM cathode enable superior cycling performance of lithium-ion batteries. *Nano Energy* **2020**, *70*.

137. Wang, Q.; Shen, C. H.; Shen, S. Y.; Xu, Y. F.; Shi, C. G.; Huang, L.; Li, J. T.; Sun, S. G., Origin of Structural Evolution in Capacity Degradation for Overcharged NMC622 via Operando Coupled Investigation. *Acs Applied Materials & Interfaces* **2017**, *9* (29), 24731-24742.
138. Nam, K. W.; Bak, S. M.; Hu, E. Y.; Yu, X. Q.; Zhou, Y. N.; Wang, X. J.; Wu, L. J.; Zhu, Y. M.; Chung, K. Y.; Yang, X. Q., Combining In Situ Synchrotron X-Ray Diffraction and Absorption Techniques with Transmission Electron Microscopy to Study the Origin of Thermal Instability in Overcharged Cathode Materials for Lithium-Ion Batteries. *Advanced Functional Materials* **2013**, *23* (8), 1047-1063.
139. Zheng, J. M.; Kan, W. H.; Manthiram, A., Role of Mn Content on the Electrochemical Properties of Nickel-Rich Layered  $\text{LiNi}_{0.8-x}\text{Co}_{0.1}\text{Mn}_{0.1+x}\text{O}_2$  ( $0.0 \leq x \leq 0.08$ ) Cathodes for Lithium-Ion Batteries. *Acs Applied Materials & Interfaces* **2015**, *7* (12), 6926-6934.
140. Li, Y. C.; Xiang, W.; Xiao, Y.; Wu, Z. G.; Xu, C. L.; Xu, W.; Xu, Y. D.; Wu, C.; Yang, Z. G.; Guo, X. D., Synergy of doping and coating induced heterogeneous structure and concentration gradient in Ni-rich cathode for enhanced electrochemical performance. *Journal of Power Sources* **2019**, *423*, 144-151.
141. Nam, G. W.; Park, N. Y.; Park, K. J.; Yang, J.; Liu, J.; Yoon, C. S.; Sun, Y. K., Capacity Fading of Ni-Rich NCA Cathodes: Effect of Microcracking Extent. *Acs Energy Letters* **2019**, *4* (12), 2995-3001.
142. Liu, S. Y.; Dang, Z. Y.; Liu, D.; Zhang, C. C.; Huang, T.; Yu, A. S., Comparative studies of zirconium doping and coating on  $\text{LiNi}_{0.6}\text{Co}_{0.2}\text{Mn}_{0.2}\text{O}_2$  cathode material at elevated temperatures. *Journal of Power Sources* **2018**, *396*, 288-296.
143. Jiao, S. H.; Ren, X. D.; Cao, R. G.; Engelhard, M. H.; Liu, Y. Z.; Hu, D. H.; Mei, D. H.; Zheng, J. M.; Zhao, W. G.; Li, Q. Y.; Liu, N.; Adams, B. D.; Ma, C.; Liu, J.; Zhang, J.

G.; Xu, W., Stable cycling of high-voltage lithium metal batteries in ether electrolytes. *Nature Energy* **2018**, *3* (9), 739-746.

144. Sun, D. R.; Sun, F. X.; Deng, X. Y.; Li, Z. H., Mixed-Metal Strategy on Metal-Organic Frameworks (MOFs) for Functionalities Expansion: Co Substitution Induces Aerobic Oxidation of Cyclohexene over Inactive Ni-MOF-74. *Inorganic Chemistry* **2015**, *54* (17), 8639-8643.

145. Son, I. H.; Park, J. H.; Kwon, S.; Park, S.; Rummeli, M. H.; Bachmatiuk, A.; Song, H. J.; Ku, J.; Choi, J. W.; Choi, J. M.; Doo, S. G.; Chang, H., Silicon carbide-free graphene growth on silicon for lithium-ion battery with high volumetric energy density. *Nature Communications* **2015**, *6*.

146. Jin, Y.; Li, S.; Kushima, A.; Zheng, X. Q.; Sun, Y. M.; Xie, J.; Sun, J.; Xue, W. J.; Zhou, G. M.; Wu, J.; Shi, F. F.; Zhang, R. F.; Zhu, Z.; So, K. P.; Cui, Y.; Li, J., Self-healing SEI enables full-cell cycling of a silicon-majority anode with a coulombic efficiency exceeding 99.9%. *Energy & Environmental Science* **2017**, *10* (2), 580-592.

147. Jin, Y.; Zhu, B.; Lu, Z. D.; Liu, N.; Zhu, J., Challenges and Recent Progress in the Development of Si Anodes for Lithium-Ion Battery. *Advanced Energy Materials* **2017**, *7* (23).

148. Park, K. S.; Schougaard, S. B.; Goodenough, J. B., Conducting-polymer/iron-redox-couple composite cathodes for lithium secondary batteries. *Advanced Materials* **2007**, *19* (6), 848-+.

149. Chao, D. L.; Xia, X. H.; Liu, J. L.; Fan, Z. X.; Ng, C. F.; Lin, J. Y.; Zhang, H.; Shen, Z. X.; Fan, H. J., A V<sub>2</sub>O<sub>5</sub>/Conductive-Polymer Core/Shell Nanobelt Array on Three-Dimensional Graphite Foam: A High-Rate, Ultrastable, and Freestanding Cathode for Lithium-Ion Batteries. *Advanced Materials* **2014**, *26* (33), 5794-5800.

150. Gowda, S. R.; Reddy, A. L. M.; Shaijumon, M. M.; Zhan, X. B.; Ci, L. J.; Ajayan, P. M., Conformal Coating of Thin Polymer Electrolyte Layer on Nanostructured Electrode Materials for Three-Dimensional Battery Applications. *Nano Letters* **2011**, *11* (1), 101-106.
151. Vernitskaya, T. V.; Efimov, O. N., Polypyrrole: A conducting polymer (synthesis, properties, and applications). *Uspekhi Khimii* **1997**, *66* (5), 489-505.
152. Wu, M. Y.; Xiao, X. C.; Vukmirovic, N.; Xun, S. D.; Das, P. K.; Song, X. Y.; Olalde-Velasco, P.; Wang, D. D.; Weber, A. Z.; Wang, L. W.; Battaglia, V. S.; Yang, W. L.; Liu, G., Toward an Ideal Polymer Binder Design for High-Capacity Battery Anodes. *Journal of the American Chemical Society* **2013**, *135* (32), 12048-12056.
153. Zeng, W. W.; Wang, L.; Peng, X.; Liu, T. F.; Jiang, Y. Y.; Qin, F.; Hu, L.; Chu, P. K.; Huo, K. F.; Zhou, Y. H., Enhanced Ion Conductivity in Conducting Polymer Binder for High-Performance Silicon Anodes in Advanced Lithium-Ion Batteries. *Advanced Energy Materials* **2018**, *8* (11).
154. Choi, S.; Kwon, T. W.; Coskun, A.; Choi, J. W., Highly elastic binders integrating polyrotaxanes for silicon microparticle anodes in lithium ion batteries. *Science* **2017**, *357* (6348), 279-283.
155. Lv, Y. Y.; Shang, M. W.; Chen, X.; Nezhad, P. S.; Niu, J. J., Largely Improved Battery Performance Using a Microsized Silicon Skeleton Caged by Polypyrrole as Anode. *Acs Nano* **2019**, *13* (10), 12032-12041.
156. Kostic, R.; Rakovic, D.; Stepanyan, S. A.; Davidova, I. E.; Gribov, L. A., VIBRATIONAL SPECTROSCOPY OF POLYPYRROLE, THEORETICAL-STUDY. *Journal of Chemical Physics* **1995**, *102* (8), 3104-3109.

157. Yamaguchi, M., Effect of molecular structure in branched polyethylene on adhesion properties with polypropylene. *Journal of Applied Polymer Science* **1998**, 70 (3), 457-463.
158. Chen, Q.; Sieradzki, K., Spontaneous evolution of bicontinuous nanostructures in dealloyed Li-based systems. *Nature Materials* **2013**, 12 (12), 1102-1106.
159. Lin, D. C.; Lu, Z. D.; Hsu, P. C.; Lee, H. R.; Liu, N.; Zhao, J.; Wang, H. T.; Liu, C.; Cui, Y., A high tap density secondary silicon particle anode fabricated by scalable mechanical pressing for lithium-ion batteries. *Energy & Environmental Science* **2015**, 8 (8), 2371-2376.
160. Fang, Y.; Lv, Y. Y.; Gong, F.; Elzatahry, A. A.; Zheng, G. F.; Zhao, D. Y., Synthesis of 2D-Mesoporous-Carbon/MoS<sub>2</sub> Heterostructures with Well-Defined Interfaces for High-Performance Lithium-Ion Batteries. *Advanced Materials* **2016**, 28 (42), 9385-+.
161. Sevilla, M.; Yu, L. H.; Fellingner, T. P.; Fuertes, A. B.; Titirici, M. M., Polypyrrole-derived mesoporous nitrogen-doped carbons with intrinsic catalytic activity in the oxygen reduction reaction. *Rsc Advances* **2013**, 3 (25), 9904-9910.
162. Naguib, M.; Kurtoglu, M.; Presser, V.; Lu, J.; Niu, J. J.; Heon, M.; Hultman, L.; Gogotsi, Y.; Barsoum, M. W., Two-Dimensional Nanocrystals Produced by Exfoliation of Ti<sub>3</sub>AlC<sub>2</sub>. *Advanced Materials* **2011**, 23 (37), 4248-4253.
163. Zhang, Y. L.; Mu, Z. J.; Lai, J. P.; Chao, Y. G.; Yang, Y.; Zhou, P.; Li, Y. J.; Yang, W. X.; Xia, Z. H.; Guo, S. J., MXene/Si@SiO<sub>x</sub>@C Layer-by-Layer Superstructure with Autoadjustable Function for Superior Stable Lithium Storage. *Acs Nano* **2019**, 13 (2), 2167-2175.
164. Wang, C. D.; Chen, S. M.; Xie, H.; Wei, S. Q.; Wu, C. Q.; Song, L., Atomic Sn<sup>4+</sup> Decorated into Vanadium Carbide MXene Interlayers for Superior Lithium Storage. *Advanced Energy Materials* **2019**, 9 (4).

165. Liang, X.; Garsuch, A.; Nazar, L. F., Sulfur Cathodes Based on Conductive MXene Nanosheets for High-Performance Lithium-Sulfur Batteries. *Angewandte Chemie-International Edition* **2015**, *54* (13), 3907-3911.
166. Shang, M. W.; Chen, X.; Li, B. X.; Niu, J. J., A Fast Charge/Discharge and Wide-Temperature Battery with a Germanium Oxide Layer on a Ti<sub>3</sub>C<sub>2</sub> MXene Matrix as Anode. *Acs Nano* **2020**, *14* (3), 3678-3686.
167. Stokes, K.; Boonen, W.; Geaney, H.; Kennedy, T.; Borsa, D.; Ryan, K. M., Tunable Core-Shell Nanowire Active Material for High Capacity Li-Ion Battery Anodes Comprised of PECVD Deposited aSi on Directly Grown Ge Nanowires. *Acs Applied Materials & Interfaces* **2019**, *11* (21), 19372-19380.
168. Mishra, K.; Liu, X. C.; Geppert, M.; Wu, J. J.; Li, J. T.; Huang, L.; Sun, S. G.; Zhou, X. D.; Ke, F. S., Submicro-sized Si-Ge solid solutions with high capacity and long cyclability for lithium-ion batteries. *Journal of Materials Research* **2018**, *33* (11), 1553-1564.
169. Forney, M. W.; Ganter, M. J.; Staub, J. W.; Ridgley, R. D.; Landi, B. J., Prelithiation of Silicon-Carbon Nanotube Anodes for Lithium Ion Batteries by Stabilized Lithium Metal Powder (SLMP). *Nano Letters* **2013**, *13* (9), 4158-4163.

# CURRICULUM VITAE

**Mingwei Shang**

## **EDUCATION**

- **Materials Engineering, PhD**, 09.2016-Now, (graduation date: 05/23/2021)  
Department of Materials Science & Engineering, University of Wisconsin  
Milwaukee, WI, US

*Research Topics:* (1) Lithium-ion batteries: high-performance Ni-rich, Li-Mn-rich cathode materials; regeneration of high-performance cathode material from spent LIBs; Ge, Si advanced anode materials; (2) hydrophobic/hydrophilic surface modification; (3) Water treatment: heavy metal ions removal; (4) Lead-acid batteries.

12 publications (6 first author), 2 patents, 3 times of Chancellor Graduate Student Award, 1 UWM Graduate Student Excellence Fellowship

- **Master of Science in Materials**, 01.2013-05.2014  
Department of Physics, Astronomy & Materials Science, Missouri State University,  
Springfield, MO, US

*Research Topics:* All solid-state dye-sensitized solar cells.

- **Master of Engineering in Materials**, 09.2011-07.2014  
College of Materials Science & Engineering, Qingdao University of Science &  
Technology, Qingdao, China

*GPA:* 3.26/4.0 (Total) 3.62/4.0 (Relevant)

*Research Topics:* All solid-state dye-sensitized solar cells.

- **Bachelor of Science in Materials Physics**, 09.2007-07.2011  
College of Materials Science & Engineering, Qingdao University of Science &  
Technology, Qingdao, China

## **WORKING EXPERIENCE**

- **University of Wisconsin-Milwaukee**
  - Graduate Research Assistant/Teaching Assistant for undergraduate level Engineering Materials Lab. 09.2016-Now
  - In charge of lab management, including supplies ordering, lab safety and inspection.
- **Missouri State University**

- Graduate Research Assistant in the Field Emission Scanning Electron Microscopy Laboratory, 01.2013-07.2013
  - Graduate Teaching Assistant for undergraduate level Physics Lab sections, 08.2013-05.2014
  - Project Advisor Assistant in high school student research team, which received the Grand Prize and the 1st place in the category of Senior Chemistry at the 54th Annual Ozarks Science & Engineering Fair and was selected to compete at the 2014 Intel International Science & Engineering Fair.
- **Qingdao University of Science & Technology**
- Vice-president of Graduate Student Union in the College of Materials Science & Engineering, 09.2011-01.2013
  - Research Assistant at the Institute of Advanced Energy Materials and Devices, 08.2014-07.2015

## SKILLS

- ✓ Morphology characterizations: High-resolution transmission electron microscopy, Field Emission Scanning Electron Microscope
- ✓ Structural and chemical characterizations: X-ray Diffraction, X-ray photoelectron spectroscopy, Raman, Photoluminescence, UV-vis spectrum, Semiconductor probe workstation, External quantum efficiency, Porosity and specific surface area measurement (BET)
- ✓ Inductively coupled plasma mass spectrometry
- ✓ Electrochemical characterization: Electrochemical Workstation, Landt Battery Test System.

## PUBLICATIONS

- 1) **M. Shang**, X. Chen, J. Niu, Ni-rich layered transition metal oxide cathode with dual gradient on both primary and secondary particles for high energy-density lithium-ion batteries, Under preparation.
- 2) **M. Shang**, M. Samuel, J. Niu, Strengthened self-cleaning coating on glaze via a two-layer configuration, under preparation.
- 3) **M. Shang**, X. Chen, B. Li, J. Niu. A fast charge/discharge and wide-temperature battery with germanium oxide layer on TiCA3 MXene matrix as anode. *ACS Nano*, 14 (2020), 3678-3686.
- 4) Y. Lv, **M. Shang (co-first author)**, X. Chen, P. Nezhad, J. Niu, Largely improved battery performance using micro-sized silicon skeleton caged by polypyrrole as anode. *ACS Nano*, 13 (2019), 12032-12041.
- 5) Y. Lv, **M. Shang (co-first author)**, X. Chen, J. Niu. Double-net enclosed sulfur composite as a new cathode in lithium sulfur batteries. *The Journal of Physical Chemistry C*, 123 (2019), 17719-17727.

- 6) X. Chen, **M. Shang**, J. Niu, A pre-SEI covered Li metal anode with improved electrochemo-mechanical reliability in high energy-density batteries, under review.
- 7) M. Samuel, **M. Shang**, S. Klimchuk, J. Niu. Novel regenerative hybrid composite adsorbent with improved removal capacity for lead ions in water. *Industrial & Engineering Chemistry Research*, (2021), in print, <https://doi.org/10.1021/acs.iecr.0c06277>.
- 8) X. Li, Y. Zheng, Y. Duan, **M. Shang**, J. Niu, C. Li. Designing Comb-Chain Crosslinker-Based Solid Polymer Electrolytes for Additive-Free All-Solid-State Lithium Metal Batteries. *Nano Letters*, 20 (2020), 6914-6921.
- 9) X. Chen, **M. Shang**, Junjie Niu. Inter-layer-calated thin Li metal electrode with improved battery capacity retention and dendrite suppression. *Nano Letters*, 20 (2020), 2639-2646.
- 10) S. Klimchuk, **M. Shang**, M. Samuel, J. Niu. A robust hybrid hydrophilic coating on HDPE surface with enhanced mechanical property. *ACS Applied Materials & Interfaces*, 12 (2020), 32017-32022.
- 11) X. Chen, Y. Lv, **M. Shang**, J. Niu. Iron controllable lithium into lithiotropic carbon fiber fabric: a novel Li metal anode with improved cyclability and dendrite suppression. *ACS Applied Materials & Interfaces*, 11 (2019), 21584-21592.
- 12) Y. Ye, S. Klimchuk, **M. Shang**, K. McDonald, Junjie Niu. Acoustic bubble suppression by constructing a hydrophilic coating on HDPE surface. *ACS Applied Materials & Interfaces*, 11(2019), 16944-16950.
- 13) Y. Ye, S. Klimchuk, **M. Shang**, J. Niu. Improved antibacterial performance using hydrogel-immobilized lysozyme as catalyst in water. *RSC Advances*, 9 (2019), 20169-20173.
- 14) S. Kang, **M. Shang**, M. Spence, M. Andrew, S. Liu, and J. Niu. Dynamic charge acceptance and hydrogen evolution of new MXene additive in advanced lead-acid batteries via a rapid screening three-electrode method. *ChemComm*. 54 (2018), 3456-3459.
- 15) Y. Kim, **M. Shang**, S. Kang, J. Karsseboom, and J. Niu. A strong hydrophobic coating by conducting a new hierarchical architecture. *The Journal of Physical Chemistry C*, 122 (2018) 4628-4634.
- 16) **M. Shang**, B. Liu, Z. Dong, Z. Dong and L. Dong, Effects of counter electrodes on photovoltaic performance of all-solid-state TiO<sub>2</sub>-based dye-sensitized solar cells. *Materials Research Express* 2.3 (2015): 035502.
- 17) **M. Shang**, B. Liu, Z. Dong, Z. Dong, Q. Sun, L. Dong, Effects of Electrolytes on the Photoelectric Properties of TiO<sub>2</sub>-Based Dye-Sensitized Solar Cells. *ECS Transactions* 61.1 (2014): 169-174.
- 18) **M. Shang**, C. Liu, Q. Sun, Q. Zhang, H. Dong, L. Dong, Fabrication and Photovoltaic Properties of Cu<sub>2</sub>O/ZnO p-n Heterojunction Solar Cells, *Chinese Journal of Luminescence* 34, (2012): 197-201
- 19) S. Ma, **M. Shang**, L. Y. Yu, and L. F. Dong, Ma, Shuai, et al. Device optimization of CsSnI<sub>2.95</sub>F<sub>0.05</sub>-based all-solid-state dye-sensitized solar cells with non-linear charge-carrier-density dependent photovoltaic behaviors. *Journal of Materials Chemistry A* 3.3 (2015): 1222-1229.
- 20) Y. Zhang, **M. Shang**, T. Xia, P. Wallenmeyer, J. Murowchick, L. Dong, and X. Chen, Influence of the Amount of HF on the Formation of (001) Faceted TiO<sub>2</sub> Nanosheets and their Photocatalytic Hydrogen Generation Performance, *ChemPlusChem* 1 (2015): 270-275.

- 21) Y. Zhang, T. Xia, **M. Shang**, P. Wallenmeyer, D. Katelyn, A. Peterson, J. Murowchick, L. Dong, and X. Chen, Zhang, Yuliang, et al. Structural evolution from TiO<sub>2</sub> nanoparticles to nanosheets and their photocatalytic performance in hydrogen generation and environmental pollution removal. *RSC Advances* 4.31 (2014): 16146-16152.
- 22) K. Wu, C. Liu, **M. Shang**, Q. Zhu, L. Dong. Photoelectrochemical Properties of  $\alpha$ -Fe<sub>2</sub>O<sub>3</sub>: Sn/CuFe<sub>2</sub>O<sub>4</sub> Composite Nanorod Arrays as Photoanodes. *ECS Transactions* 53.22 (2013): 49-56.